Simulation and Modeling of Mono- and Bidisperse Suspensions

Kai Höfler

Von der Fakultät Physik der Universität Stuttgart
zur Erlangung der Würde eines Doktors der
Naturwissenschaften (Dr. rer. nat.) genehmigte Abhandlung

Vorgelegt von Kai Höfler aus Aichhalden

Hauptberichter: Prof. Dr. H. J. Herrmann
Mitberichter: Prof. Dr. G. Wunner
Tag der mündlichen Prüfung: 26. Juli 2000

Universität Stuttgart
Institut für Computeranwendungen 1

2000

Contents

Preface

Many applications in chemical engineering [27, 97], fluid mechanics [33], geology [85], and biology involve systems of particles immersed in a liquid or gas flow. Examples of such systems are sedimentation processes, gas-solid or liquid-solid fluidized beds, blood, mixing processes when sediment-laden rivers enter lakes or the sea, powder transport by pneumatic conveying, the ticking of hour glasses, flocculation in suspensions, and many more.

Although all suspensions are based on the same fundamentals – solid particles are *suspended* in a fluid or a gas – the physical properties that dominate the behavior could not be more diverse.

- In colloidal chemistry the behavior of a suspension is dominated by physical and chemical properties of the particles and the fluid, so that interparticle forces such as repulsive electrostatic or attractive van der Waals forces determine the state of a suspension. The addition of a small amount of additive containing, e.g. free ions, to the fluid may cause a stable suspension to flocculate.
- If particles like sand or dust are transported by the air flow in low concetrations, they do not cause a distinct change of the flow. Therefore, clouds of dust, e.g. from volcanic eruptions, are transported over large distances in the atmosphere.
- In contrast to low particles concentrations, the behavior changes dramatically if we consider high particle concentrations, as they occur in dust avalanches, where e.g. powdery snow slides down a mountain. The particles themselves drive the airflow and are able to cause wind velocities in excess of 200 km/h [32].

This selection of examples is far from being complete but it already shows that the physics of suspensions is very rich in phenomena and the *classical* problem of sedimentation is only a starting point for the exploration of the vast field of particles suspensions.

Particle suspensions have all in common that the long-ranged hydrodynamic interactions mediated by the fluid in the interstitial voids of a particulate, granular system greatly

change its physical behavior as compared to the “dry” state without medium. The dry state is characterized by the short-ranged, mostly viscoelastic forces that act when single grains come into contact. Thus the behavior of a dry granular system depends very strongly on the particle volume fraction. Dust avalanches are an ideal example of this phenomenon. As long as the dust rests on the ground the air in the in the interstitial voids is of no interest and the dust may be described like a heap of sand. But as soon as the particles start to move, the particle volume fraction is reduced and the particles lose contact. Now the air between the particles mediates a coupling of the movements of single particles.

The analytical description of suspensions is limited to special cases, such as zero Reynolds numbers, spherical particles, infinite system sizes, or periodic boundary conditions. We therefore have to rely on phenomenological descriptions of the suspension or on computer simulations. Phenomenological descriptions have proven to provide accurate predictions for special cases [15, 57] but they are limited to parameter ranges where the physical mechanisms dominating the suspension behavior do not change. Computer simulations in principle overcome this restriction but suffer from the enormous expense that is associated with the numerical representation of freely moving boundaries in a fluid. It is therefore necessary to find a description of suspensions which allows to transfer the particle scale phenomena to a macroscopic scale. However, such a project is not possible without a detailed understanding of the suspension.

To gain such an understanding, we study the sedimentation of mono- and bidisperse suspensions. We restrict our studies to non-Brownian, hard spheres with a discrete distribution of sizes and densities settling under the influence of gravity in a quadrilateral container. The container may either have walls on the boundaries or be periodically continued.

The thesis is organized as follows: In Chapter 1 we describe the fluid dynamical foundation of the problem and describe some basic properties of particles suspended in a fluid. We then describe in Chapter 2 a numerical simulation technique that is capable of simulating more than 10^9 degrees of freedom and use this simulation technique to study monodisperse (Chapter 3) and bidisperse (Chapter 4) suspensions. Based on the simulations and experimental data, we show that a advection-diffusion model for the particle concentration is able to describe the settling of polydisperse suspensions (Chapter 5).

Chapter 1

The Physics of Particle Suspensions

1.1 The Fluid

1.1.1 Continuum Mechanical Description

The theoretical description of liquids is based on the continuum hypothesis, which states that it is possible to associate the macroscopic properties of the fluid with any volume of fluid, no matter how small it is, and that the fluid consists of a continuous aggregate of such fluid elements [101]. We know that the continuum hypothesis breaks down for very small length scales of the order of the length of the mean free path of the molecules which form the fluid. However if the scale of the phenomena of interest is seperated clearly from that of the mean free path, then we can choose an averaging length scale on which each volume element contains so many particles that the fluctuations of the mean value of a physical quantity is negligible.

Building on the continuum hypothesis we can describe the movement of a fluid by its local velocity $\vec{v}(\vec{x},t)$, local density $\rho(\vec{x},t)$, and local pressure $p(\vec{x},t)$ where $\vec{x}$ is the position in space fixed coordinates and t is the time. We will only deal with isothermal processes and therefore not include the temperature in our considerations. To formulate the basic equations for the fluid we utilize the conservation of mass and momentum.

We consider a volume V of fluid in Eulerian (space fixed) coordinates. The mass of the volume changes due to the in- and outflow of fluid through the surface S. So that the change of mass is

$$\frac{\partial}{\partial t}\int_V \rho \,\mathrm{d}V = -\int_S \rho\vec{v}\cdot\mathrm{d}\vec{S} \tag{1.1}$$

where $\mathrm{d}\vec{S}$ is a volume element of the surface with an outward normal. Because the integration volume does not change with time we can exchange the integral with the time derivative and by applying Gauss's theorem we find the continuity equation,

$$\frac{\partial \rho}{\partial t} + \nabla \cdot (\rho \vec{v}) = 0. \tag{1.2}$$

Additional equations are found by using the conservation of momentum, or Newton's second law, i.e. the change of momentum of a fluid element is equal to the force acting on it. We follow the movement of a fluid element such that it always contains the same molecules. This implies that the volume of this fluid element may change, but that its mass is constant. As a consequence, the momentum of the fluid element changes only due to changes in the velocity

$$\rho \frac{\mathrm{d}\vec{v}}{\mathrm{d}t} = \rho \frac{\partial \vec{v}}{\partial t} + \rho \left(\frac{\mathrm{d}x}{\mathrm{d}t} \frac{\partial \vec{v}}{\partial x} + \frac{\mathrm{d}y}{\mathrm{d}t} \frac{\partial \vec{v}}{\partial y} + \frac{\mathrm{d}z}{\mathrm{d}t} \frac{\partial \vec{v}}{\partial z} \right), \tag{1.3}$$

or equivalently

$$\rho \frac{\mathrm{d}\vec{v}}{\mathrm{d}t} = \rho \frac{\partial \vec{v}}{\partial t} + \rho (\vec{v} \cdot \nabla) \vec{v}. \tag{1.4}$$

Here the velocity enters Eq. (1.4) in two ways: First as the quantity that changes as the fluid moves and second as the quantity that controls how fast the change occurs.

Now that we know how the momentum changes we must consider the forces acting on a fluid element. In principle there are two type of forces, namely surface and volume forces, so that we can write

$$\frac{\mathrm{d}}{\mathrm{d}t} \int_V \rho \vec{v} \, \mathrm{d}V = \int_S \mathbf{T}(\vec{x}, t) \, \mathrm{d}\vec{S} + \int_V \vec{f}(\vec{x}, t) \, \mathrm{d}V \tag{1.5}$$

where $\mathbf{T}$ is the symmetric stress tensor which describes the surface forces in case of no internal torques in the fluid and $\vec{f}$ is an arbitrary force acting on the fluid volume like, e.g., gravity. As Eq. (1.5) is valid independent of the actual form of the integration volume, the relation must therefore hold also for the integrands only. By applying Gauss's theorem to the surface integral on the right hand side we obtain

$$\rho \frac{\partial \vec{v}}{\partial t} + \rho (\vec{v} \cdot \nabla) \vec{v} = \nabla \mathbf{T}(\vec{x}, t) + \vec{f}(\vec{x}, t). \tag{1.6}$$

Eq. (1.6) together with Eq. (1.2) provide 4 equations for the 5 variables velocity, pressure and density. The last equation is given by the equation of state for the fluid $\rho = \rho(p)$. In many cases, especially when the fluid velocities are much smaller than the speed of sound in the fluid, the fluid can be regarded as incompressible and ρ is a constant.

We now have to specify the nature of the stress tensor $\mathbf{T}$. Often the symmetric stress tensor $\mathbf{T}$ is divided into two contributions, (i) the diagonal part of T_{ij} and (ii) the off

diagonal part $\tilde{T}_{ij} = T_{ij} - 1/d\delta_{ij}T_{kk}$. The trace of the first is the pressure acting in normal direction on a fluid element, and the second the shear force acting perpendicular to the surface normal. In an ideal fluid with no friction $\tilde{T}_{ij}$ is zero and Eq. (1.6) reduces to the Euler equation

$$\rho\frac{\partial\vec{v}}{\partial t} + \rho(\vec{v}\cdot\nabla)\vec{v} = -\nabla p + \vec{f}. \tag{1.7}$$

For a viscous fluid $\tilde{T}$ is not zero and friction occurs when the distance between two neighboring fluid elements changes,i.e. they move relative to each other. The force is proportional to the relative velocity of the two fluid elements. The most general form of the stress tensor for isotropic fluids linear in the velocity gradients is [101]

$$T_{ij} = -p\delta_{ij} + \eta\left(\frac{\partial v_i}{\partial x_j} + \frac{\partial v_j}{\partial x_i} - \frac{2}{3}\delta_{ij}\frac{\partial v_k}{\partial x_k}\right) + \xi\delta_{ij}\frac{\partial v_k}{\partial x_k}, \tag{1.8}$$

where η is called shear viscosity and ξ the bulk viscosity, which is the resistance of the fluid against compression. For the case of an incompressible fluid $\rho = \mathrm{const}$ the continuity equation (1.2) reduces to $\nabla\cdot\vec{v} = 0$, so that the compressible part of the stress tensor disappears. By inserting Eq. (1.8) in Eq. (1.6) we arrive at the Navier-Stokes equation for a incompressible fluid

$$\rho\frac{\partial\vec{v}}{\partial t} + \rho(\vec{v}\cdot\nabla)\vec{v} = -\nabla p + \eta\nabla^2\vec{v} + \vec{f}. \tag{1.9}$$

The Navier-Stokes equation is a set of three nonlinear partial differential equations for $\vec{v}$ and p, whose nonlinearity is due to the convective term of the time derivative. Together with appropriate boundary conditions and the incompressibility constraint, these four unknowns can be determined in space and time.

1.1.2 Boundary Conditions

Since the Navier-Stokes equations of the fluid motion are partial differential equations, we need boundary and initial conditions to solve these equations. The typical boundaries for a fluid are (i) solid, impermeable walls, (ii) the boundary to another fluid and (iii) a free surface of the fluid. We will only consider the case where the boundary consists of solid walls, because we will only deal with solid suspended particles in this thesis.

One condition in case of a solid, impermeable wall is that no fluid may pass through the wall. Thus the velocity component normal to the boundary must equal the velocity of the wall.

$$\vec{v}\cdot\vec{n} = \vec{V}_S\cdot\vec{n}, \tag{1.10}$$

where $\vec{V}_S$ is the velocity of the wall.

The second condition for the tangential component of the velocity is not as obvious. It has been shown by experiments that the *no-slip* boundary condition applies for the boundary of normal fluids and solid walls, because the surface of the wall acts like a layer of fluid moving with velocity $\vec{V}_S$. The viscosity of the fluid prevents a discontinuity of the velocity between the fluid and the wall. The no-slip boundary condition is expressed by

$$\vec{v} \times \vec{n} = \vec{V}_S \times \vec{n}, \tag{1.11}$$

and is independent of the condition for the normal component.

We will later utilize the equivalence of a solid wall boundary with a fluid moving with the same velocity in our numerical method to describe the suspended particles.

1.1.3 Dimensionless Description

The concept of *dynamical similarity* says that under some conditions the flow patterns of two similar geometries are also similar. This concept allows for the usage of small-scale models and wind-tunnels or towing-tanks to design and test the fluid dynamical properties of aeroplanes, cars, and ships. The question is now under which condition two similar geometries will produce similar flow patterns.

Let us introduce typical length and velocity scales L and U of our system. These are typical scales of the system, e.g. the size of an obstacle in the flow and a typical velocity of the fluid. We use this characteristic values to obtain a non-dimensional form of the variables, which we denote by primes,

$$\vec{x}' = \vec{x}/L, \quad \vec{v}' = \vec{v}/U, \quad t' = tU/L. \tag{1.12}$$

Substituting Eq. (1.12) into (1.9) and multiplying the resulting equation by $L/\rho U^2$ gives the dimensionless Navier-Stokes equation

$$\frac{\partial \vec{v}'}{\partial t'} + (\vec{v}' \cdot \nabla')\vec{v}' = -\frac{1}{\rho U^2}\nabla' p + \frac{\eta}{UL\rho}\nabla'^2\vec{v}' + \frac{L}{\rho U^2}\vec{f}. \tag{1.13}$$

where the spatial and time derivative transform like

$$\nabla' = L\nabla, \quad \text{and} \quad \frac{\partial}{\partial t'} = \frac{L}{U}\frac{\partial}{\partial t}. \tag{1.14}$$

If we measure the pressure and the force in units of $1/\rho U^2$ and $L/\rho U^2$ then the equations for the non-dimensional variables are the same if $\eta/UL\rho$ is the same in the two geometrically similar situations As all variables are now primed we drop the primes and write the final, dimensionless form of the Navier-Stokes equation

$$\frac{\partial \vec{v}}{\partial t} + (\vec{v} \cdot \nabla)\vec{v} = -\nabla p + \frac{1}{Re}\nabla^2\vec{v} + \vec{f}, \tag{1.15}$$

where Re is the so called Reynolds number

$$Re = \frac{UL\rho}{\eta} = \frac{UL}{\nu} \tag{1.16}$$

and $\nu = \eta/\rho$ is the kinematic viscosity.

If we neglect the external forces $\vec{f}$ then two geometrically identical situations will have the same solutions and therefore the same flow patterns if the Reynolds number is the same in both situations because then the Navier-Stokes equations are identical. Thus the Reynolds number is the condition for dynamical similarity.

1.1.4 The Stokes Equations

We find a physical interpretation of the Reynolds number Re, introduced in the previous section, by comparing the ratio of the inertial term of the Navier-Stokes equation

$$|\vec{v} \cdot \nabla \vec{v}| \sim \frac{U^2}{L} \tag{1.17}$$

to the viscous term

$$|\nu \nabla^2 \vec{v}| \sim \frac{\nu U}{L^2}. \tag{1.18}$$

We find that the Reynolds number indicates the ratio of inertia forces to viscous forces

$$\frac{|\vec{v} \cdot \nabla \vec{v}|}{|\nu \nabla^2 \vec{v}|} \sim \frac{UL}{\nu} = Re. \tag{1.19}$$

Thus, when the Reynolds number is very small ($Re \ll 1$) the inertia term of the Navier-Stokes equation (1.15) is very small compared to the viscous forces and we may neglect it. This leads to the so called Stokes equation for a viscous fluid,

$$\frac{\partial \vec{v}}{\partial t} = -\nabla p + \frac{1}{Re} \nabla^2 \vec{v} + \vec{f}. \tag{1.20}$$

The Stokes equation is a linear equation in $\vec{v}$ and therefore analytically easier to handle than the full Navier-Stokes equation. It also shows two features present in low Reynolds number flow, namely flow reversibility and the long-range nature of the viscous interactions. Due to the linearity new solutions to the Stokes equation can be found by superposition of known solutions.

1.2 Particles in Fluid

In this section we look at the flow of viscous fluid in the presence of a single or many spherical particles. The analytical calculations are only possible in the limit of low-Reynolds number flows where the Stokes equation is still valid.

1.2.1 A Single Particle

A famous solution of the Stokes equation (1.20) is the flow past a sphere. The solution of the flow field is used to calculate the force on the sphere.

The problem is best considered in spherical coordinates. We choose a frame of reference where the sphere is at rest and the orientation so that $\Theta = 0$ in the flow direction. By symmetry the azimuthal component of the velocity is equal to zero $v_\phi = 0$. The fluid is moving with constant velocity $\vec{v}_0$ at infinity, which gives the boundary conditions

$$v_r = v_0 \cos\Theta, \quad \text{and} \quad v_\Theta = -v_0 \sin\Theta \tag{1.21}$$

at $r = \infty$. The boundary conditions on the sphere can be expressed by

$$v_r = v_\Theta = 0 \quad \text{at} \quad r = a \tag{1.22}$$

where a is the radius of the sphere. The solution of Eq. (1.20) is then [39]

$$v_r = v_0 \cos\Theta \left(1 - \frac{3a}{2r} + \frac{a^3}{2r^3}\right), \tag{1.23}$$

$$v_\Theta = -v_0 \sin\Theta \left(1 - \frac{3a}{4r} + \frac{a^3}{4r^3}\right), \tag{1.24}$$

$$p - p_0 = -\frac{3}{2}\frac{\eta v_0 a}{r^2}\cos\Theta. \tag{1.25}$$

The main characteristic of the solution is that the disturbance from the velocity field without a sphere decays $\sim 1/r$. This shows that the flow field is influenced by the presence of a sphere over large distances. To calculate the force on the particle we need the stress on the surface of the particle. On a boundary at rest the pressure and viscous forces per unit area are given by

$$T_{\Theta\Theta} = -\eta \left(\frac{\partial v_\Theta}{\partial r}\right)_{r=a} \sin\Theta - (p - p_0)_{r=a}\cos\Theta, \tag{1.26}$$

which equals the constant value

$$T = \frac{3\eta v_0}{2a} \tag{1.27}$$

By (trivial) integration over the surface we get

$$F_D = 6\pi\eta a v_0, \tag{1.28}$$

the drag on a sphere in an unbounded fluid. It should be noted that due to the fact that the viscous effect extends over a long range, even distant boundaries have a large effect on the particles. E.g. in a falling-sphere viscometer the radius of the container has to be 100 times larger than that of the sphere to reduce the error to less than 2% [39].

It is now easy to calculate the velocity of a particle settling under gravity in a unbounded fluid. The resulting velocity U_{St} is called the Stokes velocity,

$$U_{\mathrm{St}} = \frac{2}{9}\frac{a^2(\rho_{\mathrm{p}} - \rho)g}{\eta}, \tag{1.29}$$

where ρ_{p} is the density and a the radius of the particle.

1.2.2 A Fixed Array Of Particles

One of the first approaches to calculate the velocity of suspended particles was to compute the resistance of a fixed assemblage of particles. In the presence of walls the method of reflections [39] is used to find the correct flow field and the forces on the particles iteratively. The solution is approximated by considering the boundary conditions with one particle at a time, which is called a reflection. A different technique was used by Hasimoto [41] to calculate the force on a periodic array of particles. He used the periodicity of the problem to expand the fluid fields into Fourier series. By using a point particle approximation he found that the force on a particle is given by

$$F = \frac{6\pi a\eta u}{1 - 1.7601\phi^{\frac{1}{3}} + \phi - 1.5593\phi^2} \tag{1.30}$$

where ϕ is the fraction of the volume occupied by the particles. The settling velocity U of such an array is therefore given by

$$U = \frac{U_{\mathrm{St}}}{1 - 1.7601\phi^{\frac{1}{3}} + \phi - 1.5593\phi^2}. \tag{1.31}$$

For $\phi \ll 1$ the change in the velocity is proportional to $\phi^{-\frac{1}{3}}$ and therefore proportional to the inverse of the particle separation.

1.2.3 Freely Moving Particles

In a real suspension the particle positions are not fixed, so that the particles are able to change their relative positions. This renders the calculation of the settling velocities difficult, because we must know the particle distribution to determine the average particle velocity $\langle U \rangle$, which is defined by

$$\langle U \rangle = \frac{1}{N}\sum_{i=1}^{N} U_i. \tag{1.32}$$

For monodisperse suspensions the particle distribution is not known a priori. We must distinguish between two cases

1. The particles are so small that the continuum hypothesis is only partially fulfilled. Then the particles show an erratic random motion, the so called Brownian motion.

2. The particles are large enough so that the Brownian motion is neglegible.

The so called Péclet number Pe provides an estimate whether the Brownian motion of particles may be neglected. The Péclet number compares the ratio of heat advection to heat conduction and is defined by

$$Pe = \frac{Ua}{D}, \tag{1.33}$$

where U is a typical velocity of the particle, a its radius and D is the thermal diffusion coefficient. For $Pe \gg 1$ the advective motion of the particle dominates and the Brownian motion can be neglected, whereas for $Pe \ll 1$ the Brownian motion is dominating and the particle movement will be largely of random nature. In case of low Péclet number we therefore expect to find a locally homogeneous particle distribution. This shows that even if we do not consider interparticle forces, the particle distribution is not known a priori.

There have been many approaches to calculate the average settling velocity of the particles in a suspension. We will briefly describe Batchelor's idea [7] which is based on two-particle interactions.

Batchelor considers a random suspension at low volume fraction ϕ. He assumes that the particle distribution is homogeneous and calculates the pair interaction between a test sphere positioned at $\vec{x}_0$ and all possible positions of particles. The mean settling velocity is then given by

$$\langle U \rangle = \frac{1}{N!} \int U(\vec{x}_0, \mathcal{C}_N) P(\mathcal{C}_N | \vec{x}_0) \mathrm{d}\mathcal{C}_N, \tag{1.34}$$

where $\mathcal{C}$ is a configuration of N spheres, and $P(\mathcal{C}_N|\vec{x}_0)$ is the conditional probability density of a configuration of $N+1$ particles given that there is a sphere at the position $\vec{x}_0$.

The main problem is that the integral (1.34) is divergent because the velocity field of a particle decays $\sim r^{-1}$. He overcomes this problem by calculating $U - V$ where V is the translational velocity due to the nonuniform environment. In this fashion, he finds $\langle U \rangle$ up to order ϕ,

$$\langle U \rangle = U_{\mathrm{St}}(1 - 6.55\phi). \tag{1.35}$$

Although Eq. (1.35) is only valid at low volume fractions, Batchelor's linear approximation of the hindered settling function captures one of the main features of particle suspensions. If the particle volume fraction is increased, the settling of the particles is hindered due to the backflow of liquid caused by the other particles.

For particle volume fractions larger than ≈ 0.15 the Eq. (1.35) predicts negative settling velocities, i.e. the particles will rise. This shows that the linear theory must not be applied over the whole range of possible volume fractions. A second order approximation of the hindered settling function would require to take three particle interactions into account. This approach has been taken e.g. by P. Mazur et. al. and Brady et.al. [70, 13] and leads to better approximations of the hindered settling function. But in all cases one has to make assumptions on the particle distribution within the suspension.

The calculations of the hindered settling function assume that the particles are distributed homogeneously within the volume. If this is not the case, say due to the initial conditions or generated by inclined walls as shown in Figure 1.1, the calculations are not valid any more. In case of inhomogeneous initial conditions as shown on the left side of Figure 1.1, the backflow generated by the particles is not forced to move through the particles but avoids the region of high particle concentration. Thus the hindered settling effect is reduced. In the case of inclined walls, an initially homogeneous distribution of particles will develop areas of higher concentrations (dark grey in Figure 1.1) and areas of lower particle concentration (light grey), where the upward moving fluid flows without the hindrance of settling particles.

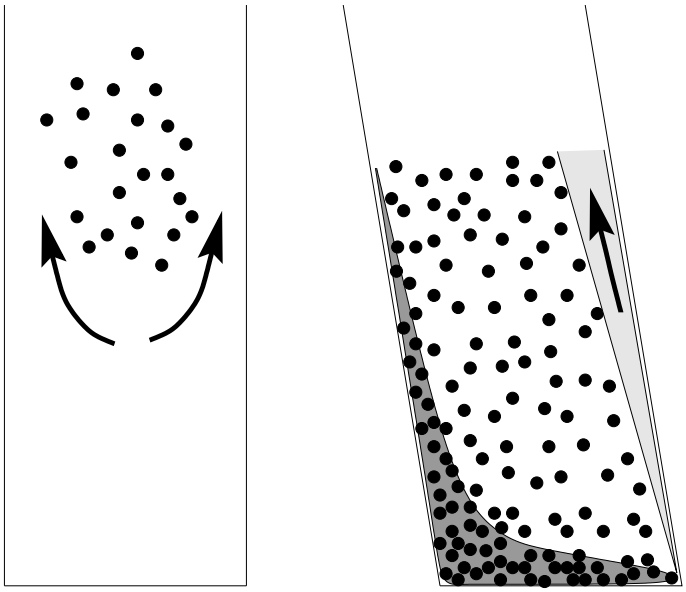

Figure 1.1: Sketch of two situations where the average particle settling velocity is increased due to a inhomogeneous initial particle distribution (left side) or inclined walls (right side). In both cases the backflow generated by the settling particles avoids the particles and the average particle velocity is increased.

A similar situation occurs when there are long-range interparticle forces or other physical effects that lead to clustering of the particles. In such cases the hindered settling function

does not need to be a monotonically decreasing function of the volume fraction.

Chapter 2

Simulation Method

Because of its great importance, the problem of particle suspensions has been and is still attracting considerable attention on both the experimental and theoretical level. As is known from the physics of liquids on the molecular scale [37], long-time tails will arise in the correlation functions of conserved currents as, e.g., the liquid's velocity field, and the long-range character of the hydrodynamic interaction necessitates very careful studies of the system size dependence of the results. Short of analytic solutions of the problem, the challenge therefore is to find simulation techniques that are on the one hand accurate enough to allow reliable predictions, but on the other hand of sufficient numerical efficiency to permit studies on "large" systems in terms of particle numbers and confining geometry and "long" times with respect to the intrinsic velocities and length scales.

Some techniques, notably finite element or finite volume techniques [22, 34, 49, 51, 69], can reproduce very precisely the behavior of a small number of particles, but they are too computer intensive to simulate in three dimensions inherently collective, many-particle effects as, for example, the influence of the presence of a fluid phase on convection in granular assemblies, the bubbling in fluidized beds, or instabilities associated with gravitational overturning. Recently however, in two dimensions successful simulations of rheological behavior [34, 69] have been performed. The most time consuming part of these algorithms is the recurrent necessity to generate new, geometry adapted grids because continuous distortion of the initial grid will quickly result in very elongated elements or even overlaps with parts of the internal boundary (a particle).

Other techniques can deal with many particles, but use phenomenological expressions [53, 91, 102, 107] for the coupling between particles and fluid that are incapable of rendering correctly single particle behavior and limit severely the predictive power of a method when new parameter ranges are explored. These include also the averaged equation techniques and the Euler-Lagrangian formulations that are popular in turbulent flow

simulations, where direct simulation is prohibitively expensive [96, 99, 102].

Several techniques are based on the assumption of low Reynolds numbers, which turns the Navier-Stokes equation into the linear Stokes equation. Then one exploits the fundamental solution of the Stokes equation to eliminate the need to compute the solution everywhere in space, but rather uses a boundary element formulation [105] or a multipole expansion for the stress on the particle surface [10, 12, 58] possibly together with specific precautions for the divergent near-field lubrication forces [88]. Naive implementations of these methods require the storage and inversion of a full matrix. Only rather complex clustering techniques that exploit the decay of the influence of one particle on the other with increasing distance between the two can reduce this effort to be proportional to the number of particles (apart from logarithmic corrections). However, no efficient boundary integral technique is known to us for the nonlinear Navier-Stokes problem.

The most powerful techniques in terms of the ability to deal with large systems of the described kind have proved to be those that use a *fixed* nonadaptive grid to represent the fluid flow. The particle boundaries can then be represented only approximately as permitted by the regular discretization. Such techniques have been successfully used by Ladd in conjunction with a lattice-Boltzmann flow solver [60, 61] or in Ref. [103] with a more conventional finite difference Navier-Stokes solver.

The method that we propose here follows the immersed boundary technique proposed by Fogelson and Peskin [25]. Similar ideas are also employed in the fictitious domain method developed by Glowinski and co-workers [30, 28, 29] and earlier domain embedding methods [16] about which we learned only after most of this work had been completed. The basic idea of these two approaches is to use the same *constant* grid for the resolution of the fluid flow at all times and represent the particles not as boundary conditions to the flow, but by a volume force term or Lagrange multipliers in the Navier-Stokes equation. The fluid equation can then still be solved by very fast specialized Fourier or multigrid techniques that exploit the regular grid structure.

2.1 Numerical Method

We now describe the essentials of our technique to treat large numbers of rigid particles moving in a fluid modeled by the Navier-Stokes equations. The problem can be quite cleanly separated into three parts: (i) the fluid equations, (ii) the motion of the suspended particles, and (iii) their mutual coupling. Most of the technical details of the first two subproblems can be found in the literature and we will here give only the most important facts for completeness. The way of coupling these two phases will be addressed in more detail.

2.1.1 Liquid

Our starting points are the Navier-Stokes equations describing the motion of a Newtonian fluid with inertia,

$$\rho\frac{\partial\vec{v}}{\partial t}+\rho(\vec{v}\cdot\nabla)\vec{v}=-\nabla p+\eta\nabla^2\vec{v}+\vec{f}. \tag{2.1}$$

Here ρ and η denote the fluid density and viscosity, $\vec{v}$ and p its velocity and pressure, respectively, and $\vec{f}$ a volume force term. As usual [63], we will not consider the time independent gravity contribution to $\vec{f}$ explicitly, but cancel it against the hydrostatic pressure and omit both terms from Eq. (2.1). The corresponding buoyancy forces will be taken into account explicitly in the equations of motion of the suspended particles. However, we will require a fluctuating component of $\vec{f}$ as an essential ingredient of our simulation technique (see below), so that the volume force term must be left in Eq. (2.1). For the following, we will consider the liquid as incompressible, i.e., $\nabla\cdot\vec{v}=0$, and choose the solution method for the fluid equation accordingly. Incompressibility is not a necessary condition for the coupling technique.

We use a staggered marker and cell (MAC) mesh as the base for a second order spatial finite-difference discretization of (2.1), which simplifies considerably the treatment of the pressure boundary conditions [26]. Details can be found, e.g., in Ref. [78], Chap. 6. If we denote the components of the velocity by u, v and w the discretized Navier-Stokes equation is given by

$$\begin{aligned}
\frac{u_{i,j,k}^{(n+1)}-u_{i,j,k}^{(n)}}{\Delta t} &= -\Delta_x(u^2)_{i,j,k}^{(n)}-\Delta_y(uv)_{i,j,k}^{(n)}-\Delta_z(uw)_{i,j,k}^{(n)} \\
&\quad -\Delta_x p_{i,j,k}^{(n+1)}+\frac{1}{Re}\nabla^2 u_{i,j,k}^{(n)}\,, \\
\frac{v_{i,j,k}^{(n+1)}-v_{i,j,k}^{(n)}}{\Delta t} &= -\Delta_x(vu)_{i,j,k}^{(n)}-\Delta_y(v^2)_{i,j,k}^{(n)}-\Delta_z(vw)_{i,j,k}^{(n)} \\
&\quad -\Delta_y p_{i,j,k}^{(n+1)}+\frac{1}{Re}\nabla^2 v_{i,j,k}^{(n)}\,, \\
\frac{w_{i,j,k}^{(n+1)}-w_{i,j,k}^{(n)}}{\Delta t} &= -\Delta_x(wu)_{i,j,k}^{(n)}-\Delta_y(wv)_{i,j,k}^{(n)}-\Delta_z(w^2)_{i,j,k}^{(n)} \\
&\quad -\Delta_z p_{i,j,k}^{(n+1)}+\frac{1}{Re}\nabla^2 w_{i,j,k}^{(n)}\,.
\end{aligned} \tag{2.2}$$

where Δt is the time step and the differential operators are defined by

$$\begin{aligned}
\Delta_x f_{l,m,n} &= \frac{1}{h}(f_{l+1/2,m,n} - f_{l-1/2,m,n}) \,, \\
\Delta_y f_{l,m,n} &= \frac{1}{h}(f_{l.m+1/2,n} - f_{l,m-1/2,n}) \,, \\
\Delta_z f_{l,m,n} &= \frac{1}{h}(f_{l.m,n+1/2} - f_{l,m,n-1/2}) \,, \\
\nabla^2 f_{l,m,n} &= \Delta_x\Delta_x f_{l,m,n} + \Delta_y\Delta_y f_{l,m,n} + \Delta_z\Delta_z f_{l,m,n} \,, \\
\Delta_x\Delta_x f_{l,m,n} &= \Delta_{xx} f_{l,m,n} = \frac{f_{l+1,mn} - 2f_{l,m,n} + f_{l-1,m,n}}{h^2} \,.
\end{aligned} \tag{2.3}$$

We calculate the values of u, v and w located between the grid points by averaging the on-grid values, so that the approximation is still of second order.

The incompressibility constraint is satisfied via an explicit operator-splitting, fractional-time-step method, described in detail in the same reference. In that framework, one introduces an additional provisional "velocity" $\vec{v}^*$ *without physical meaning* in order to split the one velocity equation (2.1) into two,

$$\rho\frac{\vec{v}^* - \vec{v}^n}{\Delta t} = -\rho(\vec{\nabla}\cdot\vec{v}^n)\vec{v}^n + \eta\nabla^2\vec{v}^n + \vec{f}^n \,, \tag{2.4}$$

$$\rho\frac{\vec{v}^{n+1} - \vec{v}^*}{\Delta t} = -\nabla p^{n+1} \,. \tag{2.5}$$

Here, the superscripts n and $n+1$, respectively, denote the values at $t = n\ \Delta t$ and $t = (n+1)\ \Delta t$. This system of two equations is mathematically equivalent to the single equation that we started out with.

An equation for the pressure variable is obtained from Eq. (2.5) by taking the divergence and using that the divergence of the updated velocity field $\vec{v}^{n+1}$ must vanish,

$$\nabla^2 p^{n+1} = \frac{\rho}{\Delta t}\vec{\nabla}\cdot\vec{v}^* . \tag{2.6}$$

The steps above are often considered to be a projection of Eqs. (2.4,2.5) onto a divergence free subspace of the velocity vector field—the pressure equation is used to remove the "perpendicular" velocity components contained in $\vec{v}^*$—and thus the term "projection method" is often employed in this context. The exact distribution of terms to the split equations is not unique; in principle, some of the velocity terms on the right hand side of (2.4) could appear in (2.5). Consequently, the unphysical temporary field $\vec{v}^*$ would take different values, without affecting $\vec{v}^{n+1}$.

The fluid equations must be solved subject to the boundary and initial conditions implied by the confining geometry, in our case a quadrilateral volume which is either (i) limited by fixed walls on which no-slip conditions hold or (ii) periodically repeated in space. To obtain the boundary conditions for Eq. (2.6), we project expression (2.5) onto the

boundary's outward pointing normal $\vec{n}$,

$$\frac{\rho}{\Delta t}\left(v_{\perp}^{n+1} - v_{\perp}^{*}\right) = -(\vec{n}\cdot\nabla)p^{n+1}. \tag{2.7}$$

Let us now consider the spatially discretized forms of Eq. (2.6) and (2.7) in the vicinity of a boundary, as e.g., displayed in Fig. 2.1,

$$\begin{aligned}\frac{1}{h}\left(\frac{p_{1,m}^{n+1}-p_{0,m}^{n+1}}{h} - \frac{p_{0,m}^{n+1}-p_{-1,m}^{n+1}}{h}\right) + \frac{1}{h}\left(\frac{p_{0,m+1}^{n+1}-p_{0,m}^{n+1}}{h} - \frac{p_{0,m}^{n+1}-p_{0,m-1}^{n+1}}{h}\right) \\ = \frac{\rho}{\Delta t}\left(\frac{v_{x;0,m}^{*}-v_{x;\Gamma}^{*}}{h} + \frac{v_{y;0,m}^{*}-v_{y;0,m-1}^{*}}{h}\right)\end{aligned} \tag{2.8}$$

and

$$\frac{1}{h}(p_{0,m}^{n+1} - p_{-1,m}^{n+1}) = -\frac{\rho}{\Delta t}\left(v_{x;\Gamma}^{n+1} - v_{x;\Gamma}^{*}\right). \tag{2.9}$$

Here, h is the lattice spacing of the grid used for the discretization and the suffix Γ refers to values on the boundary.

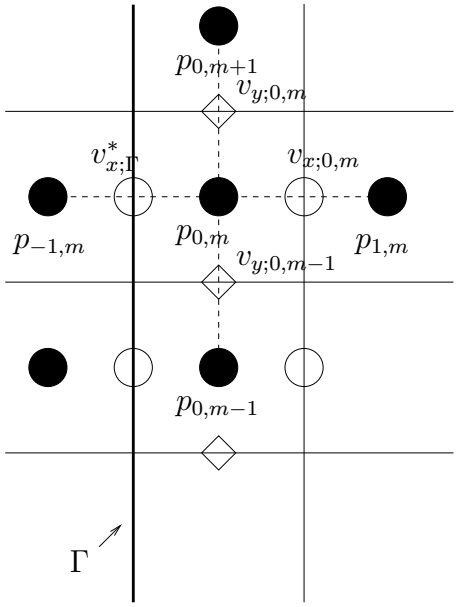

Figure 2.1: Staggered marker and cell (MAC) mesh in the vicinity of a vertical boundary. The pressure $p_{0,m}$ discretization is centered in cell $(0, m)$, the velocities are shifted by half the cell size to the right $v_{x;0,m}$ and upward $v_{y;0,m}$, respectively. The evaluation of the Laplace operator applied to p involves one leg on which the pressure derivative across the boundary needs to be known. This derivative can be replaced by a term that involves both the unknown velocity v_{Γ}^{*} on the boundary and the updated velocity $v_{x;-1,m}^{n+1}$ on the boundary at the same location (not shown).

If we now substitute the expression $(p_{0,m}^{n+1} - p_{-1,m}^{n+1})/h$ from Eq. (2.9) in (2.8), we see that the the value of $v_{x;\Gamma}^{*}$ cancels from both sides of the equation. In other words, the solution of the pressure equation does not depend on the specific values of $v_{x;\Gamma}^{*}$ on the

boundary. For computational convenience, we can thus in particular demand that the left hand side of the equation specifying the boundary conditions shall vanish, i.e., $v_{x;\Gamma}^{n+1} = v_{x;\Gamma}^{*}$, corresponding to vanishing normal derivatives of the pressure across the boundary. Thus, we do not need to know these two values when we solve the pressure equation.

Also, the incompressibility guarantees that we satisfy the integrability conditions for the pressure equation with Neumann conditions:

$$\begin{aligned} 0 &= \oint d\vec{A} \cdot \vec{\nabla} p \\ &\stackrel{!}{=} \frac{\rho}{\Delta t} \int d\vec{x}\, \nabla \cdot \vec{v}^{*} = \frac{\rho}{\Delta t} \oint dA \vec{n} \cdot \vec{v}^{*} = \frac{\rho}{\Delta t} \oint dA \vec{n} \cdot \vec{v}^{n+1} = 0. \end{aligned} \tag{2.10}$$

The actual solution of the pressure equation is effected by a fast multigrid scheme that exploits the regularity of the grid used for discretization. The general idea [35] and details for two dimensions (2D) [53, 82] are given in the literature; the three dimensional (3D) implementation is described in [46]. The hierarchical structure of a multigrid scheme ensures that the time to solve the pressure equation is asymptotically proportional to the number of grid points, a highly desirable feature for large-scale simulations. Since no transform into abstract spaces is necessary as, e.g., in Fourier techniques, multigrid is memory efficient and also well-suited for parallelization by domain composition, as described, e.g., in [104].

One fluid time step hence consists of first computing the provisional velocity $\vec{v}^{*}$ from Eq. (2.4), which provides the information for the source terms of the pressure Eq. (2.6). Next the Poisson problem is solved with Neumann conditions $\vec{n} \cdot \nabla p = 0$ on the boundary where applicable, i.e., for the nonperiodic directions. For uniqueness, we demand that the average pressure is zero. Finally, the pressure values are substituted in Eq. (2.5) to calculate the updated velocities $\vec{v}^{n+1}$.

A local and linear Neumann stability analysis of the numerical scheme neglecting the coupling of the velocity equations by the pressure term leads to the condition

$$1 > \frac{\eta^2}{\rho^2 h^4} \left[\left(\frac{\rho h^2}{\eta} + 2\Delta t \left(d - \sum_{i=1}^{d} \cos(k_i h) \right) \right)^2 + \left(\frac{\rho h}{\eta} \Delta t \sum_{i=1}^{d} v_i \sin(k_i h) \right)^2 \right] \tag{2.11}$$

for linear stability of a standing wave perturbation with wave number k_i; the v_i are the local fluid velocity components. The inequality (2.11) must be satisfied at all discretization nodes and for all wave numbers k_i. We obtain two simpler *necessary* conditions from (2.11) by demanding that the inequality holds for the two squares separately. In the first, we set $cos(k_i h) = -1$ and find

$$\Delta t < \frac{1}{2d} \frac{\rho h^2}{\eta}, \tag{2.12}$$

which is familiar from discretizations of the diffusion equation. Now we define the maximum value of all velocities components over all space, $v_{\max} = \max |v_i(\vec{x})|$, and set $\sin(k_i h) = 1$ in the second square. Then it follows that

$$\Delta t < \frac{h}{d v_{\max}}, \tag{2.13}$$

a term due to the presence of the convective nonlinearity of the Navier-Stokes equations.

2.1.2 Particle-fluid coupling

The most challenging part of the problem is the treatment of the no-slip boundary condition for the fluid on the particle surfaces. We here build on an idea that has been applied by Fogelson and Peskin [25] to the case of viscous flow. Instead of implementing the no-slip boundary conditions by modifying coefficients of the discretized system [90] or employing grid adaptivity as in finite-volume or finite-element techniques, we use the body-force term in the Navier-Stokes equations to implement constraints acting on the fluid such as to mimic the presence of rigid particles at appropriate regions in the flow. These regions will move as the physical particles will and they will comprise sufficiently many grid points in order to represent the geometry of the physical particles. Since the lattice points are spatially fixed, but the particles move, the association of grid points to particle representing regions will change in the course of the simulation.

In more detail, the computation of the motion of a physical particle i is decomposed into two contributions. A moving liquid volume element V_i of the same shape as the particle constitutes the first contribution. Let us for the moment assume that we knew how to move this element rigidly within the rest of the fluid, just as if it were a solid particle of fluid density ρ_{f} with mass $M_i^{\mathrm{l}} = V_i \rho_{\mathrm{f}}$ and moment of inertia $I_i^{\mathrm{l}} = c M_i^{\mathrm{l}} a^2$. For simplicity we assume that we deal with disks or spheres so that I is represented by a scalar, a being the particle radius and $c = 1/2$ or $2/5$ in two and three dimensions, respectively. As will become clear, our approach is not limited to these cases.

The second contribution is a particle template that also has the shape of the rigid physical particle, but it carries the mass M_i^{t}, and the moment of inertia I_i^{t}. These values complement those of the fluid contribution and sum to the values of the physical particle i, i.e., $M_i = M_i^{\mathrm{l}} + M_i^{\mathrm{t}}$ and $I_i = I_i^{\mathrm{l}} + I_i^{\mathrm{t}}$. The particle template is rigid by definition. We like to think of the template motion as representing the particle motion.

To make the general idea work, we must now describe how to achieve a rigid coupling between the template and the associated fluid element. To this end, we first introduce a number n_i of reference positions $\vec{r}_{ij}^{\,r},\ j = 1 \ldots n_i$ distributed over the volume of template

i. The $\vec{r}^r_{ij}$ are vectors relative to the center of mass of template i. The associated spatial coordinates $\vec{x}^r_{ij}$ change only due to the movement and rotation of the rigid template,

$$\vec{x}^r_{ij}(t) = \vec{x}_i(t) + \mathbf{O}_i(t) \cdot \vec{r}^r_{ij}, \tag{2.14}$$

where $\mathbf{O}_i$ describes the instantaneous orientation and $\vec{x}_i$ is the position of the template. In the 2D case, we obtain $\mathbf{O}_i$ by forming the rotation matrix associated with the one angular degree of freedom of the particle, in 3D we use quaternions [3] to represent the particle orientation and to compute the rotation matrix $\mathbf{O}_i$.

Associated with each reference position is a tracer $\vec{x}^m_{ij}, \quad j = 1 \dots n_i$ which tracks the motion of the fluid,

$$\dot{\vec{x}}^m_{ij} = \vec{v}(\vec{x}^m_{ij}). \tag{2.15}$$

Here and in the following we use dots to indicate the time derivative along the trajectories. Please note that the tracers are passively convected with the fluid and do not by themselves constitute new degrees of freedom.

The comparison of the location of the tracer to the position of its reference point allows us to judge whether the fluid volume V_i has changed shape or taken another trajectory as the associated template. The condition of rigid coupling translates into zero offset and zero difference velocity of the tracer and the reference point position. The density and location of the tracers should in general be chosen such that the number of degrees of freedom of the fluid that need to be controlled should equal the controlling number of tracers (please note the pertinent comments at the end of this section). That is to say that each tracer should control a fluid volume of h^d, d being the spatial dimension.

Now we obtain an explicit numerical scheme for the computation of the force density $\vec{f}$ constraining the fluid motion as follows. Whenever between tracer and reference position there occurs a nonvanishing difference in position $\vec{\xi}_{ij} = \vec{x}^m_{ij} - \vec{x}^r_{ij}$ or in velocity $\dot{\vec{\xi}}_{ij}$, we generate an additive contribution $\vec{f}_{ij}$ to the force density in the fluid that tends to drive the liquid and thus the tracer back to the reference position and to diminish their relative velocity. One possible choice is

$$\vec{f}_{ij}(\vec{x}) = (-k\vec{\xi}_{ij} - 2\gamma\dot{\vec{\xi}}_{ij})\delta(\vec{x} - \vec{x}^m_{ij}), \tag{2.16}$$

where k is a "spring" constant, γ a damping constant, and $\delta(\vec{x})$ the Dirac distribution. In our explicit technique, k must be chosen large enough so that $|\xi_{ij}| \ll h$ holds at all times. Similarly, the dissipation introduced by the velocity-proportional friction controlled by γ must be small enough to be negligible against the external physical sources of energy dissipation. The force density $\vec{f}$ in the fluid equation (2.1) is the sum over all particles i and reference points j of $\vec{f}_{ij}$. A slight modification is needed in the case of periodic boundary conditions which will be discussed separately in Section 2.1.4.

We must regularize the δ functions in the first part of the sum (2.16) by, e.g., linearly or quadratically weighted, interpolation to the nearest grid points. For example, in 2D, $\delta(\vec{x}-\vec{x}')$ is "distributed" linearly to the four grid points closest to $\vec{x}'$ with weights $w_{\Delta k,\Delta l}$ according to the perpendicular distances of $\vec{x}'=(x',y')$ from the discretization grid point (x_{kl},y_{kl}) just below to the left. The indices k and l shall here denote grid indices as used in Fig. 2.1

$$\begin{aligned} w_{00} &= \frac{1}{h^2}\left(1-\frac{|x'-x_{kl}|}{h}\right)\left(1-\frac{|y'-y_{kl}|}{h}\right), \\ w_{10} &= \frac{1}{h^2}\frac{|x'-x_{kl}|}{h}\left(1-\frac{|y'-y_{kl}|}{h}\right), \\ w_{01} &= \frac{1}{h^2}\left(1-\frac{|x'-x_{kl}|}{h}\right)\frac{|y'-y_{kl}|}{h}, \\ w_{11} &= \frac{1}{h^2}\frac{|x'-x_{kl}|}{h}\frac{|y'-x_{kl}|}{h}. \end{aligned}$$

Please note that due to the use of a staggered grid, the (x_i,y_i) will in general be different for different components of the force.

The prefactor $1/h^2$ present in the expression for the weights above ensures that the spatial integral over this representation yields unity [91]. Generalization of this formula to quadratic or nth order weights as well as general dimensions d is straightforward,

$$w^{(n)}_{\Delta l_1,\ldots,\Delta l_d} = \frac{1}{h^d}\prod_{i=1}^{d}\left[\delta_{0\Delta l_i}\left(1-\frac{|x_i'-x_{i;l_1,\ldots l_d}|^n}{h^n}\right)+\delta_{1\Delta l_i}\frac{|x_i'-x_{i;l_1,\ldots l_d}|^n}{h^n}\right]. \qquad (2.17)$$

Here, the index i refers to the vector component and the indices l_i the location of the closest grid point whose position components are all just smaller than those of $\vec{x}'$. Larger n tend to concentrate the weight in the grid point closest to $\vec{x}'$. The application of such higher order weights has advantages when the reference points are placed up to exactly the radius of the particle.

Fogelson, Peskin [25] and Stockie [98] use smoother, longer ranged kernels, involving exponentials and trigonometric functions which (i) are numerically more expensive to evaluate and (ii) do not seem to accelerate convergence of the pressure solution even if the source terms are smoother. We consider as the advantage of these kernels their capability to obtain a grid independent limit for the force density and thus the emerging motion if the number of control points is fixed and $h\to 0$.

In order to estimate the largest possible k at a given time step Δt we consider a system of coupled masses. The value of k together with the reduced mass

$$M = \frac{M_i^{\mathrm{t}}\Delta M_{\mathrm{f}}}{M_i^{\mathrm{t}}+\Delta M_{\mathrm{f}}} \qquad (2.18)$$

of the particle template M_i^{t} and the fluid element $\Delta M_{\mathrm{f}} = \rho_{\mathrm{f}} h^d$ at $\vec{x}_{ij}^{\,r}$ introduces a time scale of oscillation,

$$T^{\mathrm{t}} = \frac{1}{2\pi}\sqrt{\frac{M}{n_i k}}, \tag{2.19}$$

which must be resolved by the integration, i.e., $\Delta t \ll T^{\mathrm{t}}$. Only for these sufficiently small Δt, we can guarantee stability and numerical correctness of the particle integration.

For many computations we have adjusted k so that the above inequality is satisfied when Δt is of the order of the diffusive stability limit (2.12) imposed by the fluid integration, i.e.,

$$\Delta t < \frac{1}{2d}\frac{\rho h^2}{\eta}. \tag{2.20}$$

Thus, k can be determined from

$$k = \mathrm{const}\frac{M}{n_i \Delta t^2} \tag{2.21}$$

In our tests that we have performed, stability was always achieved if $\Delta t < \frac{1/20}{T^{\mathrm{t}}}$.

In 2D simulations we have had good experiences with γ values close to aperiodic damping of the particle template—in this case the assumption that the tracer positions are fixed yields $\gamma = \sqrt{k} M_t$. This has often eliminated small, but unphysical oscillations of the particles, in particular in the beginning of the simulations. These oscillations do not indicate instabilities of the numerical scheme, but reflect the oscillatory time scale resulting from template mass and coupling constant k.

In 3D simulations, probably due to the larger number of control points, $\gamma = 0$ seems to suffice. Our empirical experiences concerning the admissible maximum number of tracers are not conclusive. Whereas in dynamical simulations with moving particles it seems often possible to increase the number beyond the number of grid cells within one particle volume, in low-Reynolds-number computations with *static* particle arrangements, we often need to decrease the tracer density to be slightly below this limit to avoid instabilities.

Since the strongest gradients of the stress occur on the particle surface, computational efficiency suggests to reduce the tracer density in the particle interior. Moreover, in the viscous regime, the inertial effects due to the fluid in the interior of each particle domain are negligible. Interior tracers are only necessary to resolve changes in the angular velocity accurately. These will be important if significant changes in the angular velocity occur on time scales shorter than those for the diffusion of vorticity across the particle diameter, i.e., when we leave the regime of validity of the quasistatic approximation. For particle Reynolds numbers of about 1 and sufficiently small concentrations $\Phi \lessapprox 0.2$, where it follows from the work of Goldman et al. [31] that effects from the rotational motion in

viscous suspensions are generally weak, we consider the neglect of interior tracers justified.

2.1.3 Particle motion

The constraint force distribution that we have introduced to guarantee quasi rigid fluid motion must be cancelled by opposite equal terms acting on the particle templates so that only external forces remain in the momentum balance of the combined system. This cancellation is quite naturally achieved by applying Newton's second law to the "spring" associated with each reference-point-tracer pair. That is to say that

$$\vec{F}_{ij} = k\vec{\xi}_{ij} + 2\gamma\dot{\vec{\xi}}_{ij} \tag{2.22}$$

is the force acting on particle template i at the location of reference point j. Similarly, the angular momentum balance will be satisfied when we take the torque to be

$$\vec{\tau}_{ij} = (\vec{x}^r_{ij} - \vec{x}_i) \times \vec{F}_{ij} \tag{2.23}$$

with respect to the template center of mass $\vec{x}_i$.

As further contributions single particle forces, gravity and buoyancy need to be taken into account,

$$\vec{F}^s_i = -M_i g\vec{e}_z + \rho V_i g\vec{e}_z = (\rho - \rho_p)V_i g\vec{e}_z, \tag{2.24}$$

where we have used ρ_p for the particle density and V_i for its volume (or area in 2D).

We now need to address the question of direct particle-particle interactions. In most non-Brownian suspensions these are negligible compared to the hydrodynamic effects at short distances between particles. For example, the approach of two particles is very strongly damped by the hydrodynamical lubrication forces between the two surfaces (see, e.g., [20]). Numerically these forces will be strongly underestimated when the distance between two particles becomes of the order of the lattice spacing. It is clear that all fixed grid techniques (including lattice Boltzmann) show this shortcoming, but even off-lattice particle methods (as DPD) similarly underestimate the lubrication forces because the model intrinsic mean free path sets a length scale below which viscous stresses cannot be properly represented.

We model surface contacts between particles—and solve at the same time the numerical problems arising from possible large particle overlaps—by introducing a pairwise repulsive force that acts when the centers of two particles come closer than the sum of their radii

a_i+a_k. Let the overlap between particles i and k be defined as $\vec{\zeta}_{ik} = (a_i+a_k-|\vec{x}_i-\vec{x}_k|)\vec{e}_{ik}$, with $\vec{e}_{ik}$ denoting the unit vector pointing from k to i. Then we take the force on i to be

$$\vec{F}^p_{ik} = -k_p\vec{\zeta}_{ik}. \tag{2.25}$$

In a similar manner, one may consider explicit interaction terms to restore the correct forces on the particles at short distances $\lessapprox h$ [61, 91]. However, our results indicate that in the studied concentration range the lubrication effects are recovered to a sufficient degree by our numerics. At increasing concentrations, such corrections will be of crucial importance [72].

The total force $\vec{F}_i$ on particle template i is the sum $\vec{F}_i = \vec{F}^s_i + \sum_k \vec{F}^p_{ik} + \sum_j \vec{F}_{ij}$. Apart from the fluid reaction force $\vec{F}_{ij}$, which also describes the "unphysical" constraint forces, (cf. Sec. 2.1.2), these terms are those that we expect for a "physical" particle to be present.

A Velocity-Verlet integrator [3] serves to integrate the equations of motion for the translation of the template,

$$\ddot{\vec{x}}_i = \vec{F}_i/M_i \tag{2.26}$$

and a Gear-predictor-corrector integrator of fourth order [82] for the rotation. For the quaternion formulation of the rotation, we refer the reader to Ref. [3].

To briefly summarize the above, we would like to stress again that the modeling of a rigid, heavy particle requires the (i) "freezing" of the region of fluid occupying the space of the particle and (ii) the coupling of this region to a particle template whose dynamical properties supplement those of the fluid in such a fashion that the coupled system behaves just as the modeled particle would. The arguments above can be put in a slightly more stringent mathematical context, for which we refer the reader to the appendix of this paper.

2.1.4 Treatment of periodic systems and driving

In order to minimize effects from rigid walls it is often convenient to study periodically repeated cells. Periodicity in the following will always mean periodicity *in space* only. One should be aware, however, that the long range nature of the hydrodynamic interactions might cause some artifacts in this case [55], mainly increasing auto-correlation times associated with the vertical motion.

Gravity, or an imposed driving pressure gradient single out one specific direction, say the vertical. Whereas periodic boundary conditions pose no additional difficulties for the solution of the fluid and particle equations *perpendicular* to that direction, we need to specify more precisely what we mean by periodicity *parallel* to it. We will here consider

the case of driving the system gravitationally via the density difference of particles and fluid.

For the fluid velocity field we require periodicity of the solution across the horizontal system boundary in z direction, i.e., $\vec{v}(\vec{x} + NL_z\vec{e}_z) = \vec{v}(\vec{x})$, where N is an arbitrary integer and L_z the size of the system in z direction. Similarly, the particle positions and associated velocities can be periodically extended.

If we consider the case of a section of a vertically positioned tube, then we can also demand the pressure to be a function periodic with period $L_z\vec{e}_z$. Due to the periodicity of $\vec{f}$ arising from the (periodic) particle motion and the periodic velocity field, the source term of the pressure equation is also periodic, the integrability conditions are satisfied and we obtain a periodic solution for the pressure which is unique up to a constant which we choose so that the average pressure vanishes. Physically, this system will evolve towards a statistically stationary state in which on average the viscous forces originating at the walls balance the gravitational driving.

In the case of sedimenting systems, it is however more natural to imagine the simulation cell as a small part of a larger system. In this case, there are no walls that could provide balancing viscous forces to counteract the gravitation. The least constraining condition on the system that still guarantees evolution to a stationary state is to assume that there is no net acceleration at any time on the components within the considered cell. That is to say, that at any time, we must make sure that the integral over the simulation volume of the right hand side

$$\frac{D}{Dt}\rho\vec{v} = \underbrace{-\vec{\nabla}p}_{(I)} + \underbrace{\eta\nabla^2\vec{v}}_{(II)} + \underbrace{\vec{f}}_{(III)} \tag{2.27}$$

of the Navier-Stokes equation (2.1) vanishes. Now, for the term (II) we apply Gauss's theorem and find that it depends only on the values of the velocity gradient tensor integrated over the surface of the cell. Since the velocity field is periodic, contributions from opposite faces cancel identically and this term is always zero. If we decompose the pressure into (i) a linearly varying part and (ii) a purely periodic contribution, then for similar reasons, the volume integral over the gradient of the periodic part vanishes.

Thus we are left with contributions from the integrated force density (III) and an average pressure gradient (I), which arise in addition to the well-known hydrostatic part. If we take these two time dependent terms to be equal—in formal analogy to the hydrostatic case—then they cancel from Eq. (2.27). The total acceleration of the fluid in the simulation volume thus vanishes.

For computational purposes, we simply subtract from the field $\vec{f}$ its spatial average and

thus obtain fluid and pressure equations that allow spatially periodic solutions.

$$\vec{f}(\vec{x}) = \sum_{ij} \vec{f}_{ij}(\vec{x}) - \frac{1}{V}\int_V d\vec{x} \sum_{ij} \vec{f}_{ij}(\vec{x}) = \frac{1}{V}\sum_{ij} F_{ij}. \tag{2.28}$$

Physically, we can think of the associated constant pressure gradient

$$\nabla p_{\text{lin}} = \frac{1}{V}\int d\vec{x}\ \vec{f}, \tag{2.29}$$

which drops from Eq. (2.27), as giving rise to a buoyancy force. This buoyancy force, however, is already correctly included in the "tracer-spring" forces appearing in the particle equations of motion (cf. Sec. 2.1.3), since we would reduce the tracer forces by their average and add the same term again, now in the form of a buoyancy contribution from the liquid.

2.1.5 Summary of the numerical procedure

We now briefly summarize the sequence of steps described above that are necessary to perform one time step in our simulation.

1. We perform the predictor part of the Gear algorithm for both the template and marker positions. No forces need to be known at this point, because the prediction is solely based on Taylor coefficients of the trajectories which were previously recorded.

2. Likewise, we update the quaternions and the angular velocity representing the degrees of freedom of rotation of each template. We then use their values to compute the rotation matrix $\mathbf{O}_i(t)$ to find the predicted location of the reference points [cf. Eq. (2.14].

3. From the predicted particle template location the interparticle forces are computed according to Eq. (2.25).

4. Now we are in a position to compare the predicted tracer positions to the predicted reference point locations and infer the constraint forces $\vec{f}_{ij}$ necessary to impose rigid motion on the fluid [(Eq. 2.16)]. The integration of $\vec{f}_{ij}$ over its support and summation over all tracers associated to template i yields the reaction force of the fluid onto the template. Similarly, we determine the acting torque using Eq. (2.23).

5. Knowing the force distribution $\vec{f}_{ij}$ and the fluid velocity field, we now know all terms on the right hand side of Eq. (2.4) and can perform a fluid update by

(a) calculation of the provisional "velocity" field $\vec{v}^*$, from the current velocities $\vec{v}^n$ and the constraint forces $\vec{f}_{ij}$,

(b) determination of the pressure from the Poisson equation (2.6) by a multigrid procedure,

(c) and finally by advancing the fluid velocity to $\vec{v}^{n+1}$ from the knowledge of the pressure field and the "old" velocities $\vec{v}^n$ [Eq. (2.5)].

6. From the predicted tracer positions and the new fluid velocity values we obtain the correction terms for the tracer trajectories necessary for the second (correction) part of Gear's integrator for the tracers [Eq. (2.26)].

7. Similarly, a correction step is performed for the translational and the angular velocity of the templates using the previously computed torques and forces. The corrected angular velocity will then be used to correct the quaternion values that trace the orientation of the particle (Sec. 2.1.3).

At this point we have completed the time step and can perform measurements on a consistent set of dynamical quantities.

2.2 Validation of the Navier-Stokes solver

The Navier-Stokes solver outlined in Sec. 2.1.1 has been tested on the limiting stationary flow pattern in the driven-cavity problem [11] for Reynolds numbers on the box scale of $Re = UL\rho/\eta < 100$, where U denotes the scale of the imposed velocities. As time dependent flows we have tested sinusoidal velocity profiles between parallel plates and verified the exactly exponential approach to rest and the associated decay constant.

Due to the explicit method and the inherent "diffusive" stability constraint, $\Delta t < \rho h^2/2d\eta$, very low-Reynolds-number calculations $(\eta \to \infty)$ require increasingly shorter time steps and will become prohibitively expensive. However, this limitation can be overcome by an implicit time stepping, possibly exploiting that the Navier-Stokes equations turn into the linear Stokes equations for $Re \to 0$.

We do not think that it is practical to use the proposed method in many particle systems (order of 10000) beyond Reynolds numbers *on the particle scale* larger than $Re = \rho a U/\eta = 10 \ldots 20$, because the flow on and below the Kolmogorov scale must be resolved. In this regime the grid refinement for methods without turbulence modeling will soon render the computational effort unacceptable.

It should also be noted that modern implicit and adaptive-grid methods are more suitable for high precision computation of time dependent pure fluid flows in *static* geometries. In the context of model building for suspension flows with *moving particles* however, fixed grid methods do not require remeshing. Moreover, an explicit technique like the one proposed above provides great flexibility to implement particle-particle interactions, i.e., additional short-range attractive forces of van der Waals type to model aggregation phenomena, or material properties of the particles.

2.3 The case of one particle: cubic periodic arrays

2.3.1 Setup

As the first test case in which boundary conditions on the particle surface have a non-trivial influence on the flow we consider a fluid passing through a cubic periodic arrangement of fixed spheres at low Reynolds numbers. The arising flow has been analyzed in the point particle approximation by Hasimoto [41] for small volume fractions Φ. Among others, Ladd [58] as well as Sangani and Acrivos [89] have considered larger volume fractions up to the limit of $\Phi = \pi/6$ with numerical methods in the viscous regime. More recently, Koch and Ladd [54] have published results for cylinder arrays at moderate Reynolds numbers using lattice-Boltzmann techniques.

To this end, we impose at each point of the grid at first a constant acceleration $\vec{f} = \vec{e}_z \Delta P/L$ corresponding to a constant pressure drop $\Delta P/L$ over the length L of the cubic cell. Periodic boundary conditions are used on the fluctuating, non-linearly increasing part of the pressure and the flow velocities. The particle positions and orientations are fixed to be the initial ones.

The simulations are performed in 2D and 3D as dynamical calculations starting from a fluid field at rest until a steady flow state results. The approach to stationarity is slower at lower solid volume/area fractions. In 3D, we stop when an exponential approximation indicates that the expected additional changes to the flow rate are less than a fraction of 0.02. In 2D, we have adjusted the pressure drop during the simulation to obtain constant volumetric flow rates and thus constant Reynolds numbers.

The drag force $\vec{F}_D$ on one particle is determined by summing the contributions from all the corresponding reference-point-tracer pairs according to Eq. (2.22). If we divide the modulus $F_D = |\vec{F}_D|$ of the drag force by the volumetric flow rate U,

$$U = \frac{1}{V} \int d\vec{x}\; v_z(\vec{x}) \tag{2.30}$$

obtained by averaging the flow velocity over the cell volume V, and refer the value to that of an isolated sphere, then the dimensionless drag coefficient

$$\chi_D = \frac{F_D}{6\pi\eta a U} \tag{2.31}$$

results.

In 2D, F_D is the drag force per unit length of the cylinder. We refer it to ηU which has the required units of force per unit length,

$$\chi_D = \frac{F_D}{\eta U}. \tag{2.32}$$

Both these drag coefficients are known to have corrections $O(Re^2)$ in arrays which have reflection symmetry with respect to the axis of the flow [54, 71].

Similarly, the rotational drag coefficients can be computed by imposing constant angular velocities on the particles and letting the flow adjust. In the viscous regime, both in 2D and 3D, the torque is proportional to the angular velocity. In 3D, we refer the resulting torque on the sphere to the theoretical value of an isolated sphere

$$\chi_R = \frac{\tau_R}{8\pi\eta a^3\omega}. \tag{2.33}$$

In 2D, the theoretical value of the torque per unit length on an isolated cylinder in an infinite medium is $4\pi a^2\eta\omega$, so that a dimensionless drag coefficient

$$\chi_R = \frac{\tau_R}{4\pi a^2\eta\omega} \tag{2.34}$$

can be defined.

2.3.2 Mesh size dependence

Due to the lack of adaptivity at the particle surface, we expect the effective hydrodynamic radius of the particles to be slightly larger than the geometrical radius of the reference point arrangement, because each point controls a fluid volume of extent h^d reaching beyond its geometric location by $h/2$ in each direction. In fact, if the confining radius of the reference point placement is taken to be the geometric template radius, then we measure as a function of mesh size the drag coefficients shown in Fig. 2.2, here $\Phi = 0.0335$. We see that indeed the values extrapolate to asymptotic values as $h \to 0$ with leading error proportional to h.

We can thus improve the accuracy of the simulation by taking this effect explicitly into account [61] by modifying the placement of the reference points. Let us write for the effective hydrodynamic radius a_{eff}, assuming that Δa is linear in h,

$$a_{\text{eff}}(h) = a + \Delta a(h) = a + mh. \tag{2.35}$$

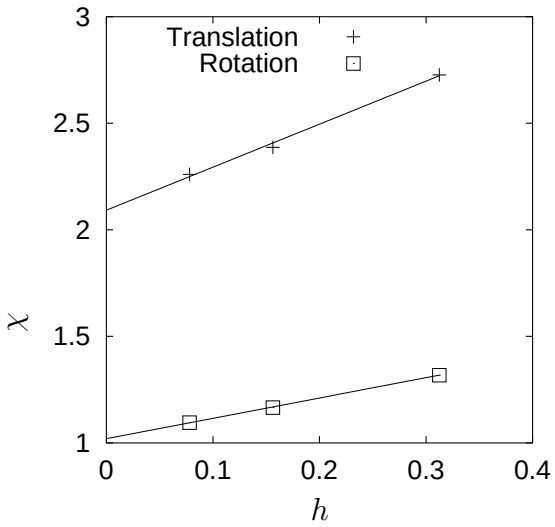

Figure 2.2: Dependence on mesh size h of the dimensionless translational $\chi_D/6\pi\eta a$ and rotational friction coefficient $\chi_R/8\pi\eta a^2$ in three dimensions, denoted by symbols + and $\boxdot$, respectively. The values are for a volume fraction of $\Phi = 0.0335$ at $Re \to 0$. It can be seen that the necessary correction to the drag coefficient is linear in h.

The dependence of the friction coefficient on the volume fraction can be Taylor expanded around the volume fraction corresponding to a particle with radius a,

$$\begin{aligned} \chi(\Phi(a_{\text{eff}})) &= \chi(\Phi(a)) + \chi'(\Phi(a))\Phi'(a)\Delta a(h) \\ &= \chi(\Phi(a)) + \chi'(\Phi(a))\Phi'(a)mh. \end{aligned} \tag{2.36}$$

Comparing the slope in Fig. 2.2 to the prefactor of h, and using the derivative $\chi'(\Phi(a))$ from the literature [58], we find $m \approx 0.3$. This value holds for 3D and quadratic $n = 2$ interpolation scheme for the δ functions in the force density [cf. Eq. (2.17)]. For the dynamical simulations in the next section, we therefore retract the tracers by an amount of $0.3h$ from the geometric surface; in 2D we use $m = 0.5h$ with $n = 1$ interpolation.

2.3.3 Translational drag and rotational friction coefficients

In Fig. 2.3 we show the results of the extrapolation to $h = 0$ of the translational drag for 2D and 3D. In 3D we compare with Ladd's [58] numerical solutions of the Stokes equation with the same boundary conditions. In 2D, we compare to the results of Sangani [89].

In the 3D simulations the pressure drop is adjusted during the simulation to achieve the same volumetric flow rate (and thus Reynolds number) independent of volume or area fraction of the obstacles. In 2D, the Reynolds number based on the flow rate and the radius of the obstacle does not exceed 0.1.

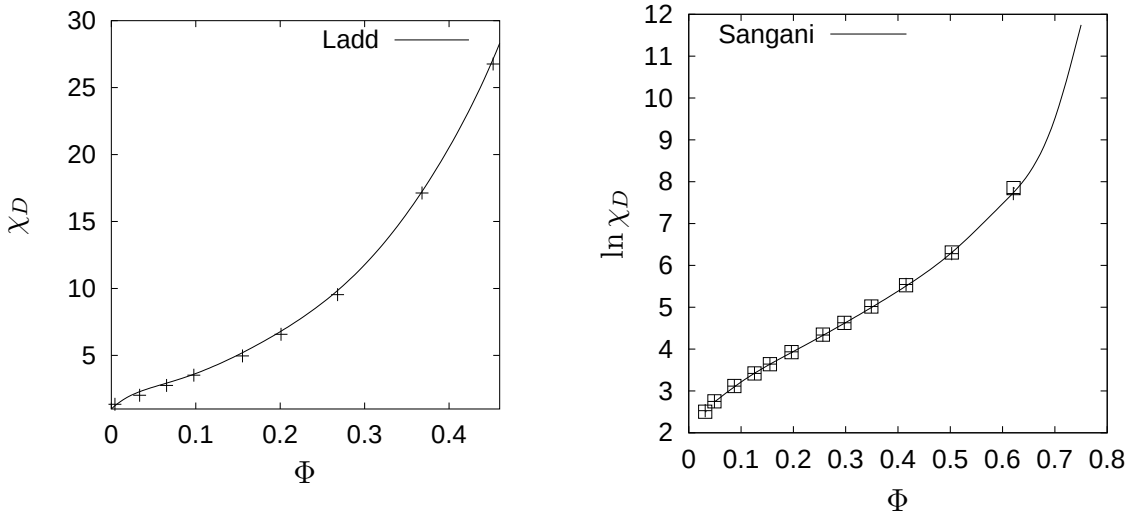

(a) (b)

Figure 2.3: (a) Drag coefficient χ_D in (a) a periodic, 3D simple cubic arrangement of spheres. (b) Natural Logarithm $\ln \chi_D$ of the drag coefficient in an array of cylinders for two different unit cells that are expected to yield the same resistance to flow. The solid line in (b) is a cubic spline through the logarithm of the semi-analytical results for the friction coefficients given in Ref. [89].

In Fig. 2.4 the corresponding results for the rotational friction coefficients χ_R are shown as functions of volume and area fraction. In two dimensions different symbols denote different arrangements of the cylinders with respect to the discretization. In one case the particle is located at position (0,0) in the cell of size $L \times L$, in the other the unit cell was chosen to include two particles, one at (0,0), the other at $(L/2, L/2)$. The symmetries of the array imply that in both cases the same scalar friction coefficient must result.

In both 2D and 3D, we have computed the drag coefficients by linear interpolation to $h = 0$ of the h-dependent results. For the densest packings in 2D, the gap between the particles is about 13 grid cells wide for the finest grid used. The relative difference of the friction coefficients computed for the two finest grids (13 grid cells and 6 grid cells across the gap) is about 0.04. Table 2.1 summarizes the numerical results for the rotational drag in the cylinder array for which we did not find values in the literature available to us.

2.4 Sedimentation velocity as a function of volume fraction

The measurement of the sedimentation velocity of an ensemble of many spheres as a function of the volume fraction constitutes a more realistic test than the two above. As

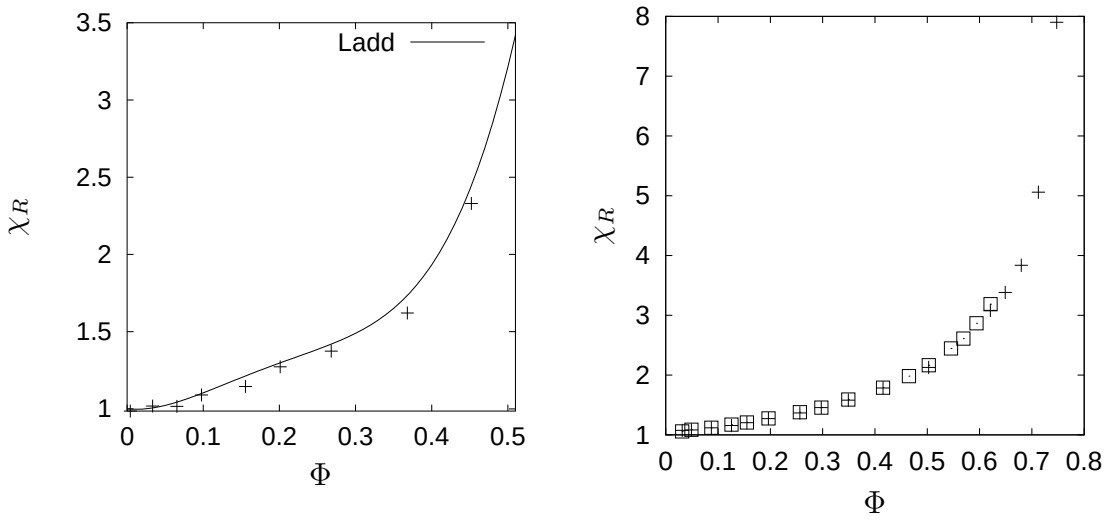

(a) (b)

Figure 2.4: Rotational friction coefficient χ_R in a periodic arrangement of (a) 3D spheres, (b) 2D cylinders. In 3D, the solid line is a cubic spline through the numerical results of Ladd [58].

Φ	$\chi_R = \tau_R/4\pi a^2\eta\omega$
0.0314	1.07
0.049	1.08
0.0872	1.11
0.125	1.15
0.155	1.2
0.196	1.27
0.256	1.36
0.297	1.45
0.349	1.58
0.415	1.78
0.502	2.12
0.62	3.08
0.649	3.38
0.679	3.83
0.712	5.05
0.747	7.9

Table 2.1: Dimensionless resistance to rotation in an array of cylinders at $Re = a^2\omega\rho/\eta = 0.1$.

in the case of the fixed sphere arrangement in the two preceding tests we choose periodic boundary conditions on our sample cell that now, however, contains many spheres whose position and orientation can evolve dynamically without artificial kinematic constraints. Gravitation acts as the driving force via the density difference of particles and fluid. It was chosen such that the Reynolds number on the particle scale of a single sedimenting particle, in 3D,

$$Re = \frac{2}{9}\frac{a^3}{\eta^2}\rho(\rho_p - \rho)g \tag{2.37}$$

is about 0.1. In 2D, we assured by test simulations on single falling discs that we are in the same range of Reynolds numbers.

As motivated in Sec. 2.1.2, we use only one shell of tracers such that their hydrodynamic radius equals the geometric radius of the template. Their number is taken to be the integer part of $4\pi a^2/h^2$, i.e., approximately equal to the number of fluid volume elements on the surface of each particle.

The mean sedimentation velocity U_s is measured in experiments either as the velocity with which the upper front of the particle rich phase settles or, when single particle velocities can be measured, as the mean velocity of the particle phase. We will here adopt the latter method because we cannot observe concentration fronts in a periodic simulation cell,

$$U_s = \frac{1}{N}\sum_{i=1}^{N}\vec{U}_i \cdot \vec{e}_z. \tag{2.38}$$

To obtain a dimensionless quantity, we refer the value of U_s to the velocity U_0 of a single falling particle in the same cell. This procedure takes some corrections due to finite cell size and Reynolds number into account.

Fig. 2.5 shows the results for the sedimentation velocity as a function of volume fraction for 2D and 3D. In 3D we compare to the empirical law of Richardson and Zaki

$$U_s/U_0 = (1-\Phi)^n, \tag{2.39}$$

with $n = 5.0$. We see good agreement to the experimental findings in the viscous regime which find values of $n = 5 \ldots 6$ [75].

In 2D, the computation of a hindered settling function is a somewhat academic exercise which we have done to juxtapose the results to the 3D ones. We have fixed the Reynolds number for the single cylinder experiment to 0.1 on the particle scale. We vary the area fraction, keeping all other parameters constant. The mean settling velocity as a function of area fraction is then been computed and normalized by the single particle value.

In 2D, the best fit of a Richardson-Zaki like law yields an exponent of $n \approx 3.8$, substantially smaller than in 3D. The effect of a lower n in 2D has been seen before using

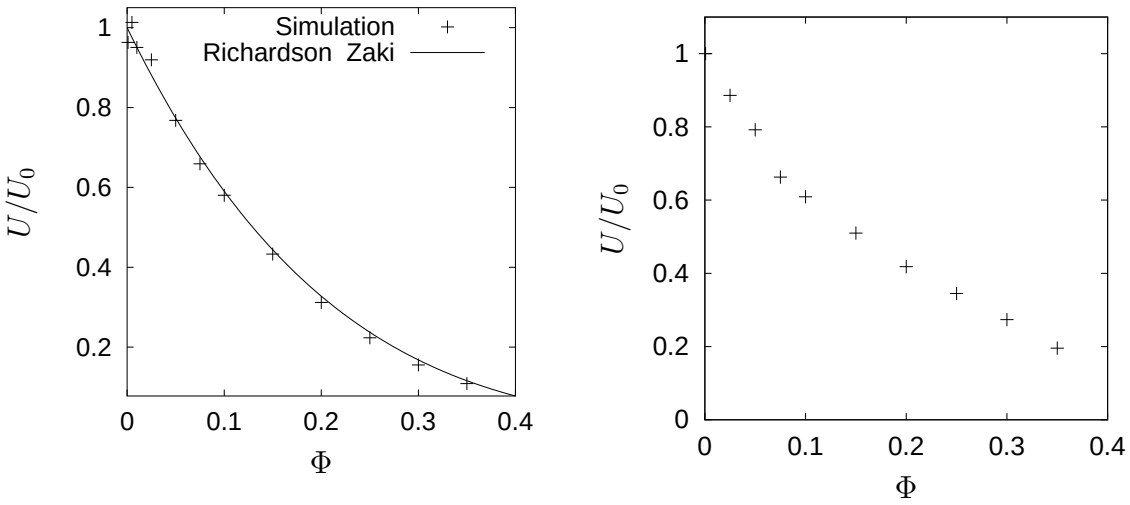

Figure 2.5: Sedimentation velocity in a periodically repeated cell: (a) 3D, (b) 2D. The action of gravity is counteracted by a constant pressure gradient in the opposite direction, such that at all times the volume flux across a horizontal cut through the cell vanishes. The size of the 3D cell is $12a \times 12a \times 12a$, that of the 2D cell $64a \times 64a (h = 0.25)$. Both simulations are performed at a Reynolds number of approximately 0.1 on the particle scale (for single particles falling)

point-force approximations for the suspended particles [52]. However, the fit to such a power law is only motivated by the analogy to 3D and is in fact not convincing. Most of the difference at larger volume fractions might be related to the area fraction of the random loose disk packing in 2D (≈ 0.7) as compared to the smaller value of the random loose sphere packing in 3D (≈ 0.6), where we expect the sedimentation velocity to drop to 0 [73].

2.5 Some Numerical Questions

2.5.1 Performance Data

As described in Sec. 2.1 our method requires the time stepping of the Navier-Stokes equation, the computation of the tracer movement with two interpolation steps for the fluid velocity and force density, and the integration of the ordinary differential equations that describe the particle motion. For this latter part, we use a linked-cell technique to reduce the determination of the particle contact forces to an $O(N)$ problem in the number of particles. The time spend in this part of the algorithm is only a few percent of the total

computation time and is negligible.

Because the exact ratio of time spent in the fluid-solver and in the coupling between the fluid and the particles depends on various parameters, as e.g. the mesh size h, the volume fraction Φ and the number of tracers per particle, we just want to give an example for the computational cost of a typical simulation done to calculate the sedimentation velocity of a suspension. In this particular case we used $65^3 \approx 2.7 \times 10^5$ fluid grid points and $h = 0.375$. Thus the cell was of a cube with edges of approximately 24 particle radii length. A volume fraction of $\Phi = 0.1$ corresponds therefore to 331 particles with 93 tracers each, representing a total of $30\,783$ tracers.

One time step of this system takes on average 2.6 seconds on a Digital Personal Workstation 433au. The fluid solver needs about 54% and the coupling code 35% of the time. The rest was spend in miscellaneous statistical calculations, file input/output, etc. The computation of particle interactions and the trajectory integration requires less than 1% of the total CPU time.

In other words, per time step we spent about $5.1 \times 10^{-6}s$ on each grid point, about $29 \times 10^{-6}s$ on each tracer and about $50 \times 10^{-6}s$ on each suspended particle. The memory requirements sum up to 80 bytes per tracer and 120 bytes per fluid grid point, including the data structures necessary for the implicit pressure update.

2.5.2 Comparison to other techniques

Particle Methods

As we have seen, the major challenge of direct suspension simulation is the proper representation of moving boundaries in conjunction with numerical efficiency. Since particles are naturally described in a Lagrangian picture by comoving dynamical variables, one could justifiably ask why not to go the whole way and also use Lagrangian techniques for the fluid. This is even more true as the Navier-Stokes equations result as the continuum limit of the average motion of particle systems under quite general circumstances [40]. The following issues should be considered:

1. the implementation of a pure Lagrangian technique is cleaner and more straightforward from a technical point. At the same time, even very simple interparticle potentials (as in the dissipative particle dynamics method (DPD) or in direct simulations of, e.g., Lennard-Jones systems) require a lot more computational effort than the treatment of a grid node in a Navier-Stokes solver. Our experiences point to factors of $3 - 5$ for structureless particles with linear spring interactions as compared to one Navier-Stokes node in 3D.

2. in general, it is not simple to predict the average material properties of the particle phase from the properties of the interaction. One strong point of DPD with respect to other computational methods is the theoretical knowledge that has been collected in the recent past about how the microscopic simulation parameters control the macroscopic properties of the DPD liquid. However, as the discussion about modeling heat conduction within the DPD framework has shown, such extensions require quite considerable contrivances and yet often material parameters of the pure suspending phase have to be determined *a posteriori* from the simulation before the properties of the multi-phase system can be determined.

3. in particle codes, one often takes the route to model larger or different particles by gluing together several (constituent) particles of the type constituting the solvent phase [81]. Such an approach is convenient and efficient because it normally does not require special measures to track the orientation or the translation of the composite particle, because these can be reconstructed from the position of the glued particles. Also, the interactions between the solvent and the constituents of the composite complex particles are often of the same nature as those between the solvent particles and can thus be computed in the same fashion without changing the structure of the simulation program.

   However, this convenience comes at the price of computing *pair* interactions between the constituents to fix the shape of the composite particles. In contrast, the marker-template coupling is a *single* particle interaction.

   Of course it is also quite possible to connect the constituents of a solute particle to a shape preserving (possibly massless) rigid template as has been suggested here for the fluid-particle coupling. This approach seems to have been taken in the DPD framework by a technique used in Ref. [9].

4. In general one must be aware of proper scale separation. For example, the discrete nature of the particle phase introduces a “noise” term which causes fluctuating motion of the suspended particles. This noise can be considered a feature if simulations at low Peclèt numbers shall be performed (as the Lennard-Jones simulations by Rapaport [44]) but must be eliminated in one way or the other in the limit of large Peclèt numbers. Similarly, the discrete nature of the solvent particles will cause breakdown of lubrication forces when the solute particles approach surface-surface distances closer than the mean free path (Knudsen length) of the solvent, as we have discussed in the context of lubrication force modeling in Sec. 2.1.3 for fixed grid methods.

5. Particle codes with short-ranged interactions, similar to explicit lattice-Boltzmann techniques, display a built-in compressibility of the solvent phase. The speed of

sound in these simulations is often very small because the particle interactions are taken to be rather soft in order to allow (apparently) large time steps. In contrast, in continuum techniques one has efficient methods to impose incompressibility (solving a Laplace equation for the pressure equation in our case) or to resort to penalty techniques [78] that effectively replace the long-range Laplace solver by introducing an artificially compressible material law.

Fixed lattice based methods

If instead of using a particle technique one attempts to solve a continuum equation for the fluid phase then one has considerable freedom in the choice of solution methodology and in the choice of the phenomenological parameters entering the equation. Every numerical solution of a continuum equation requires a discretization of the computational domain. If a high precision of the solution is required, the discretization is often taken on an unstructured grid and locally refined in the course of the solution process. The computational drawbacks are the complex data structures required and the entrained computational cost.

In addition, since particle-fluid systems are characterized by moving boundary conditions, a remeshing of the computational grid must occur when it is distorted to such an extent that the requirements of the, e.g., finite-element or finite-volume technique cannot longer be met.

As we have outlined in the introduction of this paper, it is thus advantageous for the simulation of many-particle systems and if the demands on the precision of the solution are not too high, to pick a nonadaptive, regular grid to discretize the continuum fluid equation. On such a lattice we can for example use the lattice-Boltzmann technique, a finite-difference compressible or incompressible Navier-Stokes or Stokes solver, certain lattice gas automata, etc.

As in particle methods, certain issues should be kept in mind:

1. Perhaps the most problematic point is the implementation of the no-slip conditions on the particle surfaces and the computation of the stresses. Concerning the matching of the particles to the grid, considerable freedom exists and includes

   (a) (first order) discretization of the particle surface on appropriate grid nodes or links of the respective technique [60, 87, 104] (first order),

   (b) smoothly varying “interpolation” coefficients to obtain a better, possibly second order accurate estimate of the local influence of the boundary; for lattice Boltzmann, cf. Ref. [23], for finite differences Ref. [90].

Similarly, boundary stresses must be evaluated. For lattice Boltzmann, typically the knowledge of the change of the velocity population associated with a boundary link or node is required, whereas the stress evaluation for finite differences involves direct evaluation of the stress tensor using local pressure and velocity. Please note that in our method none of the above steps is necessary, as the penalty forces on the fluid include the stresses that are determined already in the course of the fluid time step.

2. Depending on the type of discretization used, stabilization measures need to be taken. The explicit lattice-Boltzmann described in [60] requires time averaging (over two time steps) of the torque to avoid instabilities. Nonstaggered finite difference grids may show grid decoupling instabilities. Also the general stability constraints from linear analysis of all explicit methods have to be considered, most notably the Neumann diffusive criterion linking time step and square of the grid size.

3. In most modern (explicit or implicit) methods the computational effort to perform one time step is proportional to the number of discretization "cells" that represent often a set of variables describing the local configuration of the continuum. For example, in our method, the explicit part of the Navier-Stokes time step and the implicit solution of the pressure equation both have this property. Likewise, lattice-Boltzmann methods require only a reweighting of locally available information to update the local velocity histogram. So, the computational effort differs due to the constant of proportionality. An explicit lattice-Boltzmann technique can most directly be compared to a penalty technique for incompressible flows [78], which are of similar computational complexity.

4. The inclusion of energy conservation into a lattice-Boltzmann scheme, which is necessary to compute heat flow, is to our knowledge still an open question [2, 84]. There is no comparable difficulty when using directly discretized flux-conservation equations as, e.g., the Navier-Stokes equation for the momentum flux.

To summarize the above, in suspension physics there is not one single simulation method that addresses the entire spectrum of possible conditions, with or without fluid inertia, with or without particle inertia, low or high Peclèt numbers, constitutive properties of the suspending fluid, constitutive properties of the suspended phase (surface tension, elasticity, additional interactions), particle geometry, etc. with flexibility and efficiency. As we have stated in the introduction, the niche for the fixed grid method presented here is computation at moderate or zero Reynolds number with likewise good to moderate accuracy depending on the price in processing time that one is willing to pay. In that respect it is very similar to the lattice-Boltzmann methods [58, 60, 61].

Brownian motion

The Navier-Stokes describes the evolution of average velocity and pressure and is thus naturally suitable for systems at high Peclèt numbers where no information about the discrete nature of the fluid and the associated fluctuations is required.

On the other extreme, molecular simulation captures all fluctuating quantities as well as their spatial and temporal correlations. In between these two extremes we find Brownian dynamics ideas [3, 12]—incorporating thermal fluctuations into the particle equations of motions—and fluctuating hydrodynamics (cf. [63], Ch. XVII); both neglect spatial and temporal correlations of the thermal driving forces.

In fluctuating hydrodynamics stress fluctuations $\sigma'_{ij}(\vec{x})$ are built into the fluid equations and their statistical properties are found by considering ideas from nonequilibrium thermodynamics [63],

$$\langle \sigma'_{ik}(\vec{x}_1, t_1)\sigma'_{lm}(\vec{x}_2, t_2)\rangle = 2k_B T\eta\left(\delta_{il}\delta_{km} + \delta_{im}\delta_{kl}\right)\delta(\vec{x}_1 - \vec{x}_2)\delta(t_1 - t_2), \qquad (2.40)$$

where k_B is Boltzmann's constant and T the temperature. From this expression, we can find for any given discretization a finite stress vector to be included on the right hand side of the Navier-Stokes equation (2.1). We thus see that the description of fluid thermal fluctuations can quite naturally be included in our numerical framework and might be subject of a future study. It should be mentioned here that in the context of lattice-Boltzmann methods similar ideas have been used to include thermal fluctuations [24, 59, 60].

2.5.3 Scope for improving the numerical scheme

There are some unresolved numerical questions that we would like to address before we conclude.

In order to eliminate the purely numerical constants k and γ, we have tested an implicit scheme that does not require tracers, but instead associates in a quite similar fashion a force directly with each reference point. Then we make tentative fluid integration steps using these forces and compare the resulting difference velocities of fluid and template at the reference points. The forces are now modified by an additive term proportional to the velocity difference, but with the opposite direction. We thus arrive at successively "better" force distributions resulting in decreasing difference velocities. We have observed such a procedure to converge in simulations with $Re \approx 1$, but did not use it extensively due to the additional computational effort.

Due to the small slip allowed in our explicit "penalty" coupling technique there occurs a small residual fluid motion *inside* the particle regions. As a result, a certain amount of

energy is dissipated even if the coupling of fluid and tracers is not dissipative. In 3D, we find that the fraction of energy dissipated inside particle regions ranges from about 0.01 in suspensions with $\Phi = 0.05$ up to about 0.1 in for $\Phi = 0.3$. Correspondingly, one can observe changes in the sedimentation speed, which, due to these additional dissipation channels, turn out to be smaller than expected. For more precise measurements, this purely numerical dissipation must be reduced by stiffer couplings and correspondingly smaller time steps. More elaborate implicit techniques will also improve the situation, because the relative motion inside particle domains can be suppressed entirely.

2.6 Some further remarks

2.6.1 on a continuum picture,

The arguments in Sec. 2.1.2 can be made more precise if we try to understand the procedure described above as the discretized version of a continuum problem. Let us state the momentum equation of the fluid (2.1) in the form

$$\frac{D}{Dt}\rho\vec{v} = \vec{\nabla}\cdot\mathbf{T} + \vec{f}. \tag{2.41}$$

where $\mathbf{T}$ denotes the stress tensor of the fluid. Its divergence is the expression $-\vec{\nabla}p + \eta\nabla^2 v$ for Newtonian fluids used above. For the rigid particle template, we have

$$M_i^{\mathrm{t}}\dot{\vec{v}}_i = \vec{F}_i^{lp} + \vec{F}_i^{p} - (M_i - \rho V_i)g\vec{e}_z, \tag{2.42}$$

with $\vec{F}_i^{lp}$ as the force acting from the fluid on the template (determined by summation of the constraint forces), $\vec{F}_i^{p}$ the force due to the presence of other particles and the term proportional to g represents weight and buoyancy.

Let the region of fluid covered by template i at time $t = 0$ be denoted by $\Omega_i(0)$. Continuous time evolution according to Eq. (2.41) will deform this region into $\Omega_i(t)$. The positions of the tracers track this deformation and thus the maximum $\sup_j |\vec{\xi}_{ij}|$ measures the deviation of $\Omega_i(t)$ from the original particle shape. It might be intuitive to think of the marker elongations $\vec{\xi}_{ij}$ as representative discrete amplitudes of a continuous displacement field $\vec{u}_i(\vec{x})$ defined on template i, related to the position $\vec{x}_{ij}^{m}$ by $\vec{x}_{ij}^{m} = \vec{x}_{ij}^{r} + \vec{u}_i(\vec{x}_{ij}^{r})$. The constraint fluid force density $\vec{f}_i$ for particle i is related to $\vec{u}_i$ as implied by Eq. (2.16), i.e.,

$$\vec{f}_i(\vec{x}_{ij}^{m}) = -k\vec{u}_i(\vec{x}_{ij}^{r}) - 2\gamma(d/dt)\vec{u}_i(\vec{x}_{ij}^{r}), \tag{2.43}$$

where the time derivative must take the time dependence of $\vec{x}_{ij}^{r}$ into account. If the external stresses remain bounded, this form guarantees that $\vec{u}$ and the rate of change of $\vec{u}$ on

$\partial\Omega_i(t)$ remain bounded and approach zero as k and γ increase. By construction, $\Omega_i(t)$ is the union of $\vec{x} + \vec{u}_i(\vec{x})$ with $\vec{x}$ being one of the points constituting the template at time t. The incompressibility of the flow guarantees that the volume of $\Omega_i(t)$ is time invariant and equals V_i, the volume of the template.

2.6.2 conserved quantities,

The last argument shows that the sum of the mass of fluid in $\Omega_i(t)$ and the template mass M_i^t is constant and equal to the mass of the physical particle.

The total change of momentum of the coupled system is obtained by integrating (2.41) over $\Omega_i(t)$, which results in

$$\dot{\vec{P}}_i^l = \oint_{\partial\Omega_i(t)} \mathbf{T} \cdot d\vec{A} + \vec{F}_i^l, \tag{2.44}$$

where we have used Gauss's theorem to convert the integral over the divergence of the stress tensor into a surface integral. The vectors $\vec{P}_i^l$ and $\vec{F}_i^l$ denote the total fluid momentum in $\Omega_i(t)$ and the sum of the constraint forces, respectively. By construction, $\vec{F}_i^l + \vec{F}_i^{lp} = \vec{0}$. Up to a degree of accuracy determined by $\sim 1/k$ and $\sim 1/\gamma$ the center of mass velocity of the fluid in $\Omega_i(t)$ coincides with the template centers $\dot{x}_i$. Thus, for the sum of Eq. (2.44) and (2.42) we recover the equation of motion for the center of mass of a rigid particle P of mass $M_i = M_i^t + \rho V_i$ in the flow,

$$M_i \ddot{\vec{x}}_i = \oint_{\partial P} \mathbf{T} \cdot d\vec{A} - (M_i - \rho V_t) g \vec{e}_z. \tag{2.45}$$

To see what happens for the angular momentum balance, we form the vector products of Eq. (2.41) with a vector pointing from the template center of mass $\vec{x}_i$ to $\vec{x}$ before we perform the integration over $\Omega_i(t)$, i.e,

$$\int_{\Omega_i(t)} d\vec{x}\ (\vec{x} - \vec{x}_i) \times \frac{D}{Dt}\rho\vec{v} = \int_{\Omega_i(t)} d\vec{x}\ (\vec{x} - \vec{x}_i) \times \vec{\nabla} \cdot \mathbf{T} + \int_{\Omega_i(t)} d\vec{x}\ (\vec{x} - \vec{x}_i) \times \vec{f}. \tag{2.46}$$

The left hand side is the total change of angular momentum of the fluid $\dot{\vec{L}}_i^l$ and we can employ the symmetry of the stress tensor to convert the first term on the right hand side to a surface integral,

$$\dot{\vec{L}}_i^l = \oint_{\partial\Omega_i(t)} (\vec{x} - \vec{x}_i) \times d\vec{A} \cdot \mathbf{T} + \vec{\tau}_i^l. \tag{2.47}$$

As in the case of linear momentum, we also consider the corresponding equation for the template. The contribution to the torque of the gravitational forces vanishes, and

the contribution of the constraint forces cancels $\vec{\tau}_i^l$ by construction up to an accuracy determined by the maximum deviation of a tracer from a reference point. To the same accuracy, the change of angular momentum of the fluid can be written as the moment of inertia times the change of angular velocity which equals that of the template, again to the agree permitted by the tracer force law. We thus recover approximately the equation of angular motion of a rigid particle P in a fluid in the absence of external torques,

$$I_i\dot{\omega} = \oint_{\partial P} (\vec{x} - \vec{x}_i) \times d\vec{A} \cdot \mathbf{T}. \tag{2.48}$$

2.6.3 and uniqueness

The distribution of the constraint forces in the particle/template region is not uniquely determined by demanding that the fluid motion should match the rigid body motion of the particle. Also, the motion of the system as a whole does not uniquely fix $\vec{f}$. The prescription given in the text selects one of the possible distributions, but leaves some "gauge freedom" which is very similar to the indeterminacy of forces in static networks of rigid elements. Also here, the rigid template can "absorb" inner stresses consequences on the motion.

If we write the Navier-Stokes equations in the form,

$$\vec{f} - \vec{\nabla} p = \vec{G}(\vec{v}), \tag{2.49}$$

where $\vec{G}$ collects the terms depending on spatial and temporal derivatives of $\vec{v}$, then from taking curl and divergence, we find

$$\vec{\nabla} \times \vec{f} = \vec{\nabla} \times \vec{G}, \tag{2.50}$$

$$\nabla^2 p = \vec{\nabla} \cdot \vec{f} - \vec{\nabla} \cdot \vec{G}. \tag{2.51}$$

The first equation implies that the velocity distribution (and its rate of change) only determines $\vec{f}$ up to the gradient $\vec{\nabla}\phi$ of a scalar. In general, such contributions influence the pressure distribution (2.51) and thus the motion. If, however, ϕ fulfills additional conditions, i.e., $\phi = 0$ on $\partial\Omega_i$, it will not have consequences for the motion or in the exterior of Ω_i. If we extend ϕ over the whole domain such that $\vec{\nabla}\phi$ exists everywhere and $\phi = 0$ in the exterior of all Ω_i, then $p + \phi$ solves (2.51) for $\vec{f} \to \vec{f} + \vec{\nabla}\phi$. The scalar ϕ does not contribute to the momentum flux through $\partial\Omega_i$, if its surface integral $\oint_{\partial\Omega_i} d\vec{A}\ \phi$ vanishes. Likewise, the contribution to the torque, here with respect to the origin, but similarly for any reference point, is

$$\begin{aligned} \int_{\Omega_i} d\vec{x}\ \vec{x} \times (\vec{\nabla}\phi) &= \int_{\Omega_i} d\vec{x}\phi\vec{\nabla} \times \vec{x} - \int_{\Omega_i} d\vec{x}\vec{\nabla} \times (\vec{x}\phi) \\ &= -\oint_{\partial\Omega_i} d\vec{A} \times (\vec{x}\phi) \end{aligned} \tag{2.52}$$

and vanishes if the surface integral vanishes. This is the case in particular, if $\phi = 0$ on $\partial\Omega_i$ as advertised above.

Since the $\vec{f}$ acting on the fluid has a reaction force of opposite sign on the particle template, these conditions guarantee also vanishing force and torque contributions on the template as a whole.

Chapter 3

Monodisperse Sedimentation

3.1 Velocity fluctuations

The average velocity of sedimenting non-Brownian suspensions can be predicted theoretically [7, 13]. In contrast the understanding of the fluctuations of the particle velocities is not yet satisfactory. While theories [17, 42, 100] predict that the velocity fluctuations in random suspensions should diverge as the size L of the container is increased, experiments find either no dependency on the size of the container [75] or that the velocity fluctuations saturate if the container size is increased over a threshold [93]. In contrast to the experimental results, simulations [62] which used periodic boundary conditions found the predicted divergence of the velocity fluctuations with the system size.

3.1.1 Estimate of the velocity fluctuations

We will now calculate the magnitude of the velocity fluctuations using some scaling arguments of Hinch [43] and the experimental results of Segrè et al. [93].

If we imagine the system of size $2L \times L \times L$ to be separated into 2 halves by an imaginary wall, then we cannot expect both parts of the system to contain the same number $N = 3/(4\pi)\phi(L/a)^3$ of particles. We expect a difference of order $\sqrt{N}$ as would be the case if the particle distributions were random and independent. The difference in weight will then lead to a relative motion of these two regions. More precisely, $\sqrt{N}$ particles will give rise to a excess force of

$$F_1 = \pm\sqrt{N}\ \frac{4}{3}\pi a^3 \Delta\rho g. \tag{3.1}$$

This will cause the velocities of two neighboring regions to differ until the driving force is balanced by the shear force. The shear force can be estimated by the expected velocity

gradient $\Delta U/L$, the viscosity and the area $\sim L^2$ of the separated areas.

$$F_2 = \eta \frac{\sigma}{L} L^2, \tag{3.2}$$

Here σ is the velocity difference between the different regions. In the stationary state of a suspension, the two forces balance each other and we thus obtain the magnitude of the velocity fluctuations,

$$\sigma = \frac{4}{3}\pi \frac{\sqrt{\frac{\phi L^3}{a^3}} a^3 \Delta\rho g}{\eta L} \sim U_{\mathrm{St}} \sqrt{\frac{\phi L}{a}}, \tag{3.3}$$

where U_{St} is the Stokes velocity of a single particle.

If there is a length scale ξ on which the suspension is homogeneous due to correlations between the particles, then our previous argumentation is valid only for $L < \xi$. For system sizes $L > \xi$ the size of the correlated regions replaces the role of the system size in our previous arguments. Segrè et al. [93] have measured the correlations in suspensions and found

$$\xi_{||} = 11 a \phi^{-1/3}. \tag{3.4}$$

If we use this ξ to estimate L, we find that

$$\sigma = \sqrt{11} V_{\mathrm{St}} \phi^{1/3} \approx 3 V_{\mathrm{St}} \phi^{1/3}. \tag{3.5}$$

With this argument we expect that the velocity fluctuations scale in large systems as

$$\sigma \sim V_{\mathrm{St}} \phi^{1/3}. \tag{3.6}$$

This is consistent with experimental findings as shown in Fig. 3.1 (Figure 3 of [93]) where the velocity fluctuations are measured in large systems of width $W \geq 100 a \phi^{-1/3}$.

As explained above, the velocity fluctuations can be expected to be independent of the system size only if the size of the system is significantly larger than the correlation length. If, in contrast, the container width is of the same magnitude as the correlations length, the width of the container will control the absolute value of the velocity fluctuations. Eq. (3.3) indicates that the velocity fluctuations in case of small containers should scale with the square root of the container size.

With regard to the volume fraction dependency we expect that the fluctuations scale as $\phi^{1/2}$ for small systems and $\phi^{1/3}$ for large systems.

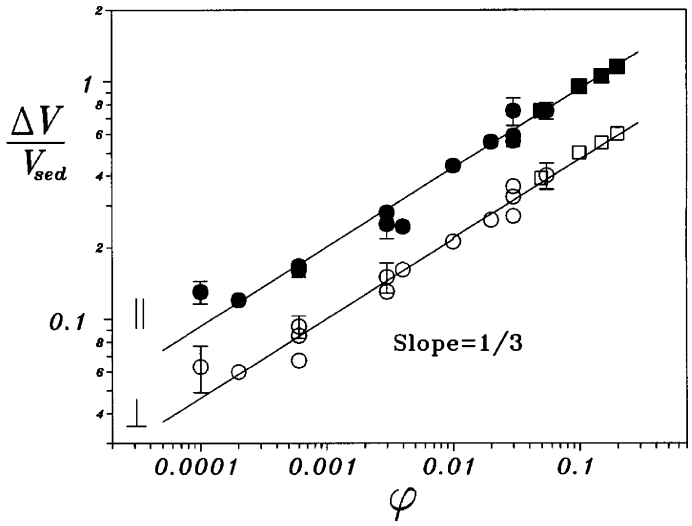

Figure 3.1: Figure 3 of [93]: Experimental measurements of the normalized velocity fluctuations $\Delta V/V_{\mathrm{St}}$. The data shown are from Segrè (circles) and Nicolai [75] (squares).

3.1.2 Systems with periodic boundary conditions

In order to reduce wall effects in the simulations we use periodic boundary conditions in all directions. We measure the velocity fluctuations in various systems of different sizes and different volume fractions. The simulation details are given in Table 3.1.

Width	Height	ϕ	T_{final}	$< U_{\|\|} >$	$\sigma_{\|\|}$
24	24	0.02	200	0.76968	0.300879
48	48	0.02	200	0.83065	0.44554
128	128	0.02	232	0.858481	0.707185
32	64	0.1	200	0.519128	0.556742
64	128	0.1	121	0.539484	0.765868
128	256	0.1	150	0.551416	1.21439
22	22	0.1	200	0.463158	0.302273
24	48	0.1	200	0.513729	0.440247
64	128	0.3	200	0.134829	0.348823

Table 3.1: Simulations of monodisperse suspensions in a container with a square ground section. The sampling started at $T = 50$ and ended at $T = T_{\mathrm{final}}$ shown in the table.

If the size of our simulations is below the limit where the velocity fluctuations become independent on the size of the system we expect

$$(\sigma/U_{\mathrm{St}}) \sim (L\phi)^{1/2}. \tag{3.7}$$

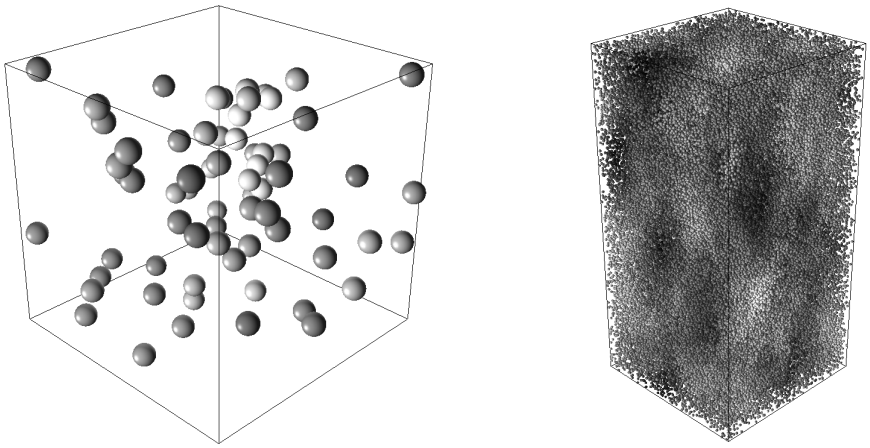

(a) (b)

Figure 3.2: Snapshots of typical systems used to calculate the velocity fluctuations in systems with periodic boundary conditions. (a) shows a system of size $24 \times 24 \times 24$ at a volume fraction of $\phi = 0.02$ (68 particles) and (b) a system of size $128 \times 256 \times 128$ at a volume fraction of $\phi = 0.1$ (100,132 particles) .

Consequently, a plot of the relative velocity fluctuations versus $(L\phi)^{1/2}$ should show all the data points on a straight line. We show the results in Table 3.1 and in Figure 3.3(a). We fit the measured velocity fluctuations to a line $f(x) = bx + c$ with $b = 0.63$ and $c = -0.12$, which is also shown in Figure 3.3(a). However, due to the dependence of σ on the product of $L^{1/2}$ and $\phi^{1/2}$ a small change of one of the exponents does not lead to a completely different rescaling. This is seen in Figure 3.3(b) where we use $\phi^{1/3}$ to scale the data. Though the fit is better in (a), a $\phi^{1/3}$ dependence cannot be entirely excluded.

3.1.3 Systems with walls

In the previous section we used periodic boundary conditions to minimize the effects of walls in the simulations. This approach is good for general studies of system size effects and bulk properties. But as soon as we want to compare the results of the simulations with experiments of a certain geometry this approach is problematic, because it is not clear how the presence of walls influences the suspension. If we are able to simulate a system of the same size as used in the experiment we use solid walls in all directions perpendicular to gravity to match the conditions of the experiments as close as possible and thus avoid effects from the absence of the walls.

In 1995 Nicolai and Guazzelli [76] published the results of experiments on the *Effect of the vessel size on the hydrodynamic diffusion of sedimenting spheres*. They used glass beads with a radius of $a = 0.394$mm in a viscous fluid (13 P) and a settling container

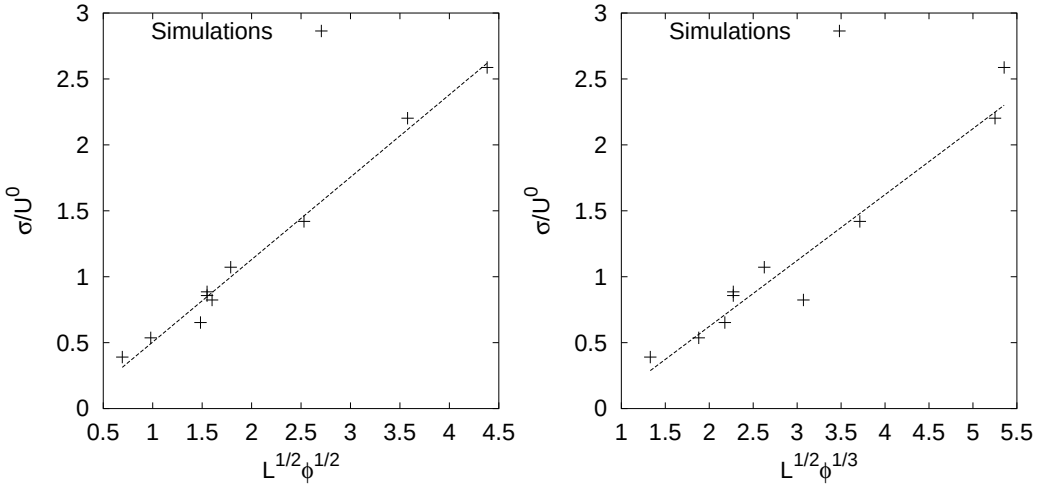

(a) (b)

Figure 3.3: Velocity fluctuations of the simulations listed in Table 3.1 versus (a) $L^{1/2}\phi^{1/2}$ as predicted by Eq. (3.3) and (b) $L^{1/2}\phi^{1/3}$. Scatter of the data in (a) is less than that in (b) so that we conclude that the scaling with $L^{1/2}\phi^{1/2}$ seems to be correct.

of height $L_y = 1262a$ and width $L_x = 252a$ and varied the depth of the vessel between $L_z = 50a$ and $200a$ (cf. Figure 3.4).

They tracked the the trajectories of marked particles in a suspension of unmarked particles with a digital imaging system and calculated the local velocities of the particles in the x and y directions and the corresponding velocity fluctuations. The particles were tracked in a imaging window of approximately 150 by $300a$. The depth of the imaging extended through the whole system.

With this experimental setup they found velocity fluctuations $\sigma_x \approx 0.33 \pm 0.04$ and $\sigma_y \approx 0.66 \pm 0.08$. The velocity fluctuations do not depend on the depth of the vessel, and the ratio $\sigma_y/\sigma_x \approx 2$.

The measurements of Nicolai and Guazzelli neglected the movement of the particles in z direction, thus it was not possible to measure the velocities and their fluctuations in in the z direction. It is therefore not clear if there is an influence of the vessel size in the z direction on the fluctuations of the velocities' z component. Our simulations are chosen to match the setup of Nicolai and Guazzelli as closely as possible. Nevertheless there are two major differences, namely, the boundary condition in the y direction and the Reynolds number. The height of the vessel in Nicolai's experiments was $1262a$ which we cannot achieve in our numerical simulations. We therefore choose to use periodic boundary conditions in the y direction and a vessel size of $L_y = 250a$. The second difference, the Reynolds number, was less than 10^{-3} in the experiment, whereas we use a

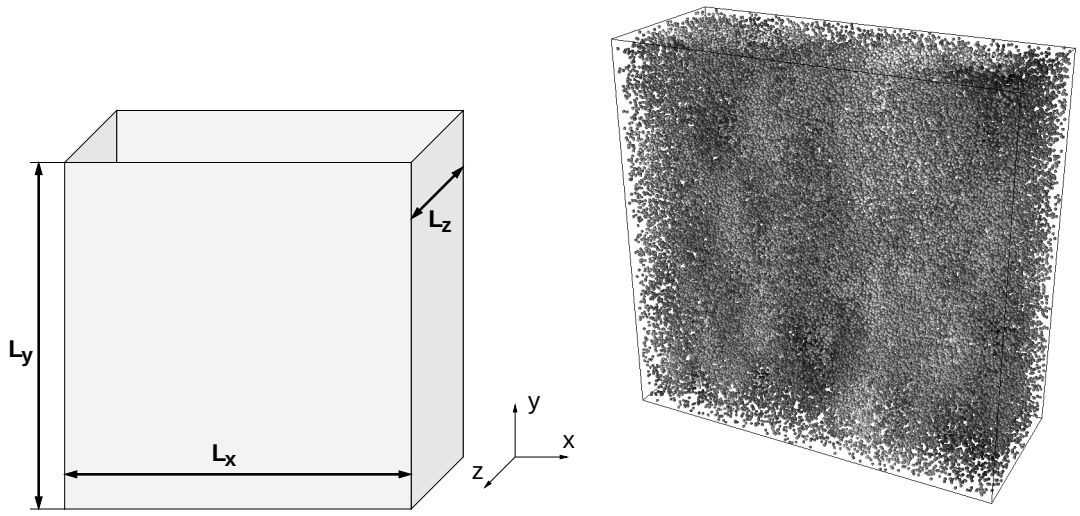

(a) (b)

Figure 3.4: (a) simulation setup and coordinate system used in the simulations. Gravity points in $-y$ direction. The boundary conditions in the simulations are periodic parallel to gravity and rigid wall perpendicular to it. (b) snapshot of a typical system of size $250 \times 250 \times 100$ with 74719 particles.

Reynolds number of 0.1 in our simulations. The setup of the simulations is summarized in Table 3.2.

a	=	1	L_x	=	250
ρ	=	2.5	L_y	=	250
g	=	30	L_z	=	$25 \ldots 200$
ϕ	=	0.05	h	=	0.78
ν	=	10			

Table 3.2: Parameters used in the simulations of the experiments of Nicolai and Guazzelli.

We sample the particle positions and velocities in a area of size $150 \times 250 \times 10$ in the center of the simulated vessel. This ensures that we do not sample particles which are strongly influenced by the walls. We first study the time dependency of the velocity fluctuations in the suspension to learn when the velocity fluctuations reach a steady state and how they change with time. We therefore measured the velocity fluctuations in intervals of $1t_{\mathrm{St}}$ and average over 10 measurements. The results for σ_y are shown in Figure 3.5 and for σ_x and σ_z in Figure 3.6 .

The magnitude of the velocity fluctuations in our simulations is about 40% larger than in the experiments of Nicolai and Guazzelli. One reason for this large value is that we only sampled particles located in the sampling zone of size $150 \times 250 \times 20$ in the center of

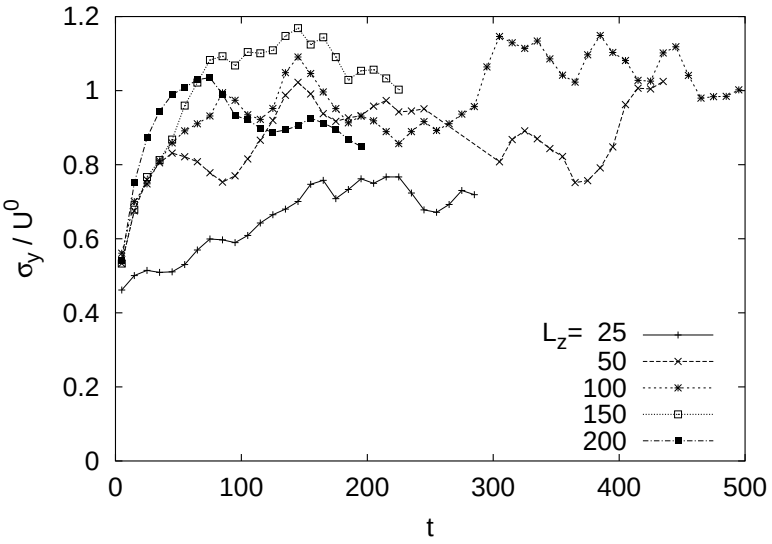

Figure 3.5: Time dependency of the velocity fluctuations in y-direction for different depth L_z of the vessel. The final value of the velocity fluctuations is independent of the depth L_z for vessels with depth larger than $50a$.

the system. Therefore, we do not sample particles that are close to the walls. Particles close to the walls will show smaller velocity fluctuations. This explains that the velocity fluctuations decrease from 0.91 to 0.82 when we extend the sampling region in the z direction to span the whole system.

The second explanation is that a relatively coarse grid ($h = 0.73$) has been used to discretize the fluid. If the grid size of the fluid h is halved, the relative fluctuations decrease from 0.91 to 0.87 for the system with $L_z = 50$. Thus part of the fluctuations is due to numerical inaccuracies. As the computational effort scales with h^5 we are presently not able to calculate all the systems with higher accuracy. Nevertheless, the ratio of σ_y/σ_x in all our simulations is 2, the same value as measured in the experiment.

The fluctuations for the different components increase very rapidly. They become stationary after approximately 150 t_{St}. But even as the stationary state is reached, the fluctuations vary strongly on time scales of about $100 \cdots 200 t_{\mathrm{St}}$ which corresponds to the time scale on which the large scale structures (swirls) in the suspension change. We find in accordance with Nicolai and Guazzelli that σ_x and σ_y do not change within the error bars if the depth of the vessel is varied between 50 and $200a$. But we find a reduction of σ_z for $L_z = 50$, which has not been measured by Nicolai and Guazzelli. In contrast to the experiments of Nicolai, we also simulated a system with a vessel of depth $L_z = 25$ and find a significant reduction in all components of σ, especially in the z component.

There are two possible explanations of the findings of the experiments and the simula-

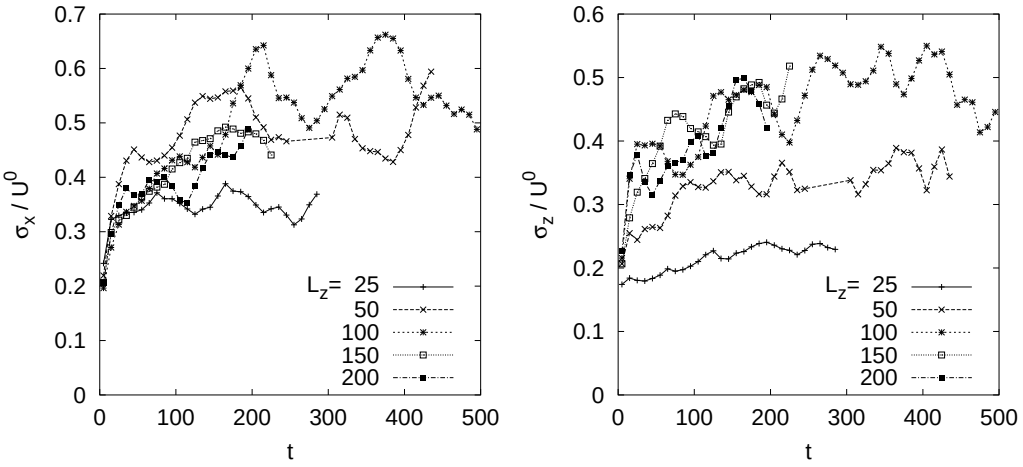

(a) (b)

Figure 3.6: Time dependency of the velocity fluctuations of the x-component (a) and z-component (b) for different depths L_z of the vessel. Like the fluctuations of the y component of the velocities, the final value of the velocity fluctuations is independent of the depth L_z for vessels with depth larger than $50a$. For $L_z < 50$ all components of σ show a decrease of the velocity fluctuations.

tions:

1. The velocity fluctuations are dominated by the largest dimension of the vessel if its smallest dimension exceeds a critical value. We expect that this critical length should be of order of the spatial correlations of the velocities. If the smallest dimension of the vessel is smaller than the critical size the velocity fluctuations will be limited by the size of the smaller dimension.

2. The velocity fluctuations are always dominated by the smallest dimension of the vessel. If the smallest dimension of the vessel exceeds a critical size then the velocity fluctutations saturate and reach a final value independend of this size.

Both arguments would explain the results we have presented up to now. We try to find the correct one by simulating a system where the smallest dimension of the vessel is above the supposed critical length, and the larger dimension is decreased. We simulate a system of size $150 \times 250 \times 100$ and compare the velocity fluctuations with the fluctuations in a system of size $250 \times 250 \times 100$.

In Figure 3.7 we compare the velocity fluctuations of the simulations with $L_x = 250$ and $L_x = 150$. No component of the velocity fluctuations changes significantly when the larger dimension of the vessel is reduced. This suggests that the smallest dimension controls the magnitude of the velocity fluctuations and that assumption 2. is correct.

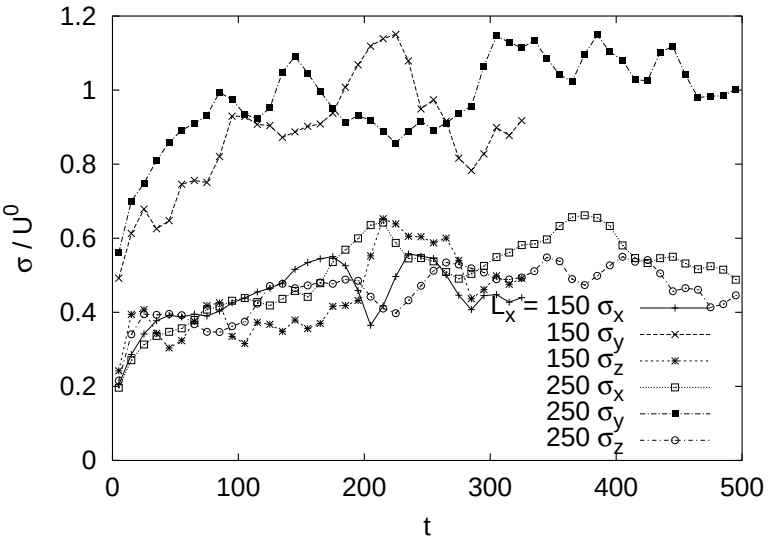

Figure 3.7: Time dependency of the velocity fluctuations when the larger extension L_x is changed from $L_x = 250$ to 150 and $L_z = 100$ is constant. The velocity fluctutations do not change due to a decrease of the larger extension, which indicates that the smaller dimension dominates the magnitude of the velocity fluctuations.

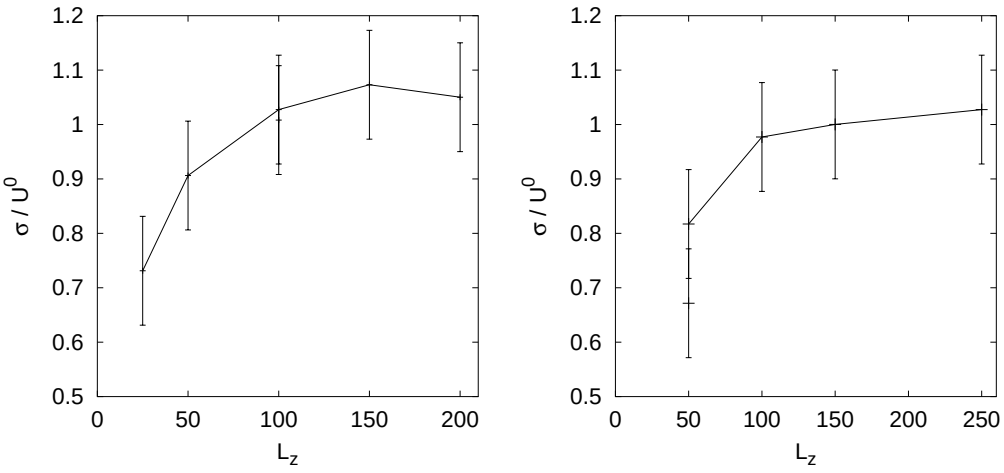

Figure 3.8: Velocity fluctuations σ_y as a function of the system size. The left side (a) shows the σ_y as a function of L_z for $L_x = 250$. On the right side L_x is varied and $L_z = 100$. The fluctuations increase until the smallest dimension of the vessel reaches a size of $\approx 100a$.

We show the velocity fluctuations as a function of the depth of the vessel in Figure 3.8(a). Figure 3.8(b) shows the velocity fluctuations for a depth of $100a$ and various widths of the system. The sampling started at $t = 150t_{\mathrm{St}}$ and we sampled all particles inside a sampling region of size $150 \times 250 \times 20$ located in the center of the vessel. We find that the fluctuations increase for vessels with the smallest extension below $100a$. As soon as the smallest extension increases above $100a$ the fluctuations are constant.

This is consistent with the spatial distribution of the velocity fluctuations, which we show in Figure 3.9 for σ_y and in Figure 3.10 for σ_x. To obtain the data shown, we divide the system in $N_x \times N_z$ columns and sample the particle velocity of all particles inside each column. All particles are sampled starting at $t = 100t_{\mathrm{St}}$. To improve the statistics we utilize the symmetry of the system in the x and z direction.

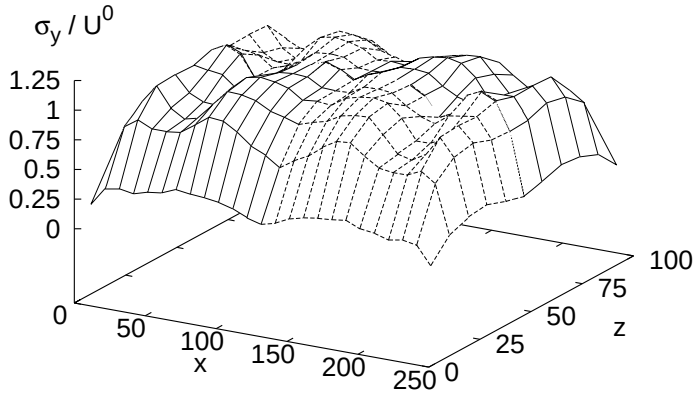

Figure 3.9: Spatial distribution of the velocity fluctuations σ_y for the vessel of size $250 \times 250 \times 100$ averaged over the height of the vessel.

Figure 3.9 and 3.10 show that the velocity fluctuations increase quickly and saturate to a final value. The larger fluctuations of σ_y in Figure 3.9 are due to the fact that only one simulation has been evaluated, so that long-lasting swirls are not well averaged. We find that the distance from the wall up to which the fluctuations are affected by the wall is approximately the same for the of the velocity components in the direction normal to the wall as for the directions parallel to the wall (cf. Figure 3.10).

In Figure 3.11 we show the velocity fluctuations as a function of the depth of the system. We find that σ_x and σ_z are reduced by the walls up to a distance of $\approx 50a$ from the wall. For distances $> 50a$ the velocity fluctuations are approximately constant. The distance of $50a$ is in accordance with our previous observations that the velocity fluctuations become independent of the system size when the size exceeds $100a$.

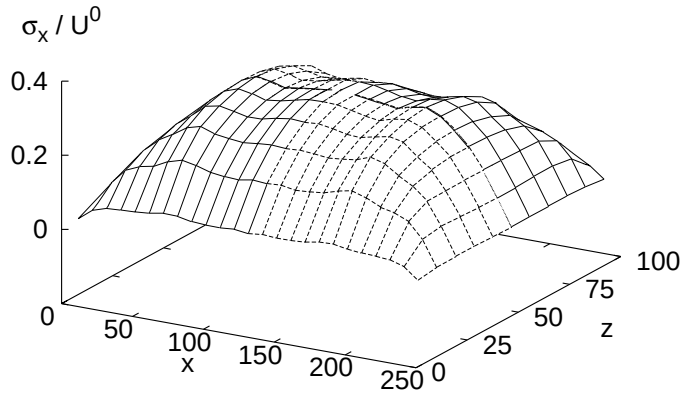

Figure 3.10: Spatial distribution of the velocity fluctuations σ_x for a vessel of size $250 \times 250 \times 100$.

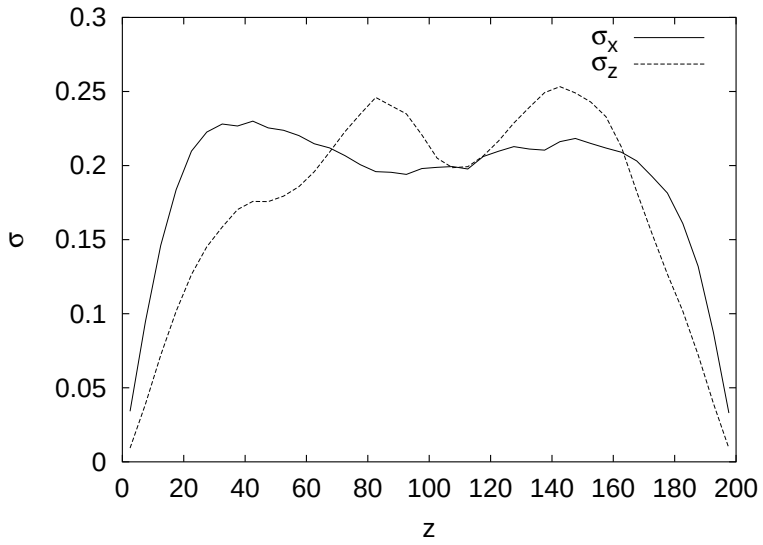

Figure 3.11: Velocity fluctuations as a function of z for a system of size $250 \times 250 \times 200$.

We previously suggested that the critical depth of the container should be of the same order of magnitude as the spatial correlations of the velocities in the direction perpendicular to gravity. To confirm this suggestion we measured the spatial correlation of the particle velocities. The spatial correlation of U_i is defined as

$$C_{U_i}(\vec{r}) = \frac{\langle U_i(0)U_i(\vec{r})\rangle - \langle U_i(0)\rangle\langle U_i(\vec{r})\rangle}{\sigma_{U_i(0)}\sigma_{U_i(\vec{r})}}, \tag{3.8}$$

where $\vec{r} = \vec{x}_2 - \vec{x}_1$ is the distance vector of the particles. We measured the spatial correlations as a function of $r = |\vec{r}|$ and the angle θ between $\vec{r}$ and the y coordinate axis $\vec{y}$. In the experiments of Segrè [93] the projection of the particle velocities on a plane have been used to calculate the spatial correlations of the velocities. To make our measurements comparable with the experimental results, we calculate the spatial correlations twice, once for particle pairs with $\vec{r}$ lying in the yx-plane and also for pairs with $\vec{r}$ lying in the yz-plane. To reduce the effect of the walls we sample particle pairs only if both particles are located inside the measurement volume, which is located in the center of the vessel and of size $150 \times 250 \times 20$ for the system of size $250 \times 250 \times 100$.

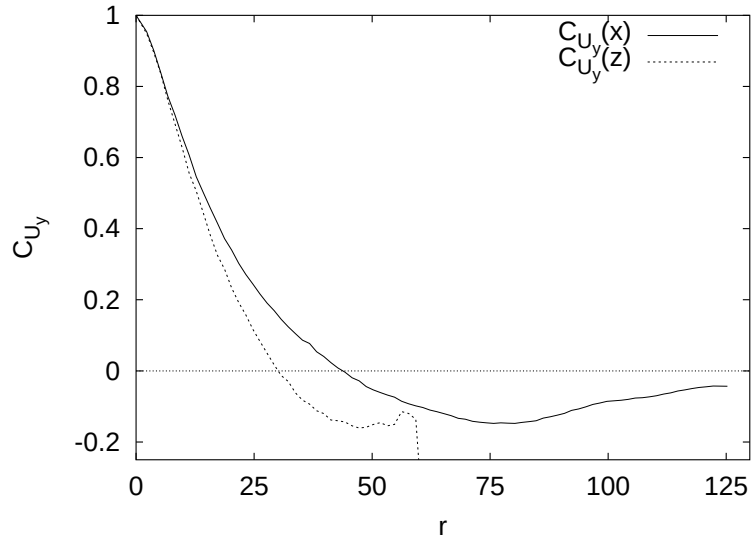

Figure 3.12: Spatial correlations of the settling velocities U_y measured in the x direction (solid line) and the z direction (dotted line). The depth L_z of the vessel was $100a$ and the width $L_x = 250a$.

Figure 3.12 shows the correlation of the velocity compononent in y direction as a function of the distance r in the x and z directions. The system size was 250×100 in the x and z directions. Thus only distances up to $60a$ in the z direction could be measured without using particles in the vicinity of a wall. The correlation functions decrease rapidly and the distinct negative correlation in x-direction shows the presence of a structure of characteristic size in the suspension. The faster decrease of the correlation in the z-direction

shows that the correlation length of the y-component of the velocity is reduced.

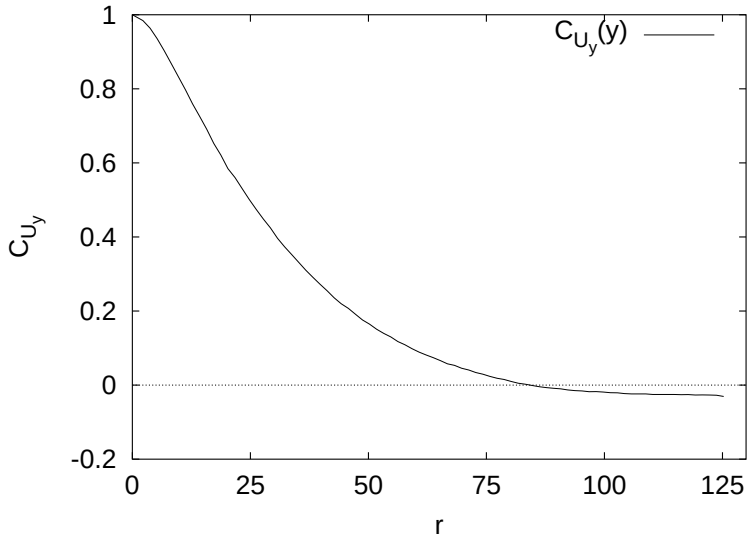

Figure 3.13: Spatial correlations of the settling velocities U_y measured in the direction parallel to gravity in a vessel with depth $L_z = 100a$. For large separations the correlations tend to zero.

Figure 3.13 shows the correlations of the velocities in the vertical direction. In the y direction the velocity corelation shows a less pronounced negative correlation when compared to the correlations in the horizontal directions.

Segrè et al. [93] measured the spatial correlations of the velocities and found that the particle distance with the minimum horizontal correlation can be well characterized by

$$\xi_\perp = 27a\phi^{-1/3}. \tag{3.9}$$

This leads to a correlation length of $\xi_\perp = 73a$ for $\phi = 0.05$. We find a correlation length of $\approx 75a$. In Figure 3.14 we show the measured spatial correlation of Segrè together with our data. We use the same scaling as proposed by Segrè: $x/a\phi^{-1/3}$. We find that the correlations are quite similar.

We have seen previously that the velocity fluctuations decrease significantly if the system depth is reduced below $50a$, so that the question arises as to how the spatial velocity correlations in the x direction are affected when the system size is decreased in the z direction. In Figure 3.15 we compare the spatial velocity correlations for a system where $L_z = 100$ with a system where $L_z = 25$.

It is clearly visible that a reduction of the depth of the system in the z-direction causes a reduction of the correlation length in the x-direction. This indicates that all the extensions

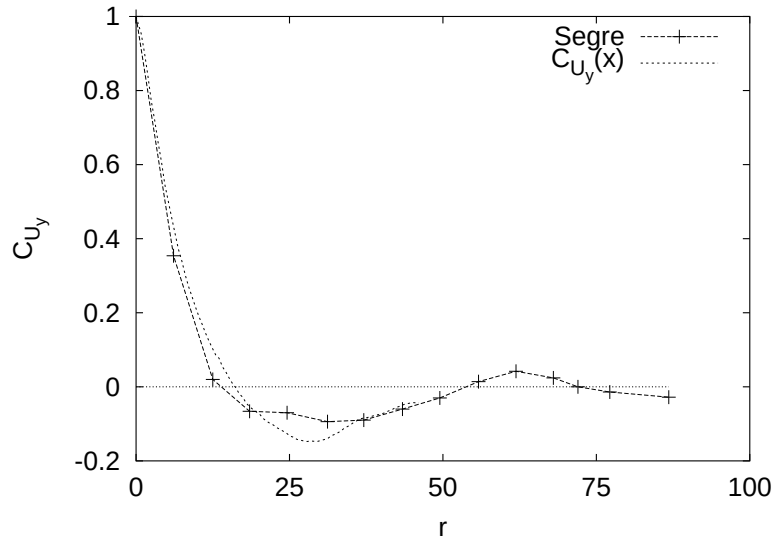

Figure 3.14: Spatial correlations of the settling velocities U_y measured in the x direction in a vessel with depth $L_z = 100a$ and the data of Segrè t al. [93] (+) of a suspension with $\phi = 0.03$.

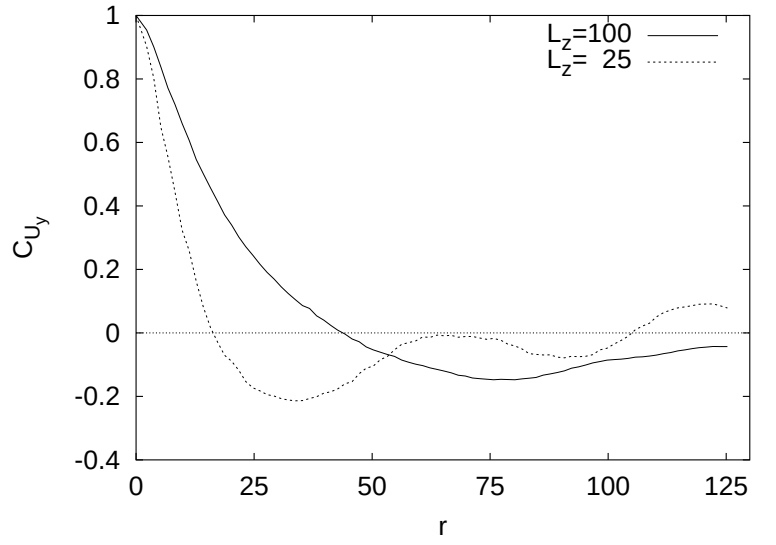

Figure 3.15: Spatial corelations of U_y measured in the x direction for vessel depth L_z of 25 and $100a$. Not only the velocity fluctuations change with the vessel depth but also the correlation length.

of a vessel have to be taken into account when the sizedependency of velocity fluctuaions are studied.

In Figure 3.16 we show the velocities relative to the average particle velocity. We only show the velocities of particles located in a slice of $10a$ located at the center of the container. The container had periodic boundary conditions in the direction of gravity and walls in the other directions. The depth of the system was (a) $25a$, (b) $50a$,(c) $100a$, and (d) $200a$. It can be seen that the instantanious fluctuations of the velocities increase significantly as the system depth is increased from $25a$ to $50a$.

By drawing the relative velocities (Fig.3.16) we also *see* the meassured size of the correlation length, which is approximately $1/4$ of the system width for the large depths and approximately $1/8$ of the system width for the container with depth $25a$.

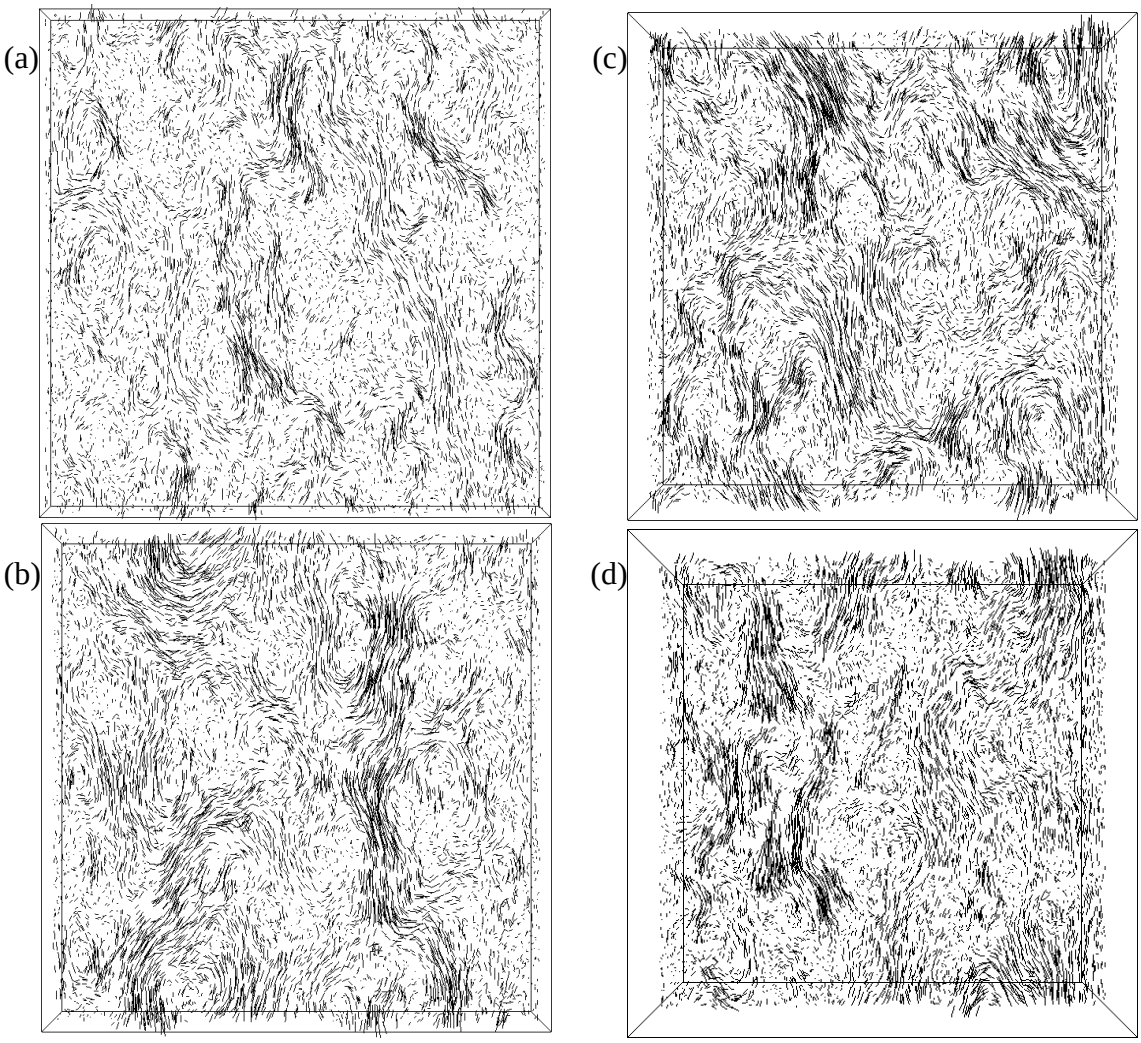

Figure 3.16: Particle velocities relative to the average particle velocity of particles located in the center of a vessel with depth (a) $25a$,(b) $50a$,(c) $100a$, and (d) $200a$. The velocity fluctuaions in (b,c,d) are significantely larger than in (a). Also the spatial extension of the *swirls* are larger when the system depth is increased over $25a$.

Chapter 4

Bidisperse Sedimentation

This chapter is dedicated to the study of the simplest cases of polydisperse suspensions of spheres. We consider a bidisperse suspension of particles with different sizes (section 4.2.1) or different densities (section 4.2.2).

In addition to the volume fractions ϕ_l and ϕ_s, we require two other dimensionless parameters to fully characterize the suspension, the particle radii ratio $\lambda = a_l/a_s$ and the reduced density ratio $\gamma = \Delta\rho_l/\Delta\rho_s$, where $\Delta\rho_i = \rho_i - \rho$ denotes the density difference of particle species i and the fluid.

The most important parameter remains the total volume fraction $\phi_t = \phi_l + \phi_s$. The influence of λ and γ is more complex to understand and generally less important if the values do not differ significantly from unity. This is reflected in the history of models that have been proposed for the particles' velocities. Only a few take the influence of species volume fraction, radii ratio and density ratio into account. The following types of models have been proposed to describe multi-species suspensions:

- So called cell models where particles settle independently of each other in a cell. The size of the cells is given by the particle volume fractions and the radii ratio [38, 94, 95]. The influence of density ratios is considered only in the single particle settling velocities.
- Phenomenologically motivated polydisperse extensions of monodisperse equations as, e.q. Lockett et al. [65, 66] or Mirza and Richardson [74]. These models take into account only the influence of volume fractions on the settling velocities. The particle radii and densities enter only indirectly via the single particle settling velocity.
- Analytical studies from first principles, which calculate the mean settling velocities for particles by solving the Stokes equations. Here, the analyses of Batchelor [6]

and Batchelor and Wen [8] are the most comprehensive. The relative velocity of particle pairs is calculated and used to determine the suspension structure, which then is employed to calculate the average settling velocities of the suspension.

4.1 Theory

We will briefly summarize Batchelor's theory [6, 8] because the discussion in the next sections will rely on his basic arguments.

Batchelor considers particles in a Newtonian fluid of viscosity η where all effects of inertia can be neglected [4, 6]. Thus, the Stokes equation

$$\eta \nabla^2 \vec{u} = \nabla p, \quad \nabla \vec{u} = 0 \tag{4.1}$$

is used to describe the fluid. A single particle settles with the Stokes velocity

$$\vec{U}_{\mathrm{S}t} = \frac{2a^2 \Delta\rho g}{9\eta}, \tag{4.2}$$

where $\Delta\rho$ is the density difference of the particle and the fluid.

We consider a suspension of N different particle species where each species i can be characterized by the particles radius a_i, the particle density ρ_i and the particle volume fraction ϕ_i. The particles are randomly distributed in space with equal probability such that there is no overlap between spheres. The particles are represented by point forces and a particle with velocity U_0 at distance R changes the fluid velocity $\sim aU_0/R$. The leading order of the correction to the mean settling velocity due to the volume fraction depends on how the particles are arranged. In the case of a regular geometrical arrangement of the spheres, we find that a/R is proportional to $\phi^{1/3}$ which leads to a correction of the settling velocities that is of order $\phi^{1/3}U_0$. This is in contrast to a random distribution of spheres where all accessible distances are *sampled*. Here the integral over the accessible positions minus the integral over the inaccessible positions scales with order ϕ.

The settling velocity for each species is of the form

$$\langle \vec{U}_i \rangle = \vec{U}_i^{(0)} (1 + \sum_{j=1}^{N} S_{ij}\, \phi_j). \tag{4.3}$$

which is correct to order $\phi = \sum_i \phi_i$. Here $\vec{U}_i^{(0)}$ is the Stokes velocity $\vec{U}_{\mathrm{S}t}$ of particle species i. The sedimentation coefficients S_{ij} depend on the particle radii ratio

$$\lambda = \frac{a_j}{a_i} \tag{4.4}$$

and the reduced density ratio

$$\gamma = \frac{\rho_j - \rho}{\rho_i - \rho}. \tag{4.5}$$

The sedimentation coefficient is calculated by computing the interaction of pairs of particles of different densities and radii. We consider a sphere of species 1 located at $\vec{x}_1$ and a sphere of species 2 at $\vec{x}_2$. A force $\vec{F}_1$ or $\vec{F}_2$ respectively acts on each sphere. The linearity of the underlying equations implies that the resulting velocity of sphere i can be calculated by

$$\vec{U}_i = \mathbf{b}_{ii}\vec{F}_i + \mathbf{b}_{ij}\vec{F}_j \tag{4.6}$$

where $\mathbf{b}_{ij}$ is the mobility tensor which is written as

$$\mathbf{b}_{ij} = \frac{1}{3\pi\eta(a_i + a_j)} \left(A_{ij}\frac{\vec{r}\vec{r}}{|\vec{r}|^2} + B_{ij}(\mathbf{I} - \frac{\vec{r}\vec{r}}{|\vec{r}|^2}) \right) \tag{4.7}$$

where we have introduced $\vec{r} = \vec{x}_2 - \vec{x}_1$, the unit tensor $\mathbf{I}$ and the dimensionless two-sphere mobility functions A_{ij} and B_{ij}. These functions have been calculated (e.g., by Jeffrey [50]) and depend on the size ratio λ and the interparticle distance $|\vec{r}| = r$. They are obtained for $r \gg (a_1 + a_2)/2$ by the *method of reflections*. If we use $\vec{F}_i = 6\pi\eta a_i \vec{U}_i^{(0)}$ for the forces, then the relative velocities $\vec{V}_{ij}$ of the two spheres can be calculated as a function of the relative positions $\vec{r}$.

$$\vec{V}_{ij}(\vec{r}) = (\lambda^2\gamma - 1)\vec{U}_i^{(0)} \left(\frac{\vec{r}\vec{r}}{r^2} L(s) + (\mathbf{I} - \frac{\vec{r}\vec{r}}{r^2}) M(s) \right) \tag{4.8}$$

where we introduced the normalized interparticle distance $s = 2r/(a_1 + a_2)$ and

$$\begin{aligned} L(s) &= \frac{\lambda^2\gamma A_{22} - A_{11}}{\lambda^2\gamma - 1} + \frac{2(1 - \lambda^3\gamma)A_{12}}{(1+\lambda)(\lambda^2\gamma - 1)}, \\ M(s) &= \frac{\lambda^2\gamma B_{22} - B_{11}}{\lambda^2\gamma - 1} + \frac{2(1 - \lambda^3\gamma)B_{12}}{(1+\lambda)(\lambda^2\gamma - 1)}. \end{aligned} \tag{4.9}$$

To calculate the mean velocities in the suspension we integrate the additional velocity of particle i caused by the other particles over the whole volume. The integral has to be weighted by the pair-distribution function g_{ij} to render the correct result. Now the problem arises that this integral diverges with $r \to \infty$ due to the terms of order r^{-1} and r^{-3} in the mobility functions A_{ij} and B_{ij}. This problem has been solved by Batchelor for the mean velocity in a monodisperse suspension [4] and for polydisperse suspensions [5]. If we do not allow for interparticle forces, then the mean additional velocity can be written as

$$\langle \Delta\vec{U}_i \rangle = \vec{U}_i^{(0)} \sum_{j=1}^{N} \phi_i \left\{ \left(\frac{1+\lambda}{2\lambda} \right)^3 (\mathbf{J}' + \gamma\lambda^2\mathbf{J}'') - \gamma(\lambda^2 + 3\lambda + 1)\mathbf{I} \right\} \tag{4.10}$$

where

$$\mathbf{J}' = \frac{3}{4\pi}\int_{s\geq 2}\left\{A_{11}\frac{\vec{s}\vec{s}}{s^2} + B_{11}\left(\mathbf{I} - \frac{\vec{s}\vec{s}}{s^2}\right) - \mathbf{I}\right\} g_{ij}(\vec{s})d\vec{s}, \tag{4.11}$$

and

$$\begin{aligned}\mathbf{J}'' = \frac{3}{4\pi}\frac{2\lambda}{1+\lambda}\int_{s\geq 2}\Bigg[&\left\{A_{12}\frac{\vec{s}\vec{s}}{s^2} + B_{12}\left(\mathbf{I} - \frac{\vec{s}\vec{s}}{s^2}\right)\right\} g_{ij}(\vec{s}) \\ &- \left\{\frac{3}{4s}\left(\mathbf{I} + \frac{\vec{s}\vec{s}}{s^2}\right) + \frac{1+\lambda^2}{(1+\lambda)^2 s^3}\left(\mathbf{I} - \frac{3\vec{s}\vec{s}}{s^2}\right)\right\}\Bigg] d\vec{s}.\end{aligned} \tag{4.12}$$

In contrast to the case of a monodisperse suspension, where Batchelor assumed that the particles in the suspension are randomly distributed, the pair distribution function in a polydisperse suspension is not known a priori. The relative motion of two spheres in a polydisperse suspension will cause a non uniform pair distribution function.

If we neglect interparticle forces and restrict our attention to the case of non-Brownian particles (e.g. large Peclèt number), then we do not need to take diffusion into account and the differential equation for the pair distribution function is the continuity equation for g_{ij} (as a pair density) and the convective pair density flux $\vec{V}_{ij}g_{ij}$

$$\frac{\partial g_{ij}}{\partial t} + \vec{\nabla}\cdot(\vec{V}_{ij}g_{ij}) = 0. \tag{4.13}$$

This equation can be solved [7] if the trajectories of the particle pair are infinite, e.g. the particle distance r tends to ∞ for $t \to \infty$. Batchelor finds that

$$\ln g_{ij}(\vec{s}) = \int_s^\infty \left(\frac{2(L-M)}{sL} + \frac{1}{L}\frac{\mathrm{d}L}{\mathrm{d}s}\right)\mathrm{d}s. \tag{4.14}$$

One may find asymptotic forms for g_{ij} from Eq. (4.14) in the limits of $s \gg 1$ and $(s-2) \ll 1$ but in general g_{ij} has to be determined numerically.

It is interesting to note that in the limit of a suspension of identical spheres, e.g. $\lambda \to 1$ and $\gamma \to 1$, the values of $L(r)$ and $M(r)$ depend on the order in which the limits are taken. Therefore a suspension of equally dense particles with a slight dispersion will show a g_{ij} different from that of a suspension with particles of the same size but a slight variation of densities. Batchelor also argues that in case of almost identical particles the Peclèt number could be of size unity since the *relative* velocity is small. Thus Brownian motion will resolve the indeterminacy in the case discussed here.

From the pair distribution it is now possible to calculate the sedimentation coefficients

$$\begin{aligned}S_{ij}(\lambda,\gamma) \;=\; &\int_2^\infty \Bigg[\left(\frac{1+\lambda}{2\lambda}\right)^3 (A_{11} + 2B_{11} - 3)g_{ij} \\ &+ \frac{1}{4}\gamma(1+\lambda)^2\left\{(A_{12}+B_{12})g_{ij} - \frac{3}{s}\right\}\Bigg] s^2\mathrm{d}s \\ &- \gamma(\lambda^2 + 3\lambda + 1).\end{aligned} \tag{4.15}$$

The values of g_{ij} and the sedimentation coefficients can be calculated numerically which has been done by Batchelor and Wen [8].

We recollect some results for the case of non-Brownian particles and no interparticle forces in Table 4.1.

$\lambda\backslash\gamma$	-2	-1	-0.5	0	0.6	1	1.5	2.25
0.25	-1.96	-2.00	-2.20	-2.56	-3.31	-3.83	-4.73	-6.90
0.5	-2.51	-2.27	-2.28	-2.53	-3.41	-4.29	-6.77	
1			$S_{ij} = -2.52 - 0.13\gamma \quad (\gamma \neq 1)$					
2	3.18	-0.34	-1.89	-2.44	-9.85	-9.81	-11.16	-13.71
4	26.63	10.05	2.03	-2.66	-19.55	-24.32	-32.71	

Table 4.1: Sedimentation coefficients calculated by Batchelor and Wen [8]

4.2 Sedimentation Velocities

4.2.1 Particles of different sizes

Theory

We now use the sedimentation coefficients of Batchelor and Wen [8] (c.f. section 4.1) and the dependency of the sedimentation coefficients on λ and γ to calculate the sedimentation velocities in particle suspensions when the radii ratio of the particles changes.

For constant $\gamma = 1$ and the case of bidisperse suspensions, Eq. (4.3) reduces to

$$\begin{aligned} < U_s > &= U_s^{(0)}(1 + S_{ss}\,\phi_s + S_{sl}\,\phi_l), \\ < U_l > &= U_l^{(0)}(1 + S_{ls}\,\phi_s + S_{ll}\,\phi_l), \end{aligned} \tag{4.16}$$

where the subscript s and l denote the small and large particle species. The sedimentation coefficients S_{ss} and S_{ll} are both equal to -5.6 as in the monodisperse case. The S_{ij} are now a function of λ only. The values calculated by Batchelor and Wen in [8] can be fitted by a polynomial of second order

$$\begin{aligned} S_{sl}(\lambda) &= -3.52 - 1.04\,\lambda - 1.03\,\lambda^2, \\ S_{ls}(\lambda) &= -3.52 - 1.04/\lambda - 1.03/\lambda^2, \end{aligned} \tag{4.17}$$

where λ is defined by $\lambda = a_l/a_s \geq 1$.

Thus we obtaion the settling velocities as functions of λ:

$$\begin{aligned} \langle U_s \rangle &= U_s^{(0)}(1 - 5.6\phi_s - 3.52\phi_l - 1.04\phi_l\lambda - 1.03\phi_l\lambda^2), \\ \langle U_l \rangle &= U_l^{(0)}(1 - 5.6\phi_l - 3.52\phi_s - 1.04\phi_s/\lambda - 1.03\phi_s/\lambda^2). \end{aligned} \tag{4.18}$$

Simulation

We simulate a bidisperse particle suspension in the dilute regime with constant particle concentrations of $\phi_l = \phi_s = 0.01$. The size of the small particles remains unchanged at $a_s = 1$ whereas the size of the large particles is varied between 1 and 2. The system is of size $24 \times 24 \times 24$ and periodic boundary conditions are applied in all directions.

In summary the following parameters are used:

a_s	=	1	ν	=	10
a_l	=	$1 \ldots 2$	g	=	30
$\rho_s = \rho_l$	=	2.5	System size	=	$24 \times 24 \times 24$
$\phi_s = \phi_l$	=	0.01	h	=	0.375

Table 4.2: The parameters used in the simulations.

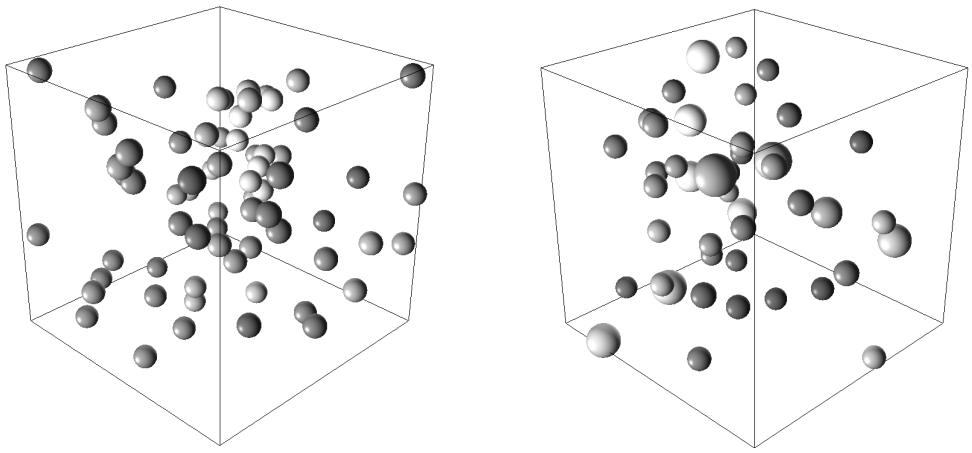

(a) (b)

Figure 4.1: Snapshots of the systems used to calculate the velocity fluctuations. (a) shows a system of size $24 \times 24 \times 24$ with 68 particles of size ratio $\lambda = 1$ and (b) with 44 particles of size ratio $\lambda = 1.5$. The volume fraction of the particles is constant, $\phi_s = \phi_l = 0.01$.

We study the bulk (the so called mixing zone) of the suspension where the particle species are not segregated. We can therefore apply periodic boundary conditions to our system and consider the simulation volume to be located inside the mixing zone of the suspension

and measure quantities associated with the bulk of the suspension. In principle this point of view is not correct, as the periodic boundary conditions still influence various measured quantities, such as the values of the settling velocities and their fluctuations. But even as these values differ for periodic boundary conditions, we have seen that these differences do not affect the effective particle interactions so that the change of the settling velocities with volume fraction is not affected by the periodic setup.

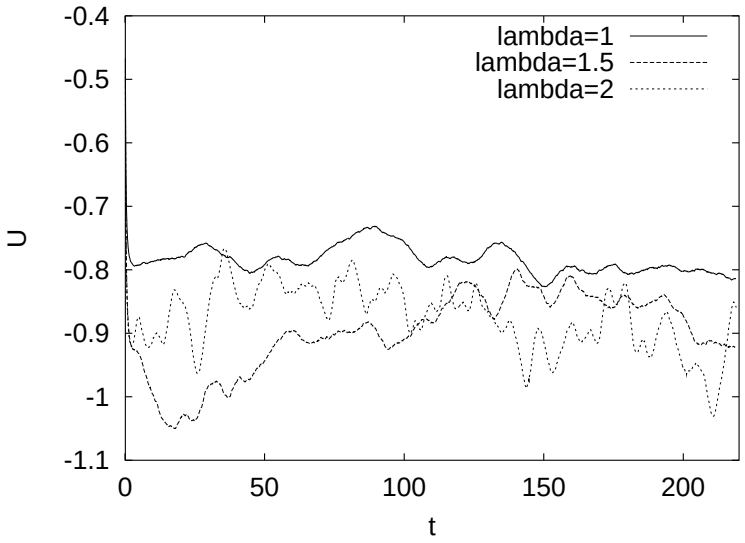

Figure 4.2: Typical examples of the evolution of the mean particle settling velocities for $\lambda = 1, 1.5, 2$.

To reduce the statistical errors of our measurements we perform 30 simulations for each set of parameters. Each simulation runs for at least 200 Stokes times. The statistical evaluation of the simulations starts after 50 Stokes times to ensure that the measured quantities are independent of initial transients. In Figure 4.2 we show the evolution of the ensemble averaged settling velocities of three typical simulations with values of $\lambda = 1, 1.5$ and 2.0. As can be seen the suspension reaches a steady state in very short time due to the dominance of viscous effects: the particles assume velocities comparable to U_{St} almost instantly (timescale $a/U_{\mathrm{St}} \sim a^2/\nu$). Afterwards there are long-lived features where the settling velocities change due to the changes in the local configurations of particles.

In Figure 4.3 we show the predictions of Eq. (4.18) for $\lambda = 1 \ldots 2$ as a dotted lines and the measured values. It is evident that Eq. (4.18) overestimates the velocities. This is due to the limited system size and the periodic boundary conditions, which changes the settling velocities.

For a single particle of radius 1 in the simulated volume, which corresponds to a volume fraction of $\phi = 0.000303$ Batchelors theory predicts the settling velocity to be $U =$

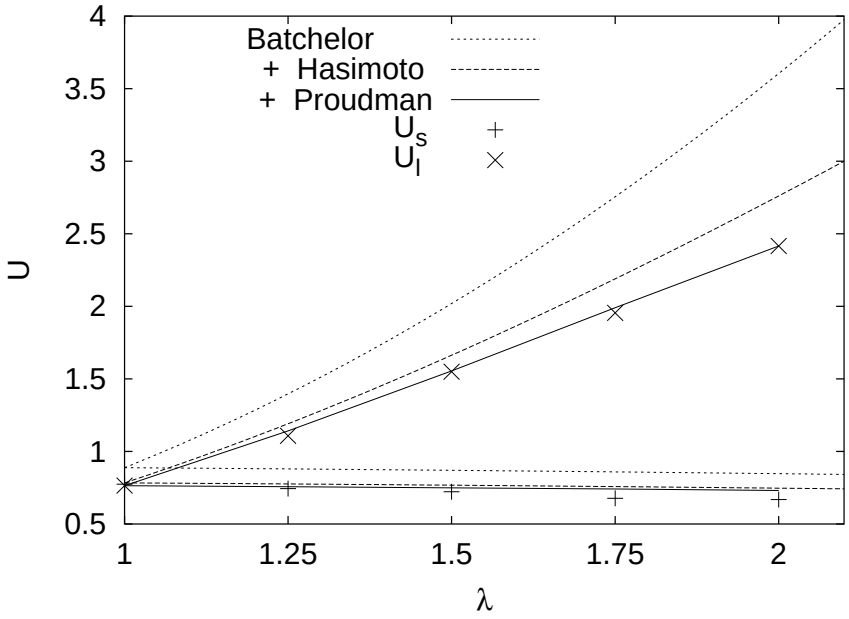

Figure 4.3: The dependence of the settling velocity of small (+) and large ($\times$) particles on λ compared with the predictions of Batchelors theory (dotted lines) and the correction applied for the finite volume (dashed lines) and additional the finite Reynolds number (solid lines).

$1 - 5.6\phi = 0.998$. Due to the periodic boundary conditions the particle *feels* the presence of its periodic images and the settling velocity for the particle is not the one of a single particle but the one for a periodic array of particles. In the limit of low volume fractions the correction to the settling velocity has been calculated by Hasimoto [41] and is given by

$$U/U_\infty = 1 - 1.7601\ \phi^{1/3} + \phi - 1.5593\ \phi^2. \tag{4.19}$$

Note that here, the leading contribution is not linear in ϕ. A single particle of radius 1 will therefore settle with a velocity of $U = 0.882$. We therefore introduce the Hasimoto-corrected single particle velocities $U_i^{\prime(0)}$ with

$$U_i^{\prime(0)} = U_i^{(0)} \left(1 - 1.7601\ \left(\frac{4\pi a_i^3}{3L^3} \right)^{(1/3)} + \frac{4\pi a_i^3}{3L^3} - 1.5593\ \left(\frac{4\pi a_i^3}{3L^3} \right)^2 \right). \tag{4.20}$$

$U_i^{\prime(0)}$ instead of $U_i^{(0)}$ is used to draw the dashed lines in Figure 4.3.

A second correction has to be applied due to the finite Reynolds number. If we consider a single particle settling in an unbounded fluid the settling velocity of the particle will be the Stokes velocity only if the Reynolds number $\mathrm{Re} \to 0$. For finite values of the Reynolds number the settling velocity has to be corrected. Proudman and Pearson [83] calculated

the drag on a sphere at low Reynolds number and found

$$\vec{F} = 6\pi a\eta\vec{U}\left(1 + \frac{3}{8}Re - \frac{9}{40}Re^2 \ln\frac{1}{Re}\right) . \tag{4.21}$$

A change in the particle Reynolds number $\mathrm{Re} = Ua/\nu$ due to a change in the particle velocity or the particle radius would therefore change the drag on the particle. To give a estimate of the magnitude of the correction due the finite Reynolds number we show in table 4.3 the correction to the drag force at various Reynolds numbers.

Re	0.01	0.1	0.2	0.4	0.6	1
$U/U_{\mathrm{St}} = 1 + \frac{3}{8}Re - \frac{9}{40}Re^2 \ln\frac{1}{Re}$	1.004	1.032	1.061	1.117	1.184	1.375

Table 4.3: Correction to the Stokes drag at finite but low Reynolds numbers.

At Reynolds numbers $\mathrm{Re} > 0.1$ the correction is $> 3\%$ and we must therefore apply a second correction to the single particle velocities which we denote by $U_i^{''(0)}$,

$$U_i^{''(0)} = U_i^{'(0)}\left(1 + \frac{3}{8}Re - \frac{9}{40}Re^2 \ln\frac{1}{Re}\right)^{-1} . \tag{4.22}$$

Here we encounter the problem that the single particle velocity $U_i^{''(0)}$ depends on the velocity of the particle due to the velocity dependency of the Reynolds number. To ensure that our measurements are consistent with the theory, we use the measured particle velocity to calculate the Reynolds number for each λ. This measured Reynolds number is then used to calculate the corrected single-particle's velocity $U_i^{''(0)}$.

We now use $U_i^{''(0)}$ in Eq. (4.18) instead of $U_i^{(0)}$ to calculate the settling velocities. The solid lines in Figure 4.3 show the predictions of Batchelors theory after Hasimotos periodic and Proudman and Pearson's finite-Reynolds-number corrections.

The simulation results for the mean settling velocities U_s and U_l show a very good agreement with Batchelors predictions for the large particles, whereas the velocities for the smaller particles are overestimated. This indicates that the increased back flow due to the large particles has a stronger influence than predicted by Batchelor's theory.

We must ensure that this effect is not due to numerical inaccuracies. Errors could arise because particles with different radii have different values of a/h due to the fixed grid spacing h and therefore the quality of the discretization varies with different radii. To estimate the error introduced by the different radii we perform a reference simulation of one particle with radius 1 settling in a periodic box of size 24x24x24 and compare the results to those for a particle of radius 2 settling in the same box. We compare the resulting velocities U_i to the theoretical values. We find that the deviation from the theoretical value

is $\approx 1\%$ for both species and the difference in the errors between the two species is less than 1%. We are therefore confident that the slower velocities are not due to numerical effects caused by the discretization.

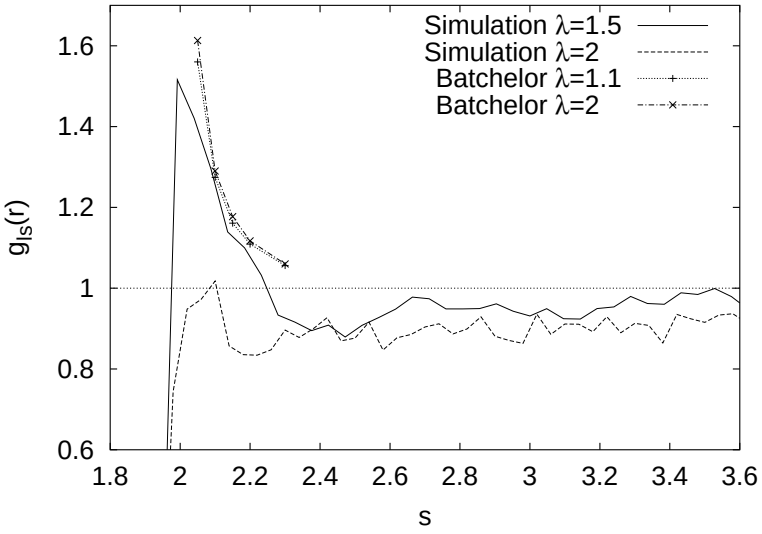

Figure 4.4: Measured pair distribution function g_{ls} for $\lambda = 1.5$ (solid line) and $\lambda = 2$ (dashed line) compared to the theoretical predictions of Batchelor [8] for $\lambda = 1.1$ (dotted line) and $\lambda = 2$ (dashed-dotted line). $s = 2r/(a_i + a_j)$ is the dimensionless distance.

To understand why the small particles settle more slowly than expected we need to look at the spatial structure of the suspension. To this end, we determine the pair distribution function $g_{ij}(r)$, i.e., the probability relative to an entirely homogeneous suspension of finding a particle of species j at distance r from one of species i. Figure 4.4 shows the measured values for the pair distribution function for pairs of one large and one small particle (for $\lambda = 1.25$ and $\lambda = 2$) as a function of the dimensionless distance

$$s = 2r/(a_i + a_j), \tag{4.23}$$

to make the results comparable for different radii ratios λ. The graph indicates that the probability of close pairs decreases as λ increases, which is a genuine three-body effect. Batchelors two-body predictions do not show a significant decrease of the pair probabilities.

The reduction of particle pairs can also be seen in the pair distribution functions calculated by Batchelor but it is much less pronounced. As we have seen in section 4.1 the pair distribution function has been calculated for a dilute suspension by solving a conservation equation for the pair distribution function. In Eq. (4.13) V_{ij} is the relative velocity of pairs of particles. As a consequence the calculated pair distribution function also neglects any effects which are due to three and more particle interactions.

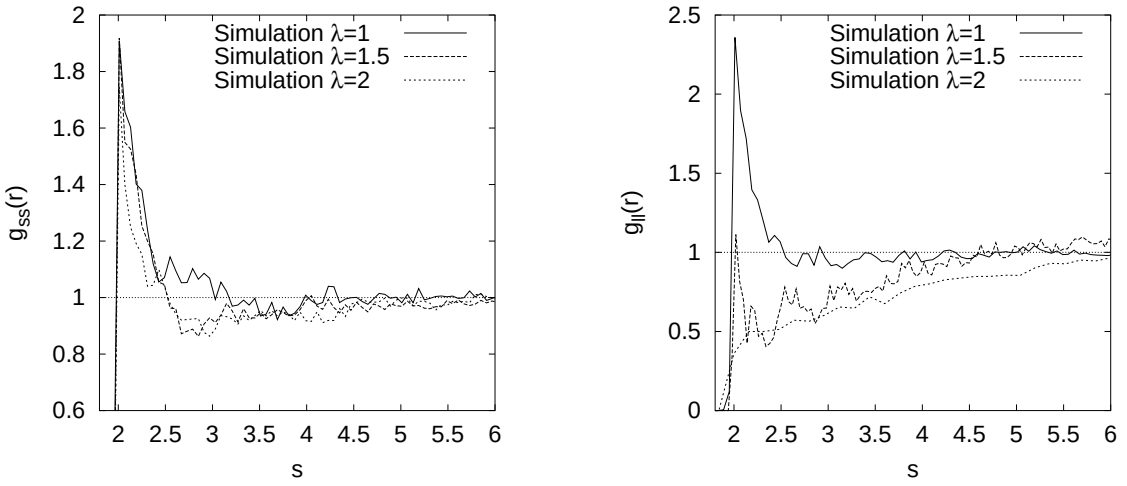

(a) (b)

Figure 4.5: (a) Measured pair correlation function $g_{ss}(r)$ for pairs of small particles for $\lambda = 1$ (solid line), $\lambda = 1.5$ (dashed line) and $\lambda = 2$ (dotted line). (b) shows the measured pair correlation function $g_{ll}(r)$ for the large particles. The values of $g_{ll}(r)$ for $\lambda = 2$ have been measured in a system of size $128 \times 128 \times 128$ to make sure that the decrease of $g_{ll}(r)$ is not due to system size effects.

The decrease of the pair correlation function $g_{ls}(r)$ implies that the correlations g_{ll} or g_{ss} or both differ, which likewise cannot be understood in a particle pair approximation for dilute suspensions. We find that $g_{ll}(r)$ shows a pronounced decrease to values significantly below 1 in the range $s = 2 \ldots 4$ for $\lambda > 1.5$ (cf. Fig. 4.5). Since close pairs settle faster, a reduced probability for such configurations implies smaller settling velocities. This corresponds to the reduction of the velocities due to the higher Reynolds number of the large particles. [a]

The reduction of $g_{ls}(r)$ implies that we have a reduction of the number of small particles in the vicinity of the large particles and therefore more small particles in the back-flow area of the large particles. If we assume that the predicted pair correlation function of Batchelor is correct for viscous flow, then we have to attribute the change in the pair correlation function to the finite Reynolds number.

[a] To quantitatively resolve what the influence of the Reynolds number is one would need to do the same simulations at zero Reynolds number. Our numerical method to simulate the fluid implies that the simulation time step has to be decreased with decreasing Reynolds number. Because of this limitation one would have to solve the Stokes equations rather than the Navier-Stokes equations to overcome this limitations.

4.2.2 Particles of different densities

Now we study the case of suspensions of particles with different densities. We define

$$\gamma = \Delta\rho_h/\Delta\rho_l \geq 1 \tag{4.24}$$

and identify the quantities associated with the heavy and light particle species by the subscript h and l, respectively.

Theory

As described in section 4.1 the settling velocities are described by Eq. (4.3) in the approximation of pair interactions. Batchelor and Wen [8] also calculated the settling coefficients for the case of $\lambda = 1$ and for $\gamma \neq 1$ as a function of γ:

$$S_{ij} = -2.52 - 0.13\gamma. \tag{4.25}$$

We are therefore able to rewrite Eq. (4.3) for a suspension of particles with different densities.

$$\begin{aligned} \langle U_h \rangle &= U_h^{(0)}(1 - 5.6\phi_h - 2.52\phi_l - 0.13\phi_l/\gamma) \\ \langle U_l \rangle &= U_l^{(0)}(1 - 5.6\phi_l - 2.52\phi_h - 0.13\phi_h\gamma) \end{aligned} \tag{4.26}$$

In the limit of $\gamma \to 1$ one would naively expect to find that

$$\lim_{\lambda=1,\gamma\to1} S_{ij}(\gamma,\lambda) = \lim_{\gamma=1,\lambda\to1} S_{ij}(\gamma,\lambda) \tag{4.27}$$

However as can be seen comparing Eq. (4.26) and (4.18), Batchelors calculation suggests that this is not the case. He finds the following values for S_{ij}:

$$\begin{aligned} \lim_{\gamma=1,\lambda\to1} S_{ij}(\gamma,\lambda) &= 5.6, \\ \lim_{\lambda=1,\gamma\to1} S_{ij}(\gamma,\lambda) &= 2.65. \end{aligned} \tag{4.28}$$

As a consequence, even a small difference in the density of the particles should lead to a sharp increase of the sedimentation velocity of more than 27% in our case.

Simulation

Starting from the same setup described in Sec. 4.2.1 with monodisperse and equally dense spheres, we now perform simulations in which the density of one species (h) is increased. We compare the results to the predictions of Eq. (4.26). As the velocities of the particles

change due to the changes in the density, we must also apply the corrections introduced in section 4.2.1 which account for the finiteness of the simulation volume and the finite Reynolds number.

We find that the measured velocities for the heavy species agree with the prediction of Eq. (4.26) of Batchelors theory. The data in Figure 4.6 even suggests the transition from $S_{ij} = 5.6$ at $\gamma = 1$ to $S_{ij} = 2.65$ when $\gamma \neq 1$.

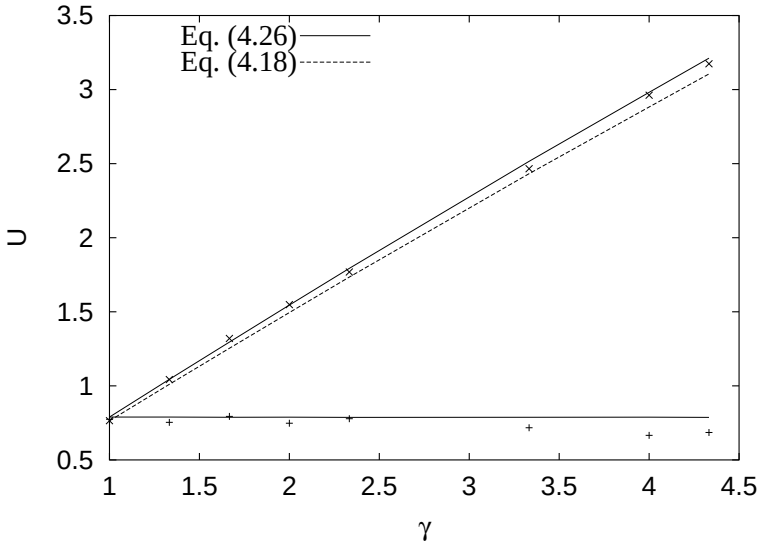

Figure 4.6: The dependence of the settling velocity of light (+) and heavy ($\times$) particles on γ compared with the predictions of Eq. (4.26) and Eq. (4.18) with the corrected single particle velocity of Eq. 4.22. The transition from Eq. (4.18) to Eq. (4.26) when $\gamma \neq 1$ is observed.

Although the predictions of Batchelor are reproduced for the heavy particles, the small particles show a clear deviation from the predictions for larger values of γ. The statistical error of the data in Figure 4.6 is smaller than the size of the symbols used. The same discrepancy has been observed for the suspension with particles of different sizes.

In order to explain this discrepancy we need to better understand the internal structure of the suspension for the case of particles with different densities (Figure 4.7 and 4.8). We see that the probability for pairs of heavy and light particles in close contact increases for increasing density ratio, which is in contrast to the behavior of a suspensions with particles of different sizes (see Figure 4.4). If we look at the probability to find pairs of light particles (Figure 4.8(a)) we see no systematic change for the light particle pairs close to contact. For the heavy particles we find a reduction of pair probability (Figure 4.8(b)) but it is less significant compared to Figure 4.5(b).

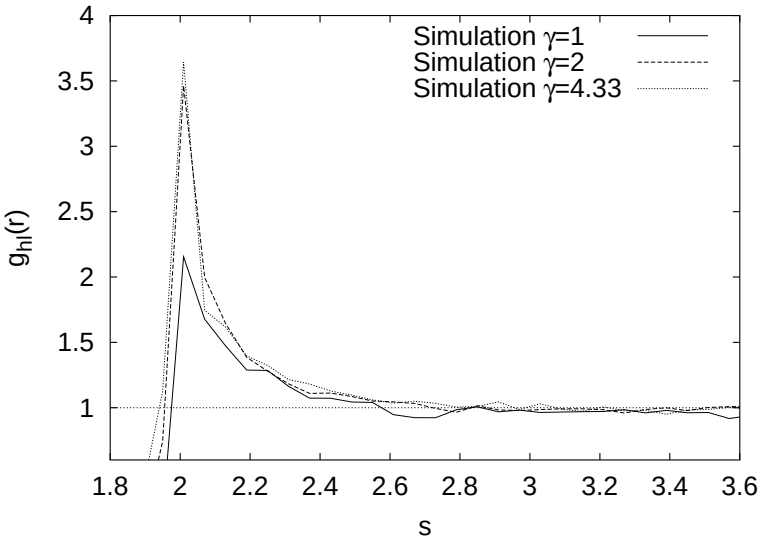

Figure 4.7: Measured pair distribution function g_{ij} for $\gamma = 1.5$ solid line, $\gamma = 2$ dashed line and $\gamma = 4.33$ dotted line. s is the dimensionless distance $s = 2r/(a_i + a_j)$.

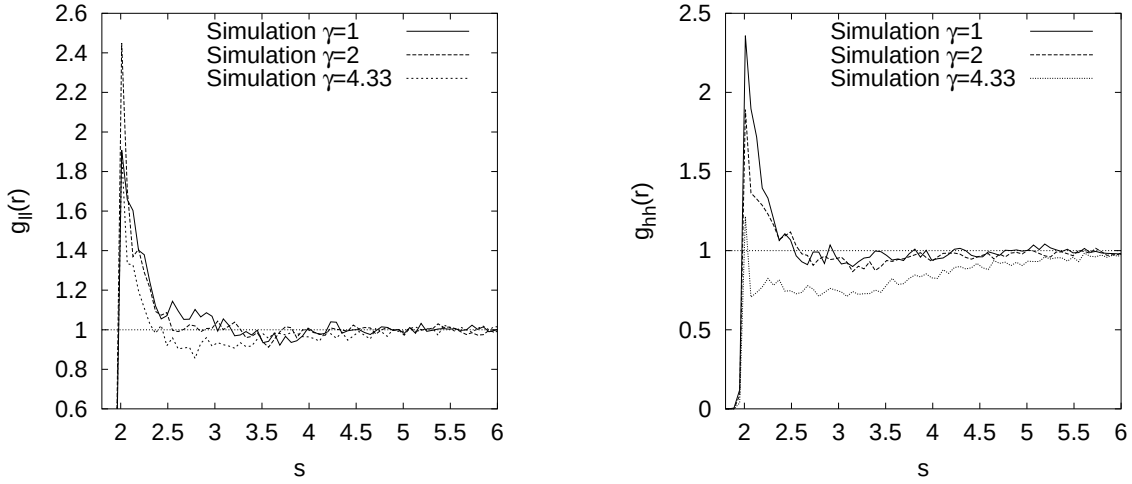

(a) (b)

Figure 4.8: (a) Measured pair correlation function $g_{ll}(r)$ for pairs of light particles for $\gamma = 1$ (solid line), $\gamma = 2$ (dashed line) and $\gamma = 4.33$ (dotted line). (b) shows the measured pair correlation function $g_{hh}(r)$ for the heavy particles.

4.3 Velocity Fluctuations

The prediction of the velocity fluctuations in suspended particle mixtures is of great importance in process engineering. Many chemical processes use fluid or gas suspensions and are sensitive to the diffusivity of the particles. As the velocity fluctuations control the effective diffusivity of the particles it is therefore desirable to understand how the velocity fluctuations change with the properties of the particles.

In contrast to the case of monodisperse suspensions where velocity fluctuations have been studied in detail, much less is known about velocity fluctuations for polydisperse suspensions. The only work on the velocity fluctuations in bidisperse suspensions is, to our knowledge, the experimental study of Peysson and Guazzelli [79, 80]. They track single particles in a bidisperse suspension with $\lambda = 2$ and different concentrations and calculate the mean and variance of the settling velocity for the two particle species. For concentrations of $\phi_L = \phi_S = 0.01$ they find for the velocity fluctuations σ of the two species that

$$\frac{\sigma_S}{\sigma_L} = 0.85, \tag{4.29}$$

and measure the velocity fluctuations as a function of the concentration of the large particles. They find that the fluctuations increase with particle concentrations ϕ_L and propose a scaling of $\sigma \sim \phi^{1/3}$.

We will now take a look at how the velocity fluctuations change when the particle radii ratio λ and the reduced particle density ratio γ are changed. The limit of $\lambda = \gamma = 1$ has been studied in section 3.1, where we have seen that the magnitude of the velocity fluctuations depend on the volume fraction and on the size of the container. The dependency of the velocity fluctuations on the system size will influence the results when λ is varied.

In the limit of $\lambda \to \infty$ or $\gamma \to \infty$ the small/light particles will act like tracer particles in the fluid and will therefore show the same velocity fluctuations as the fluid in a suspension of the large/heavy particles. On the other hand the settling velocity and the velocity fluctuations of the large/heavy particles will be reduced by the increase of the effective viscosity of the fluid with the suspended small/light particles. In the limit of low volume fractions for the small/light particles this increase in the viscosity can be estimated by Einstein's relation

$$\eta_{\text{eff}} = \eta(1 + \frac{5}{2}\phi_S). \tag{4.30}$$

In case of low volume fractions the change in viscosity will be small (e.g. 2.5% at $\phi = 1\%$) and it requires very accurate experiments to measure the influence of the increased viscosity on the velocity fluctuations.

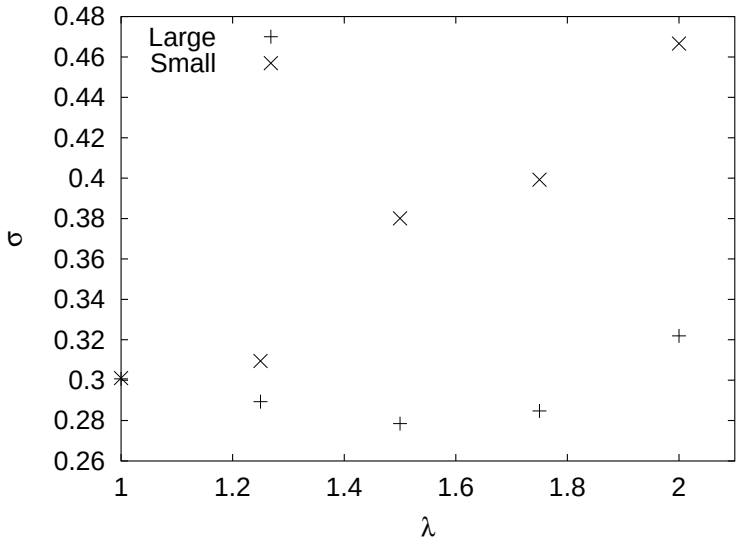

Figure 4.9: Velocity fluctuations in a bidisperse suspension of the large particles (+) and the small particles ($\times$) versus the radii ratio $\lambda = a_L/a_S$.

We will now show and discuss the results of the simulations described in section 4.2.1. In Figure 4.9 we show the measured velocity fluctuations σ for the large and the small particles in a bidisperse suspension. The velocity fluctuations of the small particles increase for increasing radii ratio λ, whereas the velocity fluctuations of the large particles first decrease and then start to increase. The observations for the small particles are easy to understand. Due to the increasing velocities of the large particles ($U^0 \sim \lambda^2$) the settling of the small particles is disturbed and some of the small particles will settle faster in the neighbourhood of the large particles while others will settle slower (or rise faster) as they are in the backflow region of the large particles. So the velocity fluctuations of the small particles are dominated by the large particles. For increasing radii ratios λ we will get closer to the case where the small particles are just tracer particles for the velocity fluctuations in the fluid.

In case of the large particles we have three effects which govern the velocity fluctuations:

1. The single particle velocity of the large particles scales approximately with $U^0 \sim \lambda^2$. As the fluctuations should be proportional to U, we would expect an influence of $O(\lambda^2)$ on the velocity fluctuations.

2. The relative size of the container decreases with increasing λ. As we have a container size dependency of order $O(\sqrt{L/a_L})$ (cf. section 3.1) we would expect the resulting effect to be of $O(1/\sqrt{\lambda})$

3. For $\lambda = 1$ we have one single particle species with a volume fraction $\phi = \phi_S + \phi_L$.

When λ is increased the large particles will become more and more independent from the influence of the small particles – they decouple. This will reduce the initial volume fraction and ϕ will reduce to the volume fraction of the large particles only $\phi = \phi_L$. As the fluctuations increase with increasing volume fractions up to $\phi = 0.3$ [75], we expect a reduction of the velocity fluctuations due to the decoupling of the large particles from the small particles.

To see when the decoupling of the two particles species occurs we scale the fluctuations with the velocity of the large particles and divide it by $\sqrt{\lambda}$ for the large particles to account for the size dependency of the velocity fluctuations. As we see in Figure 4.10, the fluctuations decrease rapidly and reach a constant value at $\lambda \approx 1.8$.

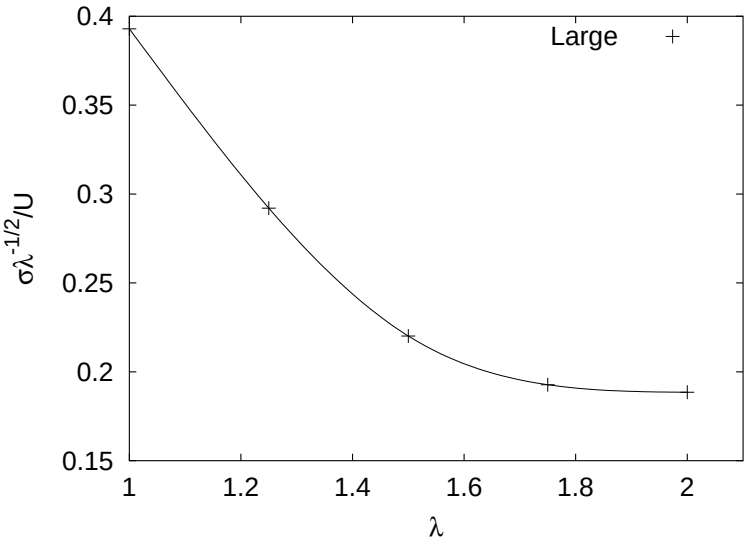

Figure 4.10: Velocity fluctuations of the large particles scaled with the mean sedimentation velocity U and $\sqrt{\lambda}$ to account for the dependency of the velocity fluctuations on U and the system size L/a respectively. The rescaled velocity fluctuations decrease and reach a constant value at $\lambda \approx 1.8$.

The value of the rescaled fluctuations at $\lambda = 2$ is about half of the initial fluctuations. We would have expected that the reduction of the velocity fluctuations due to the decoupling of the two particle species would have been about $\sqrt{2}$. This indicates that there might another mechanism (besides the decoupling) that reduces the velocity fluctuations.

We now turn to simulations of suspensions with particles of different densities. As the sizes of the particles do not change, we do not see system size dependencies for different values of γ, and the main contribution to changes in the velocity fluctuations will be from the increasing settling velocities of the heavy particles. The setup of the simulations has been discussed in section 4.2.2.

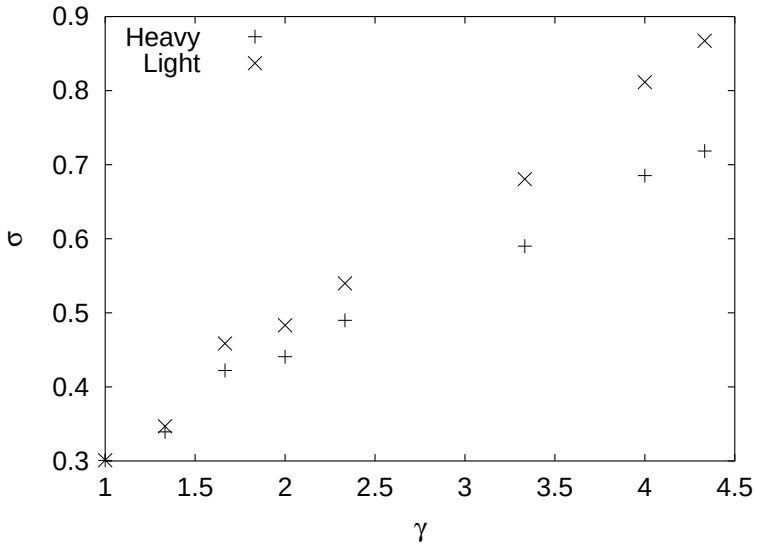

Figure 4.11: Velocity fluctuations in a suspension of two particle species with different densities for the heavy particles (+) and the light particles ($\times$) versus the reduced density ratio $\gamma = (\rho_h - \rho)/(\rho_l - \rho)$.

In Figure 4.11 we show the measured values. The main difference with respect to the measurements where λ was varied is that the heavy particles do not show a initial decrease of the velocity fluctuations in contrast to the large particles. For both species, the heavy and the light particles, the fluctuations increase roughly linearly in λ and the light particles show slightly larger fluctuations.

To compare the results of the simulations where $\gamma \neq 1$ with the results of the simulations where $\lambda \neq 1$, we scale the velocity fluctuations with U and in Figure 4.12 compare the results of Figure 4.10 with the rescaled data of Figure 4.11. We find that the qualitative behaviour for variations of γ and λ is the same, but that the reduction of the rescaled velocity fluctuations at the same relative velocity of the particles is more pronounced for variations of λ.

Another interesting quantity is the ratio of velocity fluctuations for large and small particles. Yannik Peysson found in his experiments [79] with a bidisperse suspension where the particle radii ratio was $\lambda = 2$, that the ratio was

$$\frac{\sigma_S}{\sigma_L} = 0.75 \pm 0.05. \tag{4.31}$$

To explain their results, they used the scaling argument by Hinch and considered a spherical region of size L with $N_1 = \phi(L/a_1)^3$ and $N_2 = \phi(L/a_2)^3$ particles respectively. The fluctuations in the number of particles is of order $\sqrt{N_1}$ and $\sqrt{N_2}$ if the particles are

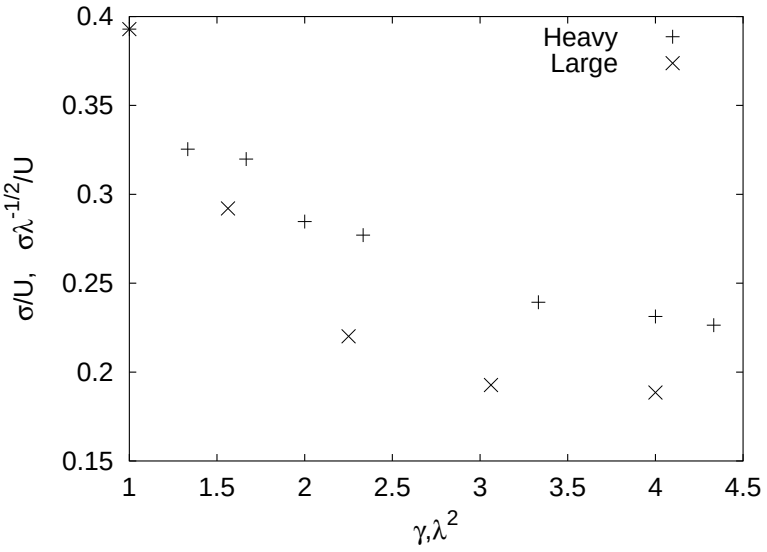

Figure 4.12: Rescaled velocity fluctuations of the heavy particles in a suspension of particles with different densities (+) compared with the rescaled velocity fluctuations of the large particles in a bidisperse suspension.

randomly distributed. The resulting velocity fluctuations would be of size

$$\sigma \approx (\sqrt{N}_1 a_1^3 + \sqrt{N}_2 a_2^3)\Delta\rho g/6\pi\eta L \tag{4.32}$$

They now introduce a virtual radius $a_0^3 = (\sqrt{N}_1 a_1^3 + \sqrt{N}_2 a_2^3)/\sqrt{N_1 + N_2}$ and a characteristic radius $a_m^3 = (N_1 a_1^3 + N_2 a_2^3)/(N_1 + N_2)$. With V_{S0} being the Stokes velocity of a virtual particle of size a_0 and $\phi = \phi_1 + \phi_2$ the total volume fraction, Eq. (4.32) can be written

$$\sigma \approx V_{S0}\sqrt{\phi(L/a_0)}(a_0/a_m)^{3/2}. \tag{4.33}$$

In [80] Peysson and Guazzelli now assume that they can calculate the correlation length ξ of each species by

$$\xi_i \approx \frac{a_i}{\phi^{1/3}}\left(\frac{a_m}{a_0}\right)^3. \tag{4.34}$$

The first part of the right hand side of this assumption is motivated by Segrès' [93] finding for monodisperse suspensions that $\xi \sim a_i\phi^{-1/3}$ whereas the second part has not been motivated. They assume that ξ from Eq. (4.34) can be used as L in Eq. (4.33). But it should be noted that a_0 and a_m both depend on N_i and therefore on L. Therefore ξ given in Eq. (4.34) also depends on L.

If we use Eq. (4.34) and set $\xi = L$ and solve for L we find $L = 3.2a_1$ for the small and $L = 6.5a_1$ for the large particles, which is significantly smaller than typical correlation lengths measured in experiments.

We also doubt that the effective volume fraction in a bidisperse suspension is the sum of the volume fractions of the two species, except in the limit of $\lambda \to 1$.

Nevertheless Peysson and Guazzelli find that the ratio of the velocity fluctuations for the two particle species should be of size

$$\frac{\sigma_S}{\sigma_L} = \sqrt{\frac{a_S}{a_L}}, \tag{4.35}$$

which agrees with their measurements.

In our simulations we find that the value of $\sigma_S/\sigma_L = 1.7$ for a radii ratio of $a_S/a_L = 1/\lambda = 0.5$. This is significantly larger than the values predicted and measured by Peysson and Guazzelli.

One cause of the differences between the simulations and the experiments is again found in the system size dependency of the velocity fluctuations. We use the same scaling laws as derived in section 3.1 to draw the velocity fluctuations vs. the scaled system size. Figure 4.13 shows the results of the bidisperse simulations ($\lambda = 2$) together with the monodisperse simulations of section 3.1.

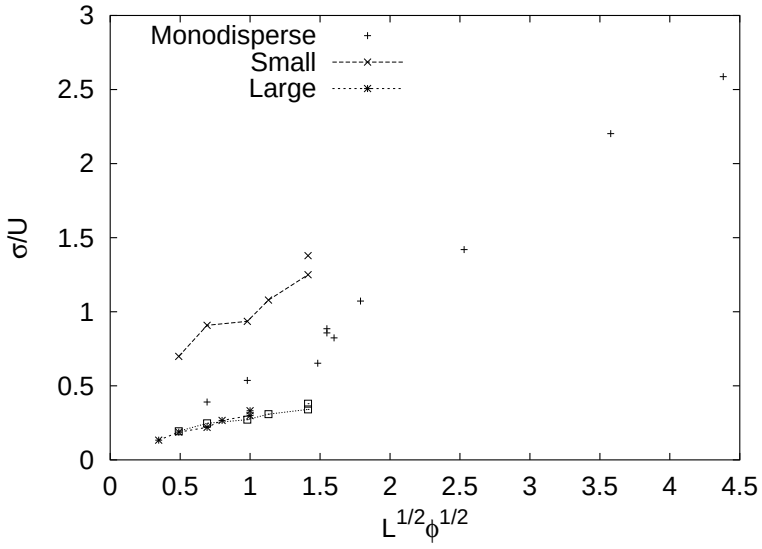

Figure 4.13: Scaling of the velocity fluctuations with the system size in a bidisperse suspension for the small particles ($\times$), the large particles ($*$) compared with simulations of monodisperse suspensions (+). The radii ratio was $\lambda = 2$ and the Reynolds number on the scale of the small particles $Re = 0.1$. We also show the velocity fluctuations for the small particles scaled with the velocity of the large particles ($\boxdot$).

We find that the fluctuations of the small particles ($\times$) scaled with their velocity are larger than in the monodisperse case. This is to be expected as we will see later. The fluctuations

of the small particles are dominated by the velocities and the velocity fluctuations of the large particles. We therefore also show the fluctuations of the small particles scaled with the average settling velocity of the large particles (⊡) which shows a close match with the measured velocity fluctuations for the large particles (∗). The velocity fluctuations for the large particles show a different scaling with the system size compared to the monodisperse case.

Due to the fact that the velocity fluctuations of the small and the large particles scale differently when the system size is changed, measurements in systems with different sizes will give different results for the ratio of the velocity fluctuations.

In Figure 4.14 we show the ratio of the velocity fluctuations σ_S/σ_L versus the particles size ratio $\lambda = a_L/a_S$.

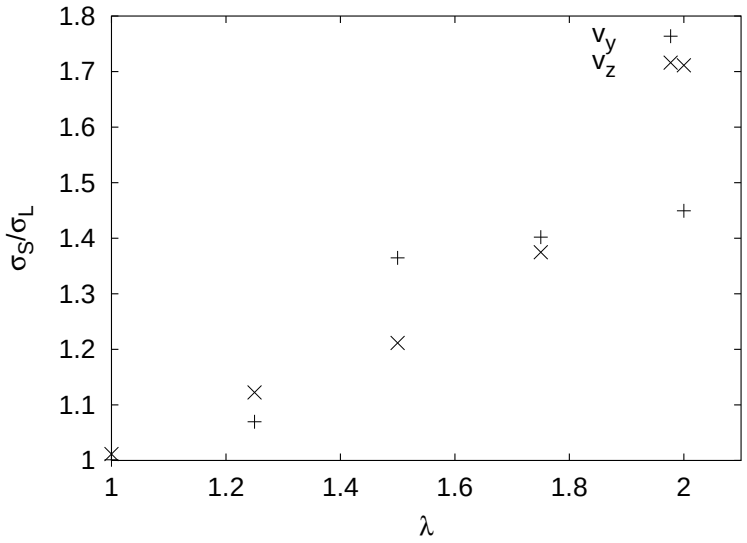

Figure 4.14: Ratio of velocity fluctuations σ_S/σ_L versus the particles size ratio $\lambda = a_L/a_S$ for the velocity component parallel (+) and perpendicular ($\times$) to gravity.

Chapter 5

Modeling of Polydisperse Suspensions

So far we have studied systems which were infinite or periodic in the direction of gravity. In such systems no large-scale separation of the involved particles species can emerge. However, in systems, where the translational invariance in vertical direction is broken, e.g, by the presence of horizontal walls, distinct regions with different concentrations of the particle species will emerge. This is sketched in Figure 5.1 for a bidisperse suspension. At the top of the vessel there is a region void of particles, because all species have moved downwards. Below, we find a region (I) with predominantly small, slowly settling particles then a mixed region (II), in which still both species are present, and, finally, at the bottom, a sediment, in which the fraction of large, quickly settling particles is increased. The transition zones display a smooth change in the particle concentrations.

Most macroscopic theories describing the evolution of volume fractions in multidisperse suspensions are based on the well known Kynch theory [57]. If the hindered settling function is known the evolution of the volume fractions can be calculated. As long as the hindered settling function is a monotonous decreasing function of the concentration the Kynch model leads to jumps in the concentrations, because e.g. a continuous concentration gradient from a concentration ϕ_0 at y_0 to $\phi = 0$ at $y_0 + \Delta y$ will result in a situation where the particles above y_0 settle faster than the particles at y_0 and therefore the width of the transition zone Δy will reduce. This mechanism is called the self-sharpening effect [57]. Experimental investigations showed that the interfaces in multispecies suspensions are broadened due to polydispersity and hydrodynamic diffusion [18, 19, 36, 64]. To account for this effect the theory of Kynch must be extended. This can be done by adding a diffusive component to Kynch's purely advective theory.

Many measurements on bidisperse suspensions have been performed, but most deal with the settling velocities of either the interfaces or single particles within the different zones of the suspension. Less publications are found on the measurements of volume fractions.

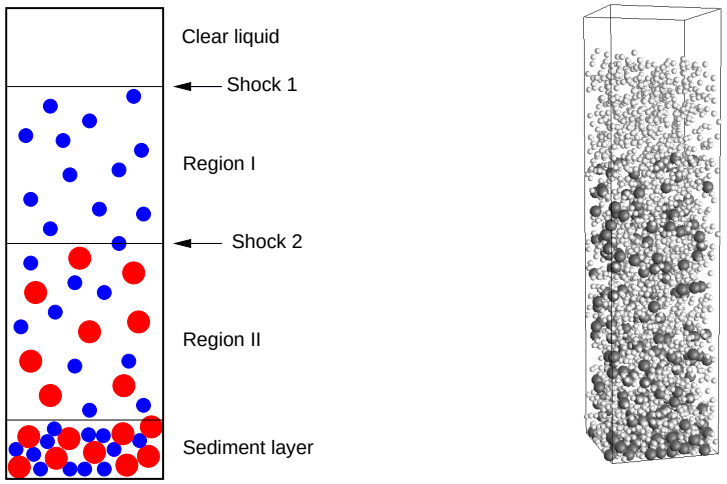

(a) (b)

Figure 5.1: (a) Sketch of the particle distribution within a bidisperse suspension and (b) a snapshot of a (small) simulation.

Especially measurements where the volume fraction is measured for each species separately are not easy to perform experimentally. Therefore, we simulate the settling of bidisperse suspensions to get a more detailled insight on the evolution of the volume fractions. We compare the results of our three-dimensional simulations first with a model based on Kynch's theory and second with a advection-diffusion model, which accounts for the hydrodynamic diffusion in particle suspensions.

5.1 The Kynch based Model

In order to allow the description of the three-dimensional problem of a particle suspension by a set of one dimensional partial differential equations the following conditions must be fulfilled. Firstly the extensions of the system in the directions perpendicular to gravity must be much larger than the size of the particles. The result then does not depend in detail on the boundaries. The second requirement is that the initial conditions of the suspension are homogeneous in the directions perpendicular to gravity. Thirdly, there should be no physical processes inducing lateral inhomogenities, as present e.g. in the case of settling in inclined containers [1].

In order to model this kind of system, we define local particle volume fractions by averaging over thin horizontal slices of the system [57], in which the particle concentrations do not change appreciably as functions of the vertical coordinate. In this way, the

problem is reduced to one dimension. The concentration changes due to vertical particle currents. These currents are assumed to be a function of the local concentrations $\Phi = (\phi_1(y), \phi_2(y), \dots)$ only. Here y is the vertical direction, parallel to gravity. The conservation of mass for each species $i = 1, \dots, N$ is expressed in the N hyperbolic conservation equations

$$\frac{\partial \phi_i}{\partial t} + \frac{\partial\, \phi_i U_i(\Phi)}{\partial y} = 0. \tag{5.1}$$

As the hindered settling function $U_i(\Phi)$ is a decreasing function of ϕ_i, Eq. (5.1) leads to discontinuities, so called shock fronts, propagating with the velocity V_S. The velocity of the shock can be calculated by evaluating the continuity equation at the shock

$$(U_i^+ - V_S)\phi_i^+ = (U_i^- - V_S)\phi_i^-, \tag{5.2}$$

where U_i^+, ϕ_i^+, U_i^-, and ϕ_i^- denote the values of U_i and ϕ_i above and below the discontinuity, respectively. Thus the velocity of the shock is

$$V_S = \frac{U_i^+\phi_i^+ - U_i^-\phi_i^-}{\phi_i^+ - \phi_i^-}, \tag{5.3}$$

which is also called the Rankine-Hugoniot condition. In case of a monodisperse suspension of initial concentration ϕ the shock front separates the homogeneous suspension from the clear fluid at the top.

Given the initial and boundary conditions, we solve Eq. (5.1) numerically. The numerical methods must take into account the jump conditions at the locations of the shocks. This is done either by using the jump condition explicitly or by employing so called *shock-capturing* schemes, which will approximate the physically relevant solution.

Properties of the Hindered Settling Function

In order to solve Eq. (5.1) we have to know the hindered settling function. There are many different empirical proposals for the hindered settling function in multidisperse suspensions [21, 65, 68, 74, 77]. Theoretical predictions of the hindered settling function are due to Batchelor [6], Hinch [42],and Brady and Durlofsky [13].

As we have seen in chapter 4, Batchelor's theory for dilute suspensions describes the behavior of polydisperse suspensions accurately. Therefore we base our modeling on Batchelor's hindered settling function but in order to simplify the modeling, we require that the hindered settling function vanishes as we approach the maximum total volume

fraction $\phi_t \equiv \sum_i \phi_i \rightarrow \phi_\infty$.[a] We therefore extend Batchelor's form

$$\langle U_i \rangle = U_i^{(0)}(1 + \sum_{j=1}^{N} S_{ij}\ \phi_j) \tag{5.4}$$

to a nonlinear equation

$$\langle U_i \rangle = U_i^{(0)} \frac{e^{\left(1+\sum_j S_{ij}\phi_j + 2\phi_t/\phi_\infty\right)}(\phi_\infty - \phi_t)^2}{e\ \phi_\infty^2} \tag{5.5}$$

which preserves the asymptotic behavior as $\phi_i \rightarrow 0$, but vanishes at $\phi_t = \phi_\infty$. We compare the form (5.5), Batchelor's hindered settling function (5.4) and the empirical relation of Richardson and Zaki [86] in Fig. 5.2.

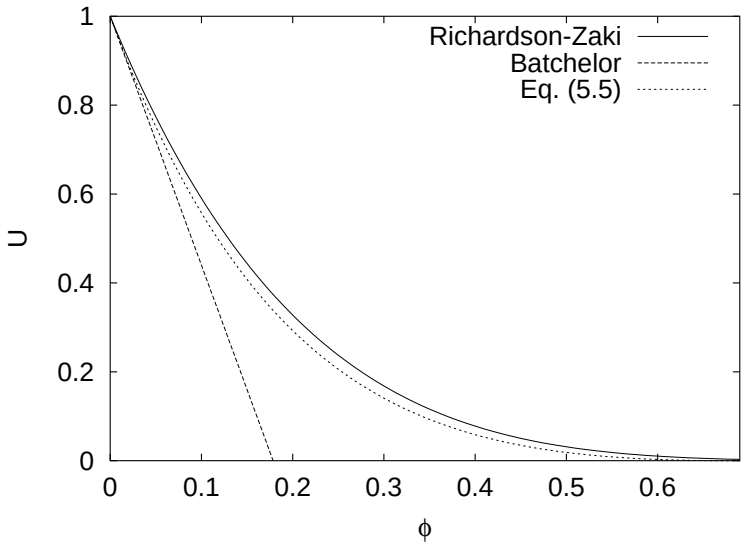

Figure 5.2: Hindered settling function Eq. (5.5) used in the advection diffusion model Eq. (5.7). We also show the results of Batchelor Eq.(5.4) and the phenomenological relation of Richardson and Zaki [86].

5.1.1 Comparison with Simulation Results

We consider particles of size $a_s = 1$ and $a_l = 1.41$ in a vessel with quadratic cross-section of size $36 \times 567 \times 36$ with walls at the bottom and top and periodic boundary conditions in the other directions. This setup is chosen to resemble a settling column where the walls are far apart from the center, so that their influence can be neglected.

[a] There is no single maximum total volume fraction for polydisperse suspension, because the maximum volume fraction of the sediment depends on the ratio of the particle radii and the actual composition of the sediment. To simplify our argumentation we assume a single value for the maximum volume fraction ϕ_∞. Also, the hindered settling function need not vanish at ϕ_∞, because in three dimensions flow through dense packed spheres is still possible.

In summary the following parameters are used for the simulations:

$\lambda = a_l/a_s$	1.414
$\phi_{l,s}$	0.05
L_x,L_y,L_z	36, 576, 36
$\rho_{l,s}$	2.5
g	30
Re	0.1

Figure 5.4 shows the iso-concentration lines of a) the small and b) the large particles obtained by drawing the concentration of the particles as a function of the height y and the time. The long-dashed, short-dashed, dotted and dash-dotted lines show the concentrations of the three dimensional simulation and correspond to $\phi_l = 0.1, 0.06, 0.04$ and 0.01, respectively. The solid lines correspond to the numerical solution [14] of the advection model and to the denoted concentration values.

Figure 5.5 shows the concentration profiles for different times. The results of the small and the large particles are shown in Figure 5.5(a) and (b), respectively.

In the three-dimensional simulations we find that the concentration of the small particles increase with time above the initial concentration of $\phi_s = 0.05$ (cf. Fig. 5.4(a)). The increase in concentration occurs in the region of the suspension where only the small particles are present and saturates at a value of $\phi_s \approx 0.064$.

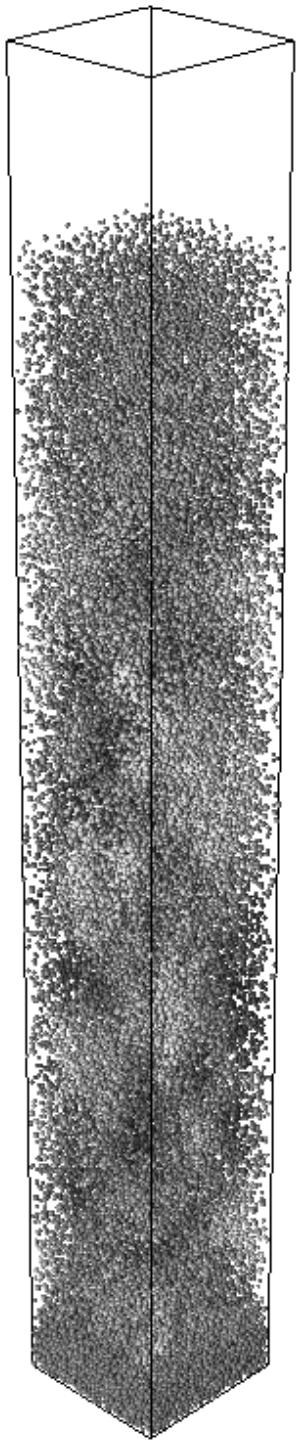

Figure 5.3: Simulation of a bidisperse suspension used to compare with the one-dimensional model equations.

The enrichment of small particles in region I follows directly from the continuity condition (5.2) if we look at the initial condition where the concentration of the small particles is (approximately) the same above and below the shock 2. The effective flux Θ of small particles from the top to the bottom is then given

a)

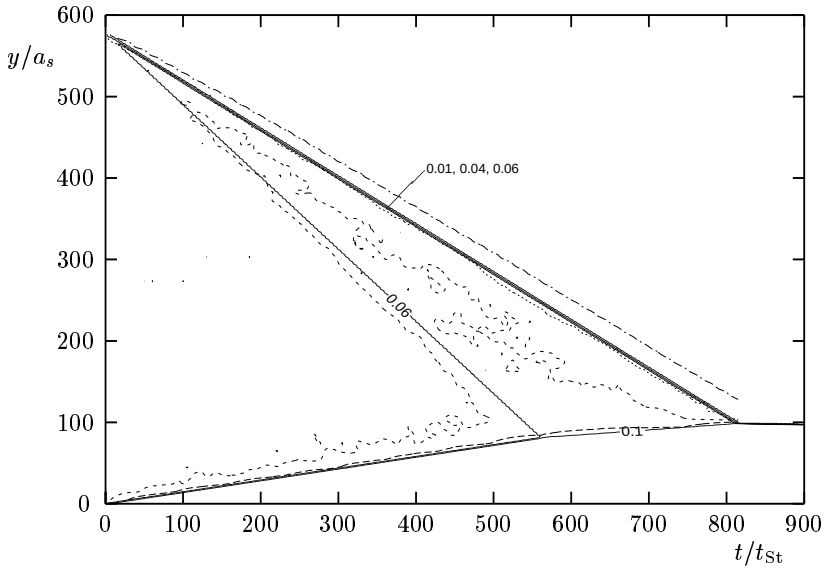

b)

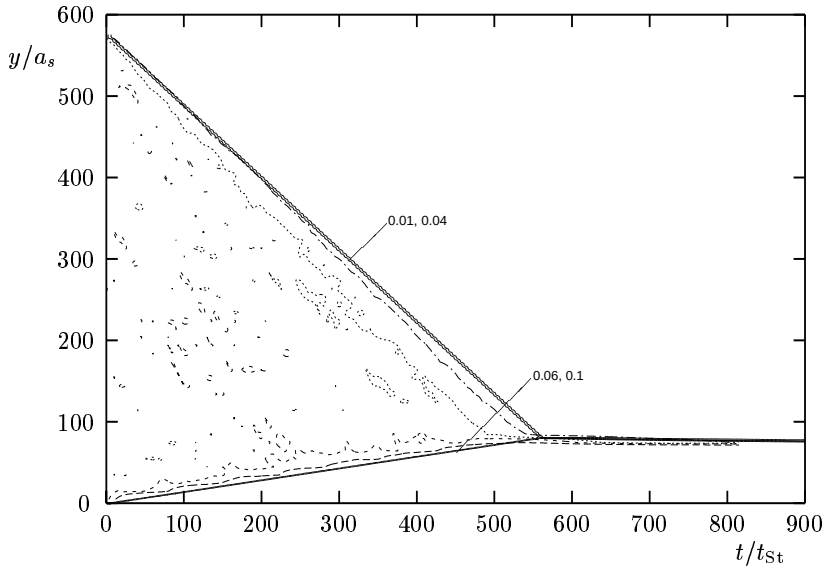

Figure 5.4: Iso-concentration lines of a) the small and b) the large particles. The concentration profiles are generated by drawing the concentration profiles as a function of the height y for different time next to each other. The long-dashed, short-dashed, dotted and dash-dotted lines show the concentrations obtained by the three dimensional simulation and correspond to $\phi_l = 0.1, 0.06, 0.04$ and 0.01, respectively. The solid lines correspond to the numerical solution [14] of the advection model and to the denoted concentration values.

a)

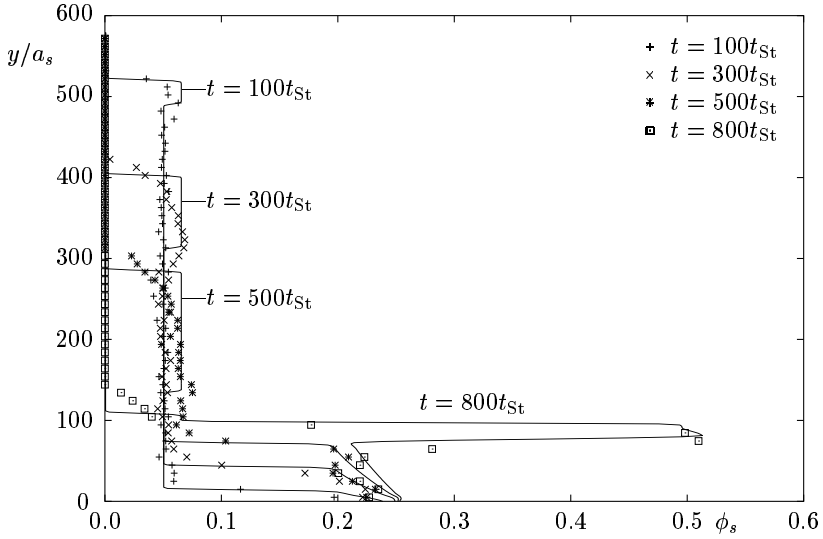

b)

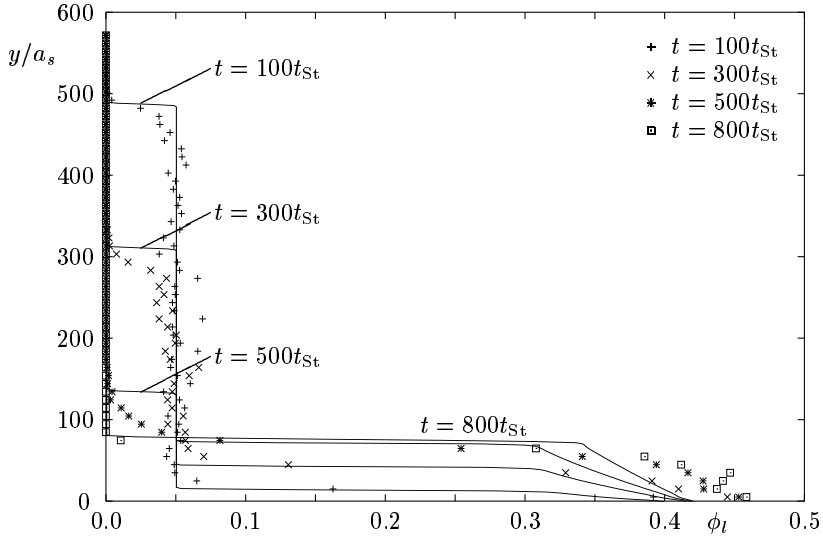

Figure 5.5: Concentration profiles of the small particles a) and the large particles b). The symbols show the results of the three dimensional simulations and the solid lines the numerical solution of the convection model.

by

$$\Theta = (U_i^+ - V_S)\phi_i^+ - (U_i^- - V_S)\phi_i^- \tag{5.6}$$

As U_i^- is smaller than U_i^+ due to the presence of the large particles in region II we have a negative net flux of small particles, until the concentration ϕ_i^+ of small particles above shock 2 is higher than below the shock.

In addition to the enrichment of the small particles volume fraction the width of the transient zone between the small particles and the clear fluid increases. The width of the transient zone between region I and region II is even more enlarged compared to the transient zone between region I and the clear fluid.

We find that a purely advective model predicts the location of the shock and the magnitude of the enhancement of the small particle concentration accurately. It also predicts the particle concentrations in the sediment. The advection model cannot render the finite width of the shock which is caused by the presence of hydrodynamic diffusion. Also the enrichment of small particles above the mixed particle region occurs instantaneously, which is not the case in the simulations. We can therefore say that a advection model is only applicable when the length scale considered is much larger than the width of the transition regions.

5.2 The Advection-Diffusion Model

It is not difficult to extend the advective model (5.1) by a diffusive contribution. To this end we assume that vertical particle currents have two components. One is due to the downward settling motion $\phi_i(y)U_i(\Phi)$. The other describes the random, diffusive component of the motion and is proportional to the gradient of the volume fraction: $-D_i(\Phi)(\partial/\partial y)\phi_i(y)$. The continuity equations for each species then turn into an advection-diffusion equation,

$$\frac{\partial \phi_i}{\partial t} = -\frac{\partial}{\partial y}\left(\phi_i U_i(\Phi) - D_i(\Phi)\frac{\partial \phi_i}{\partial y}\right). \tag{5.7}$$

This type of equation has been proposed previously [19, 64, 67] for the monodisperse case. Provided that $D(\Phi) = D$ and $U_i(\Phi)$ are both constant the solution is known to be

$$\phi(y,t) = \phi_0\left(1 - \mathrm{erf}\left(\frac{y - V_S t}{\sqrt{4Dt}}\right)\right)/2, \tag{5.8}$$

under the boundary condition that the concentration is equal to 0 and ϕ_0 for $y = +\infty$ and $y = -\infty$, respectively. Because the diffusion coefficient in suspensions changes when the volume fraction is varied, the solution (5.8) does not apply for suspensions. But, due to

the fact that self-sharpening and diffusion broadening have opposing effects on the front, they can balance each other and form a stabilized profile. This will hold for any functional form of the hindered settling function that leads to self-sharpening [57].

In the case of a monodisperse suspension we calculate the traveling profile for a given hindered settling function and a given functional form of the diffusion coefficient in the frame of reference of the moving profile. By applying the transformation

$$\zeta = y - V_S t, \tag{5.9}$$

where V_S is the velocity of the stationary profile, we determine the stationary profile by solving

$$\frac{\partial \phi(\zeta)[U(\phi) - V_S]}{\partial \zeta} = \frac{\partial D(\phi)\frac{\partial \phi}{\partial \zeta}}{\partial \zeta}, \tag{5.10}$$

which yields

$$\phi(\zeta)[U(\phi) - V_S] = D(\phi)\frac{\partial \phi(\zeta)}{\partial \zeta} + A \tag{5.11}$$

where the values of V_S and the integration constant A are determined by the boundary conditions at $+\infty$ and $-\infty$. If we consider the top front between the clear fluid and the particles of a initially homogeneous suspension of concentration ϕ_0 we find $A = 0$ and $V_S = U(\phi_0)$. The resulting integral

$$y - V_s t = \int_0^{\phi} \frac{D(\phi')}{\phi'(U(\phi') - V_S) + A}\, \mathrm{d}\phi' \tag{5.12}$$

can be integrated at least numerical for a given set of a hindered settling function and a diffusion coefficient.

In experiments the particles are not monodisperse and thus the experiments have to take the polydispersity of the particles into account. Particles of different sizes will have different velocities. Therefore the width of the interface will increase proportional to t. The interface spreading due to a diffusion is $\sim \sqrt{t}$. Thus the spreading of the interface at the beginning of the sedimentation process is dominated by diffusion, and it is in principle possible to separate the two contributions in experiments.

Properties of the Diffusion Coefficient

In contrast to the purely advective model of section 5.1 we have to provide not only the hindered settling function $U(\Phi)$ but also the diffusion coefficient $D(\Phi)$ to calculate the evolution of the particle concentrations. Analogous to the hindered settling function the diffusion coefficients have to fulfill some constraints.

In the case of high volume fraction the mobility of the particles is reduced, and at least for $\phi_t = \phi_\infty$ the particles get immobile and the diffusion coefficients of all particle species must vanish. There is also no diffusion for $\phi_t \to 0$ because in the limit of independent particles the trajectory of the particle is a straight line.

Measurements of Nicolai [75] and calculations of Schwarzer [92] showed for monodisperse suspensions that the diffusion coefficient increases for dilute suspensions $\phi < 0.1$ with increasing particle volume fractions and decreases for $\phi > 0.1$. In case of polydisperse suspensions the local concentrations of all particle species Φ determine the diffusion coefficient of a species.

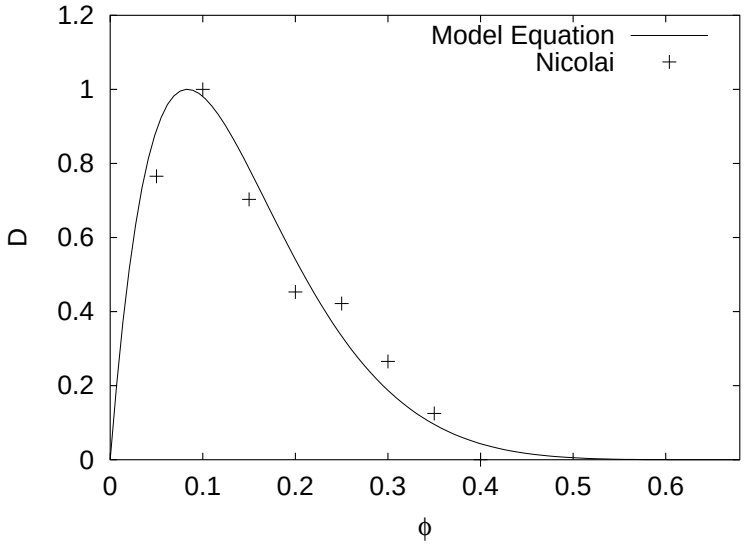

Figure 5.6: Diffusion coefficient Eq. (5.13) used in the advection diffusion model Eq. (5.7) compared with the normalized experimental data of Nicolai [75].

For the diffusion coefficients $D_i(\Phi)$ we propose the following empirically expression

$$D_i(\Phi) = D_{\max} A \, a_i U_i^{(0)} \phi_i \left(\frac{U_i(\Phi)}{U_i^{(0)}} \right)^2 , \tag{5.13}$$

which shows good agreement with the measurements of Nicolai *et al.* [75] (cf. Fig. 5.6). For $A = 31.54$, the maximum value of D_i is $D_{\max}$. So $D_{\max} = 6.4$ corresponds to a maximum of $D_i / a_i U_i^{(0)}$ of 6.4.

The Stationary Profile

With the model equation for the diffusion coefficient (5.13) and the hindered settling function (5.5) given, it is possible to integrate Eq. (5.12) numerically for a monodisperse

suspension and we can find an analytical solution of the concentration profile for special choices of $U(\phi)$ and $D(\phi)$. Especially for a linear hindered settling function $U = U_0(1 - C\phi)$ and a constant diffusion coefficient $D = D_0$ Eq. (5.13) becomes a Burger's equation, where the solution is known for all times, and the stationary profile takes the form

$$\phi(\zeta) = \phi_1 + \frac{\phi_2 - \phi_1}{1 + e^{(U(\phi_2) - U(\phi_1))\zeta/2D}}. \tag{5.14}$$

In Figure 5.7 we show the stationary solution of (i) the Burger's equation (solid line) (ii) of our model with the hindered settling function given by Eq. (5.5). Furthermore we display the solution for a constant diffusion coefficient (dashed line) and the diffusion coefficient given by Eq. 5.13 (dotted line). The profiles described by the Burger's equation corresponding to a linear hindered settling function and constant diffusion coefficient is almost S-shaped. The nonlinear hindered settling function Eq. (5.5) with a constant diffusion coefficient also shows an S-shape but the width is increased due to the nonlinearity of the hindered settling function. The usage of a concentration dependent diffusion coefficient modifies the S-shape of the profile. Especially at low volume fractions the S-shape is truncated and the characteristic tail is suppressed.

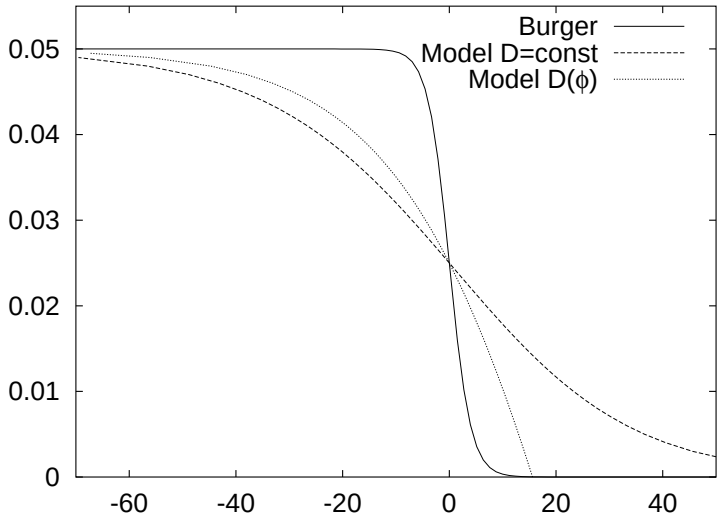

Figure 5.7: Stationary concentration profile of the Burger's equation Eq. (5.14) with $D = 4$ (solid line) and of the advection diffusion model with the nonlinear hindered settling function Eq. (5.5) and a constant diffusion coefficient $D = 4$ (dashed line). The dotted line shows the stationary profile for the concentration dependent diffusion coefficient Eq. (5.13).

5.2.1 Comparison with Simulation Results

In this section we compare the results of three dimensional simulations to the predictions of the advection-diffusion model proposed in the last section. We consider particles of size $a_s = 1$ and $a_l = 1.41$ in a vessel with quadratic cross-section of size $36 \times 567 \times 36$ with walls at the bottom and top and periodic boundary conditions in the other directions. This setup is chosen to resemble a settling column where the walls are far apart from the center, so that their influence can be neglected.

In summary we use the following parameters for the simulations:

$\lambda = a_l/a_s$	1.414
$\phi_{l,s}$	0.05
L_x,L_y,L_z	36, 576, 36
$\rho_{l,s}$	2.5
g	30
Re	0.1

Due to the relatively small cross-section of the vessel of $36a_s \times 36a_s$ which corresponds to a cross-section of $25.5a_l \times 25.5a_l$ for the large particles we expect that the magnitude of the velocity fluctuations and accordingly of the diffusion coefficient will be less than measured in the experiments (cf. section 3.1) .

We find that a maximum of $D_i/a_i U_i^{(0)}$, $D_{\max} = 4.0 \pm 0.5$ shows the best agreement with the simulations. Nicolai et al. found a maximum value of $D_i/a_i U_i^{(0)} = 6.4 \pm 1.0$.

Figure 5.8 shows the predictions of the advection-diffusion model together with the data of the three dimensional simulations. The advection-diffusion model predicts concentration profiles for the small and the large particles in the range of small volume fractions very accurately. For higher concentrations $\phi > 0.3$ the agreement is not as good, but the general trend is captured. It seems that diffusion is too pronounced at higher concentrations, in accordance with the experimental data shown in Figure 5.6. The experimentally measured diffusion coefficient vanishes at $\phi = 0.4$ whereas the model function (5.13) becomes zero only at a volume fraction of $\phi = 0.68$. The vanishing of the diffusion coefficient at volume fractions smaller than $\phi = 0.68$ is also explicable from geometrical arguments. At a certain volume fraction the particles are so close to each other that the particles are not able to move independently, the particles are trapped. We therefore expect that the diffusion is strongly reduced, well before the maximum packing of particles is reached. Our model equation for the volume fraction dependency of the diffusion coefficient does not capture this detail.

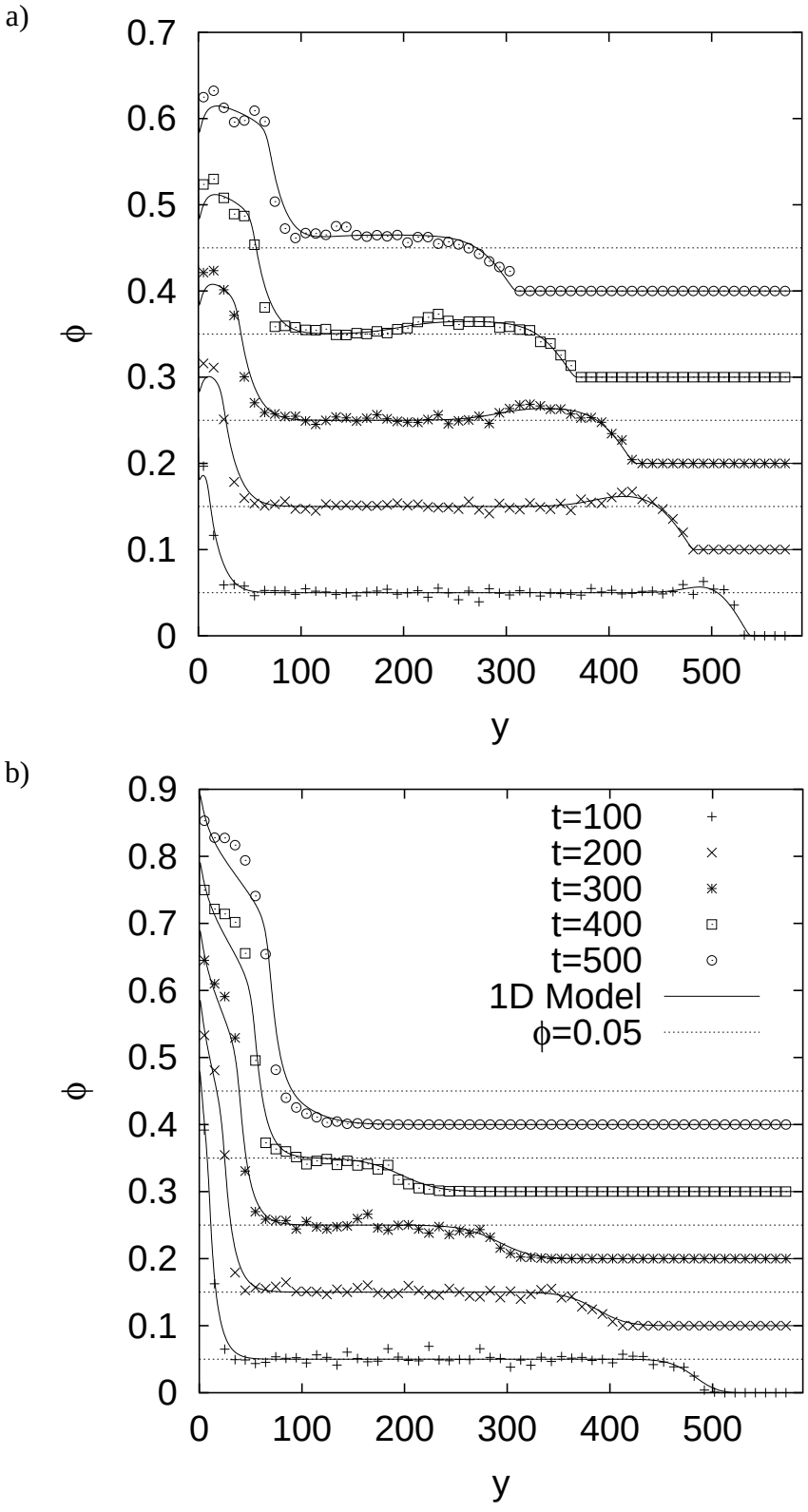

Figure 5.8: Volume fraction of the small particles (a) and the large particles (b). The solid lines show the predictions of the advection-diffusion model and the data points the measurements from 3 dimensional simulations. The values of the concentrations have been shifted by 0.1 for $t >$100. We also show the initial concentration $\phi = 0.05$ (dotted line).

5.2.2 Comparison with Experimental Results

In experimental measurements of polydisperse suspension only the total volume fraction of particles is accessible. We therefore compare our advection diffusion model with experiments which study the concentration profile of a monodisperse suspension of glass spheres in viscous fluid.

In general it is not easy to compare the theoretical predictions with experimental data, because the stationary concentration profile is normally not available from experiments. This is due to the fact that the particles used in experiments are never monodisperse. To be able to compare with experiments we therefore have to account for the polydispersity of the particles.

Lee, Jang, Choi and Lee [64] measured the broadening of the interface of a 'monodisperse', non-colloidal suspension by NMR computerized tomography. They used particles with a average radius of $68\mu m$ and a standard deviation of $4\mu m$. In Figure 2 of Ref. [64] they show the volume fraction as a function of the position for 332, 443, 567, 1288 and 2611 seconds which corresponds to 471, 628, 804, 1827 and 3703 Stokes times t_{St}.

We use Eq. (5.5) and (5.13) in the advection diffusion equation (5.7) to describe the concentration profiles by numerical integration of (5.7). The only free parameter is the scaling factor of the diffusion coefficient $D_{\max}$. All other parameters which enter the partial differential equation are given by the experimental setup. The concentration profile at $t = 471 t_{\mathrm{St}}$ can be well represented with $D_{\max} = 10$. But as we see in Figure 5.9 a value of $D_{\max} = 15$ would be needed to describe the concentration profile at $t = 804 t_{\mathrm{St}}$. The width of the profile grows faster than predicted by the advection diffusion equation.

This pronounced spreading of the profile is due to the polydispersity of the particles. As described in section 5.2 the width of the profile increases proportional to t because of the polydispersity of the suspension. To account for the polydispersity of the particle used in Lee's experiment, we represent the continuous distribution of particles sizes by N_S particle species with the same standard deviation. We use 5 particles species and weight them as shown in Figure 5.10 to resemble a Gaussian distribution of particle sizes. We also tried non-Gaussian distributions like a uniform distribution with the same variance, but we find that the differences in the results are marginal.

We find that for a particles distribution with $\sigma = 4$ the predictions of our model match the experimental data more closely than in the case of monodisperse particles, but the width of the experimental profile still increases faster than in our model. If we increased the width of our particle size distribution to $\sigma = 6$ the experimental results are reproduced to a large extent. In Figure 5.11 we show the experimental data of Lee *et al.* and our numerically calculated concentration profiles for different times.

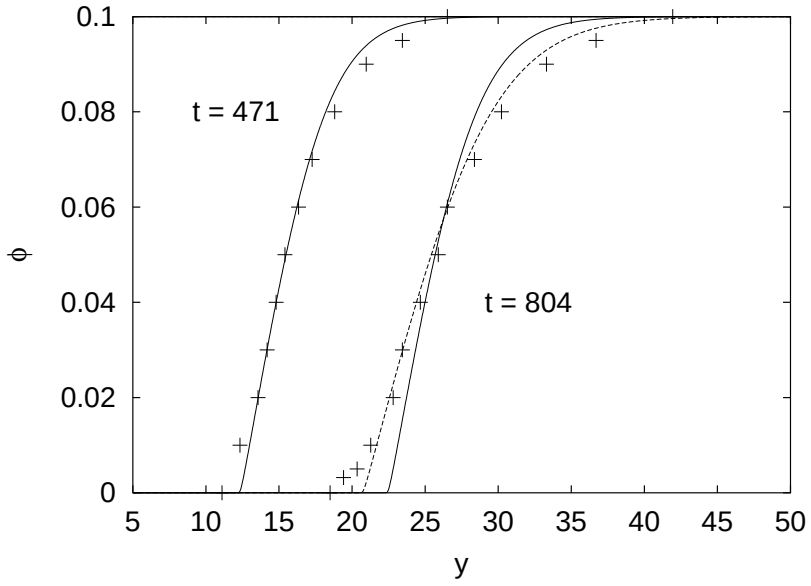

Figure 5.9: Measured concentration profile for $t = 471 t_{\mathrm{St}}$ and $804 t_{\mathrm{St}}$ (+) and predicted concentrations for a maximum value of the diffusion coefficient $D_{\max} = 10$ (solid line) and $D_{\max} = 15$ dashed line.

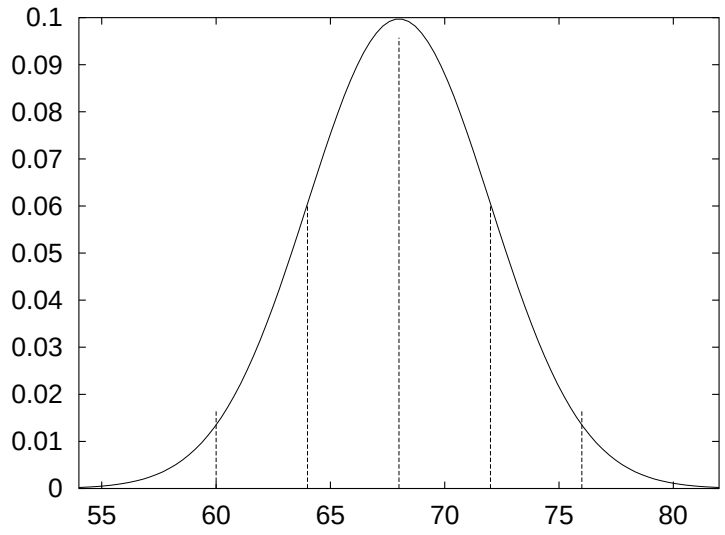

Figure 5.10: Approximation of a continuous Gaussian particle size distribution with $\sigma = 4$ by 5 particles species.

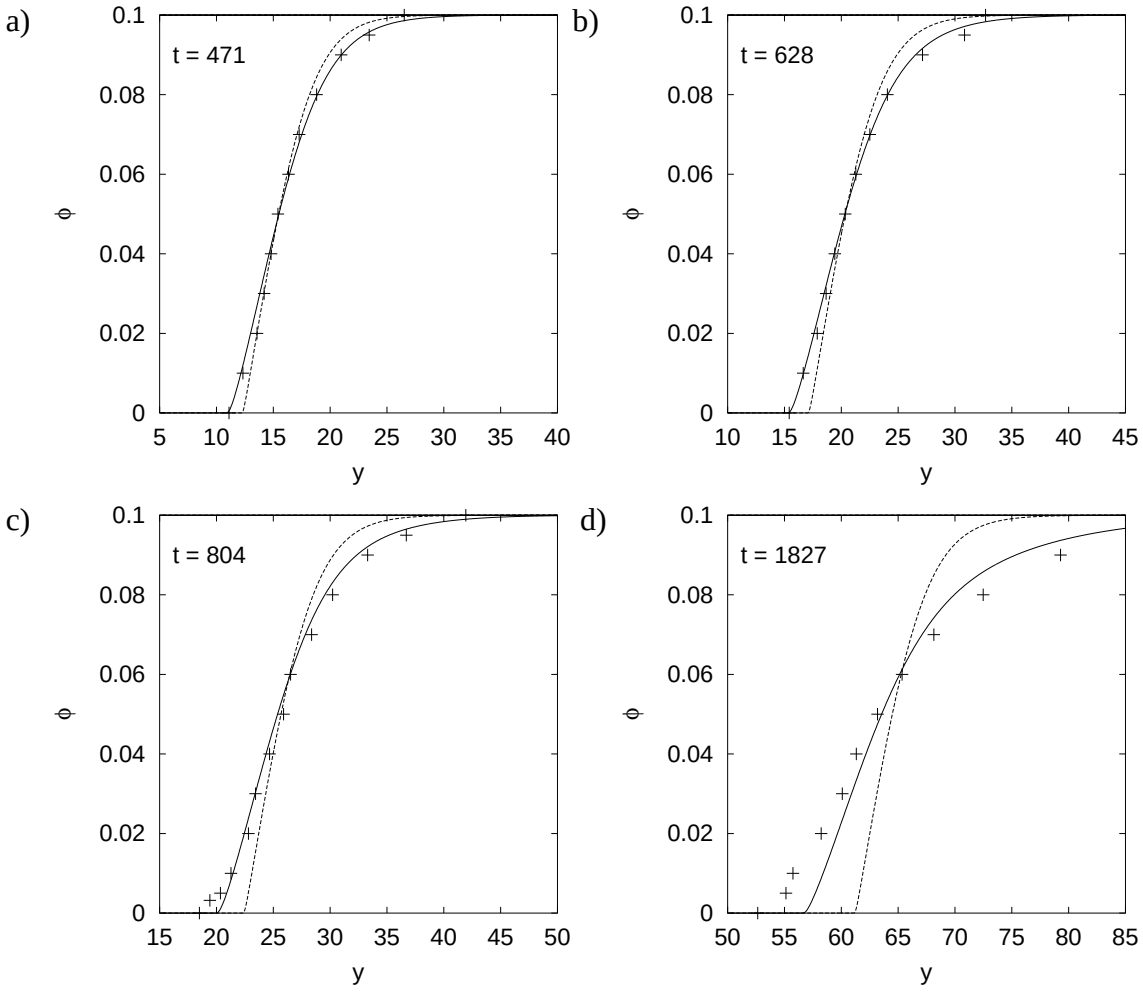

Figure 5.11: Concentration profiles measured by Lee *et al.* (+) and predictions of our model equation for monodisperse particles (dashed lines) and a distribution 5 particle sizes with $\sigma = 6$ (cf. Fig. 5.10) (solid lines). In both cases the maximum value of the diffusion coefficient was $D_{\max} = 10$.

Our study shows that a model which takes the polydispersity of the particles into account is able to yield much better results than a purely monodisperse description. It also shows that the polydispersity of the particles is often the main cause of the spreading of the interface even in seemingly monodisperse suspensions.

In Figure 5.12 we show how the suspension profile at (a) $t = 471 t_{\mathrm{St}}$ and (b) $t = 804 t_{\mathrm{St}}$ is composed from the 5 particle species, distributed like shown in Figure 5.10. The width of the transition zone for the total concentration increases due the different settling velocities of the 5 particle species. As shown in Figure 5.12 the concentration of the slower settling particles species (the particles of the particle size distribution with a radius smaller than average) increases at the top of the suspension due to the continuum equation (5.3). Additionally the width of the *interface* for the particle species larger than the average radius is much larger as for the smaller particle species.

We have shown in this chapter that it is possible to us polydisperse hindered settling functions in conjunction with concentration dependend diffusion coefficients to describe concentration profiles of mono- and polydisperse particle suspensions. Even though the time depended solutions of the resulting coupled partial differential equations are only accesible by numerical integration it provides valuable insight into the particle segregation and interface spreeding, and might even help to understand the composition of sediments.

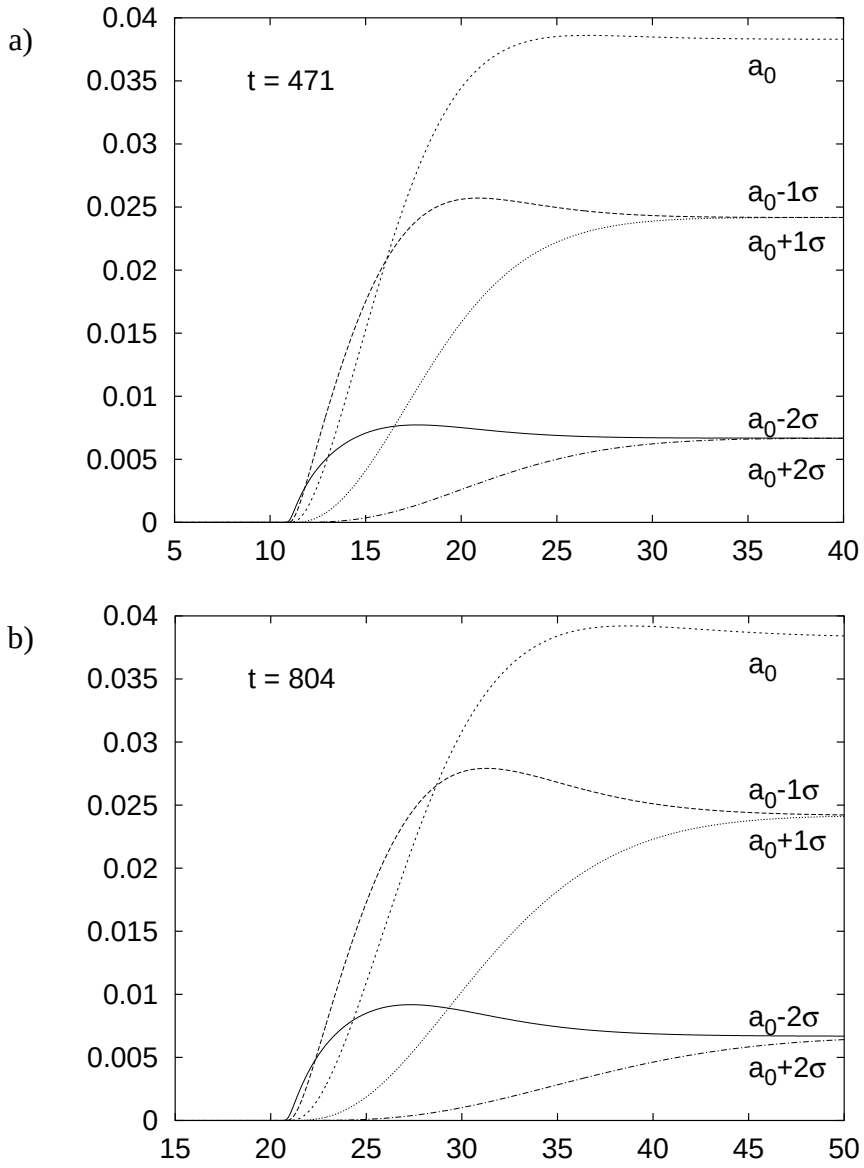

Figure 5.12: Concentration profiles at (a) $t = 471 t_{\mathrm{St}}$ and (b) $t = 804 t_{\mathrm{St}}$ for the different particle types with a discrete Gaussian size distribution ($\sigma = 6$) as shown in Figure 5.10.

Chapter 6

Conclusion

We have presented a numerical simulation technique which allows us to study three-dimensional, non-Brownian particle suspensions at low Reynolds numbers [47]. The program has been parallelized, so that we are able to simulate polydisperse suspensions with up to a few hundred thousand particles.

The simulation technique couples the particles and the fluid by means of constraint forces and has been verified on various test cases like fluid flow through a bed of fixed spheres and the calculation of the volume fraction dependency of the mean sedimentation velocity. We have shown that the simulation is suitable for suspensions up to a particle volume fraction of approximately 40%.

Monodisperse suspensions

The study of the velocity fluctuations of monodisperse suspensions has shown that the velocity fluctuations in systems with periodic boundary conditions diverge with the system size L. The increase of the velocity fluctuations is in agreement with the theoretical arguments of Hinch [43] and scales like $\sigma \sim L^{1/2}\phi^{\alpha}$ with $\alpha = 1/2$ with an error bar $\Delta\alpha = 1/6$.

In the case of monodisperse suspensions where the container is bounded by walls in the directions perpendicular to gravity no such scaling has been found. We have studied systems of size 250×250 and varied the depth from 25 to 200 at a volume fraction of $\phi = 0.05$. We have found that the smallest extension of the container controls the magnitude of the velocity fluctuations. If the smallest extension is increased, the velocity fluctuations increase up to a limit and are then independent of the container size.

We also found that the instantaneous velocity fluctuations increase very rapidly when the sedimentation process starts and reach a *steady state* after approximately $150t_{\mathrm{St}}$. After

that the width of the instantaneous velocity distribution still fluctuates significantly around its mean value on time scales of about $100t_{\mathrm{St}}$. The velocity fluctuations near the walls are reduced up to a distance of approximately $40a$ from the walls.

In accordance with the observations of Segrè [93] we also found that the relative particle velocities $\vec{U}-\langle\vec{U}\rangle$ show a swirl-like structure. The spatial correlation length perpendicular to gravity is $75a$ at $\phi = 0.05$ when the velocity fluctuations are independent of the system extensions.

Bidisperse suspensions

In simulations of suspensions with particles of two sizes we have verified predictions of Batchelor and Wen for the average settling velocities, if corrections due to the finite size of the simulation volume and the finite Reynolds number are applied to the measured data. The agreement of the predicted pair correlation functions with the measured data is not as good as for the velocities, indicating that three particle effects are present even at very low volume fracions without invalidating Batchelor's two-body approximation.

In case of particles with different densities the subtle changes of the settling velocities due to the different limits in the calculations of the sedimentation coefficients could not be found.

The velocity fluctuations in bidisperse suspensions have also been measured. On one hand the velocity fluctuations of the large particles first decrease and then increase as the size of the large particles is increased in a suspension of particles with different radii. On the other hand the velocity fluctuations of the more dense particles in a suspension with particles of different densities do increase similarly to the velocity fluctuations of the light particles. We found that the ratio of velocity fluctuations of small and large particles was about twice the experimental value reported by Peysson [80].

The measurement of the velocity fluctuations in bidisperse suspension for different sizes of the simulation volume could not be brought in accordance with the scaling behavior found for monodisperse suspensions with periodic boundary conditions.

Modeling of polydisperse suspensions

Based on Kynch's one-dimensional theory for the evolution of concentrations in monodisperse suspension [57], we formulated an extension for polydisperse suspensions. The choice of the flux function has been based on Batchelor's sedimentation coefficients [8], which reproduces the basic features of the results of three-dimensional simulations of batch sedimentation. The Kynch model did not show the broadening of the interfaces

between the different settling zones in the polydisperse suspension and lacks a correct description of the increase of small particle volume fraction in the zone of small particles only [14].

We have therefore extended the Kynch model to an advection-diffusion model, where the volume fraction dependency of the diffusion coefficient is described by the phenomenological expression

$$D_i(\Phi) = D_{\max} A \, a_i U_i^{(0)} \phi_i \left(\frac{U_i(\Phi)}{U_i^{(0)}} \right)^2 \tag{6.1}$$

which shows a good agreement with experimental data [75].

The system of coupled partial differential equations resembles the results of simulations to a high degree and allows to describe the experimental concentration profiles of monodisperse particle suspensions of a given size distribution.

6.1 Outlook

Using this simulation technique in connection with the parallelization of the particle-fluid interaction, it is now possible to efficiently simulate non-spherical particles, with a large aspect ratio or particle suspensions with particles of different sizes [56]. Future developments could aim in different directions.

- The study of non-spherical and especially elongated particle suspensions. The behavior of non-spherical particles at finite Reynolds number in a suspension is a particularly interesting problem, as the idealization of spherical particles is not often met in real suspensions. We expect interesting effects, as, e.g., clustering.

- As soon as the Reynolds number is increased above approximately 0.5 the analytical calculations based on the linear Stokes equations lose their validity. As our method uses the full Navier-Stokes equation to model the fluid, it includes the nonlinear effects, which come into play as the Reynolds number is increased. It is therefore possible to study how the properties of the suspensions change when the Reynolds number is varied.

- The most challenging is to find a description of particle suspensions which allows an up-scaling of particle scale simulations to system sizes of technological relevance. A consistent formulation on scales larger than the particle scale is required and the necessary phenomenological parameters can be determined from particle scale simulations. This would allow for the prediction of phenomena in large scale

applications from first principles and could therefore help to explore wide parameter ranges, which is not possible with classical phenomenological theories.

Appendix A

Technical Details

As we have seen in the section 2.5.1 the numerical method is still computationally expensive and it requires large resources on memory and CPU time to simulate particle laden flows with 10^5 and more particles. Due to the long-range, hydrodynamic interaction of the particles, systems with many particles have to be simulated over a long physical time. Such simulations are only possible on modern supercomputers, which implies either the vectorization or the parallelization of the algorithm. As the amount of computer memory needed increases linearly with the fluid grid points and the number of particles and the scalability of vector computers with regard to memory consumption is problematic, we decided not to vectorize the program but to parallelize the algorithm for the usage on massive parallel computers.

We chose the domain decomposition approach to port the algorithm to the parallel computer, because the interaction between the particles and the fluid are localized at the location of the particles and the inter particle forces are also short ranged. We used the Message Passing Interface (MPI), which is available on most computer platforms for the implementation of the communication. The program is integrated in and profits from the P3T C++ library that is being developed at the ICA 1 [45].

A.1 Parallelization of the Fluid

For a finite difference discretization of the Navier-Stokes equation (cf. Sec. 2.1) domain decomposition is a good choice for the parallelization strategy, because the data of only a fixed number of neighboring grid points is needed to update the information associated with a given grid point. We will sketch the parallelization principle for the two-dimensional case and appeal to the imagination of the reader for the generalization to three dimensions because the two-dimensional description is more comprehensive.

a)

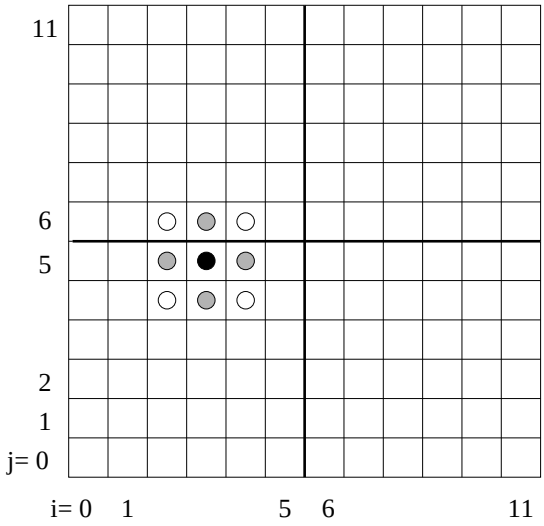

b)

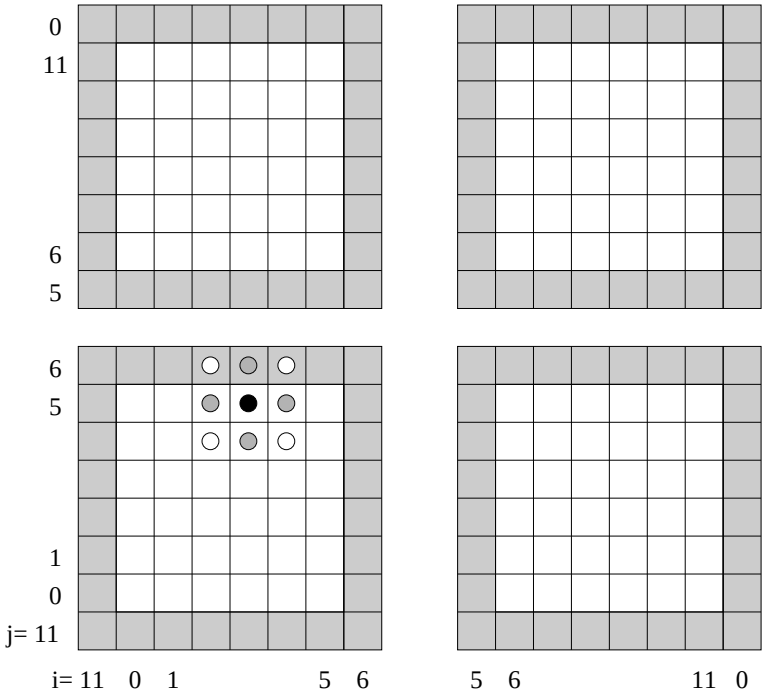

Figure A.1: Example of a two dimensional grid which is distributed across 4 PEs. The circles show the grid points needed to calculate the new value of the array at the location of the black circle. The shaded grid points are the shadow rows. They contain copies of the nonshaded grid points with the same index.

Figure A.1(a) shows an example of a two dimensional grid of size 12×12 with periodic boundary conditions. We want to distribute the computational domain onto 4 processing elements (PEs). The distributed array is shown in Figure A.1(b). In order to update any given grid point, for example the point marked with the black circle in Figure A.1 we require the values on the grid point itself and the $2d$ nearest neighbors (grey circles) to discretize the Poisson equation. Here d denotes the dimension of the discretization. To discretize the Navier-Stokes equation we also need the neighbors in the diagonal directions (white circles) due to the nonlinear part of the Navier-Stokes equation.

Thus we must copy the values on the boundary of a PE domain to that PE which contains the neighboring grid points, so that each PE can calculate the next time step independent of the other PEs. For example the lower left PE has to send the grid points with $i = 0$ and $i = 5$ to the upper left PE and the grid points with $j = 0$ and $j = 5$ to the lower right PE. As the ratio of the surface area to the volume scales like $1/L$ where L is the linear dimension, the additional work necessary for the communication will be less significant as the arrays get larger.

The Poisson equation (2.6) has to be solved in each time step. If we apply an iterative procedure like SOR to find the solution, the number of iterations needed would increase with the size of the array and make large scale simulations disproportionately expensive.

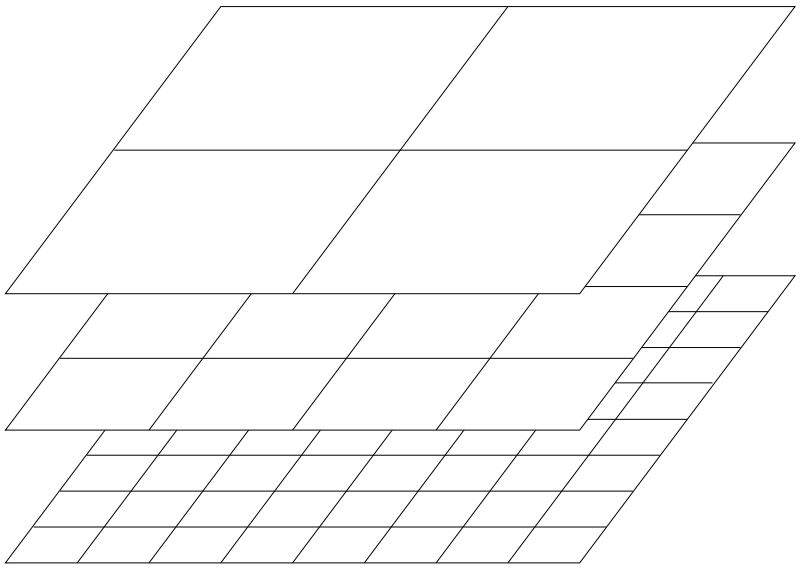

Figure A.2: Sketch of the series of grids used in the multigrid algorithm to solve the Poisson equation.

We therefore use a multigrid algorithm, which discretizes the Poisson equation on a series of grids with increasing mesh spacings (cf. Fig. A.2). On each grid only few iterations of e.g. the Gauss-Seidel relaxation method are needed to smooth the hight frequency

part of the error on that discretization level. Thus the multigrid algorithm overcomes the principal scaling problem and the effort is proportional to the number of grid points [35, 106]. The problem is now that the multigrid algorithm uses a sequence of arrays where the mesh size h is doubled from grid to grid as sketched in Figure A.2. Due to the coarsening of the grids the number of grid points decreases by a factor of $1/2d$. Therefore the boundaries, which must be communicated play a important role as the ratio of surface to volume increases. Thus the latency associated with each communication will result in a reduced parallel efficiency of the coarse grid.

The effect of the communication latency is also visible if we measure the parallel efficiency η of a Gauss-Seidel relaxation. The parallel efficiency is defined by

$$\eta = \frac{T_1}{T_N}, \tag{A.1}$$

where T_1 is the time needed to iterate a field of size L^3 on one PE and T_N the time to iterate a field of size $N\ L^3$ on N PEs. As we see in Figure A.3, latency causes a deviation from the expected $\eta = 1 - c/L$ dependency for small values of L. Here c is a constant depending on the ratio of time spend updating the boundary points (so called shadow points) and calculating the grid points in the volume.

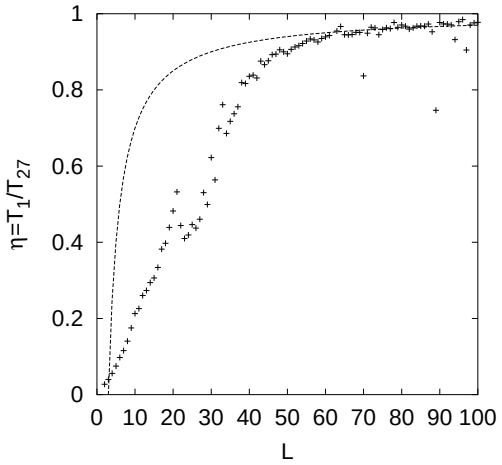

Figure A.3: Parallel efficiency of a parallel Gauss-Seidel iteration on 27 PEs. The size of the field is L^3 on one and $(3L)^3$ on 27 PEs respectively. The solid line is the idealized behavior $\eta = 1 - c/L$ without communication latency.

The usage of a multigrid algorithm for the Poisson equation results in a decrease of the parallel efficiency of the Navier-Stokes solver from $\approx 90\%$ to $\approx 70\%$ for a fluid field with $L = 64$. It is still much faster than an iterative method, due to its superior convergence properties [35].

A.2 Parallelization of the Particles

The particles in our simulation consist of the particle itself and the tracers which are associated to the reference positions on the particles (cf. Sec. 2.1.2). The particles and the tracers move continuously in space. If we decompose our computational domain in the same way as for the fluid, the computation of the interaction between the particles and the fluid does not require inter-processor communications.

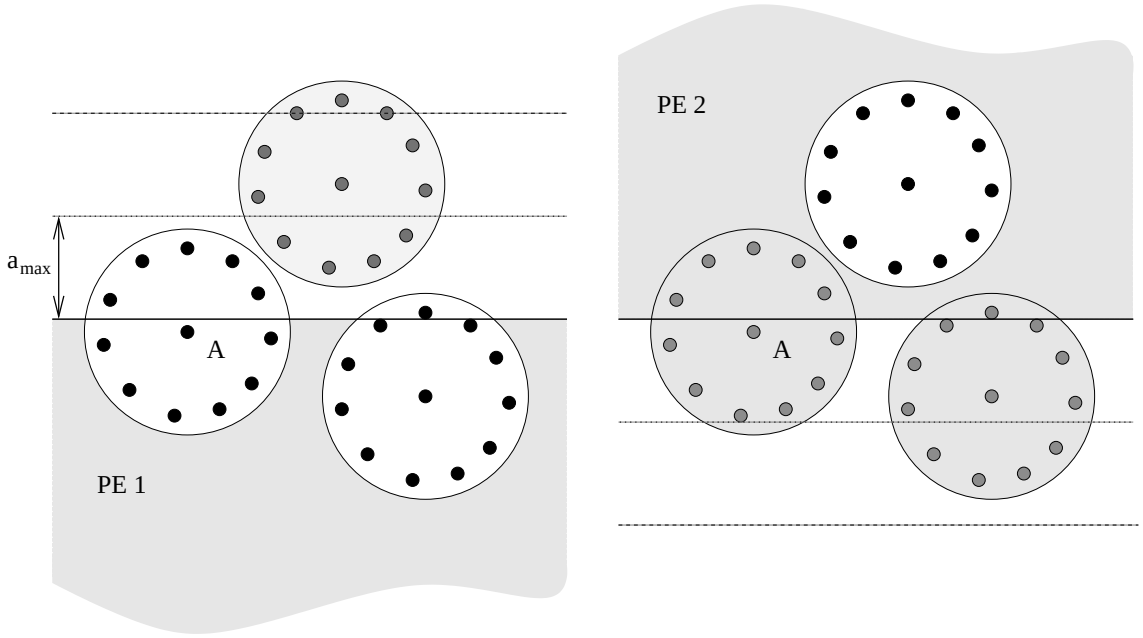

Figure A.4: Conventional approach to parallelize the particles and tracers. Particles near the boundary are shown for PE 1 on the left and for PE 2 on the right. The greyed particles are shadow particles, i.e. copies of the particles located the other PE. The tracers are stored with the particles on the same PE. The dashed line shows the interaction radius of particles, i.e. all particles, whose center lie within the boundary and the dashed line must be communicated. In the area of width $a_{\max}$ between the boundary and the dotted line the values of the fluid velocities have to be known, i.e. they must be stored in shadow rows.

If a particle (e.g particle A in Fig. A.4) is located within a distance smaller than the particle radius from the physical boundary of the computational domain, parts of the particle and therefore parts of the tracers will be located outside the computational domain. This implies that we need the fluid grid values from the neighboring PE to calculate the movement of the tracers and the forces on the particle (area between solid and dotted line in Fig. A.4). Thus we must communicate $N_{sh} = a_{\max}/h$ shadow rows from the neighboring PE to calculate the force on the particle and to integrate the tracers, where $a_{\max}$ is the

maximum particle radius. In addition the neighboring PE needs the particle and tracer positions to calculate the force on the fluid (greyed particle A on PE 2).

If this approach is utilized we must communicate N_{sh} rows of fluid velocity grid points and all the particles including the associated tracers that lie within a particle radius from the physical domain boundary [104]. Therefore large amounts of data must be communicated, especially when the mesh size h becomes small compared to the particle radius or when the particles are nonspherical, as, e.g., fiber-like particles.

To overcome this problem we split the calculation of the force from the fluid on a particle so that each PE calculates the part of the force originating from the fluid located on the PE. Additionally we store the tracers separately from the particles. This allows that tracers migrate independent of the particles from one PE to the other as as soon as they cross the boundary between the PEs. The situation shown in Figure A.4 then changes to the one shown in Figure A.5.

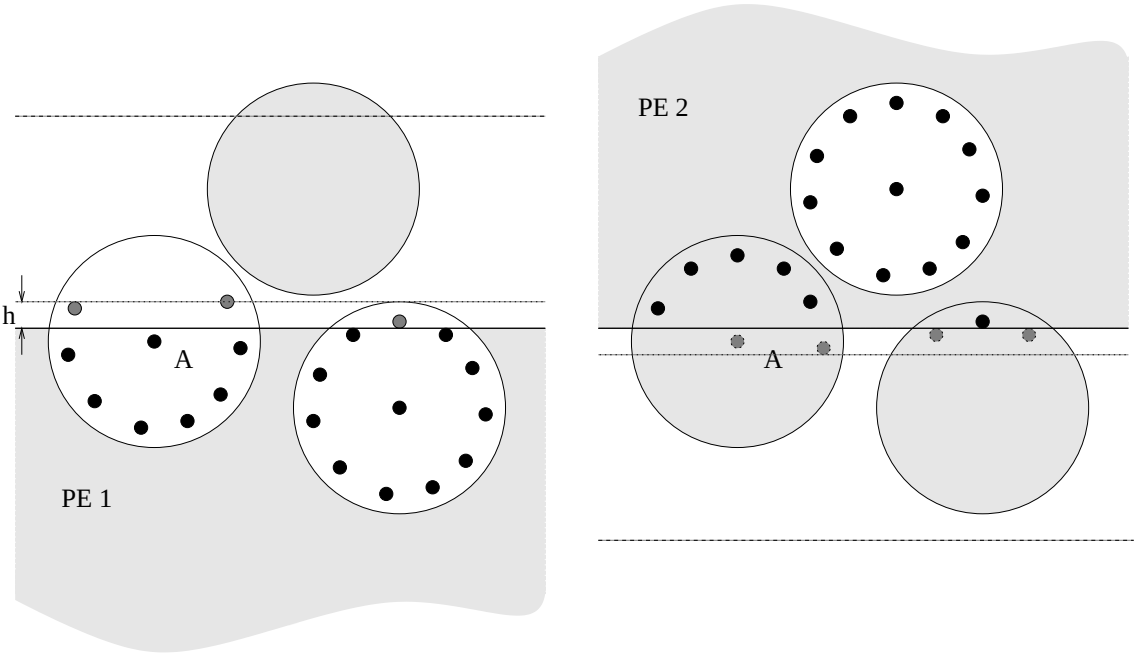

Figure A.5: Parallelization approach for the particles and the tracers used in the simulations. Traces and particles migrate independent from each other from one PE to the other. The particles and tracers that are copies from particles and tracers from another PE are drawn in grey.

PE 1 now only contains parts of the tracers associated with particle A and calculates only that part of the force acting on the particle and on the fluid which originates from this tracers. The rest of the tracers are located on PE 2. The forces on the particle calculated on PE 2 are stored in the shadow particle and after the calculation of all forces communicated

back to the PE where the particle is located (PE 1 in this case). Therefore the amount of data which has to be communicated is reduced significantly. The two tracers of particle A shown in grey on PE 1 are copies of the tracers located on PE 2 and are necessary to calculate the force on the fluid at the boundary grid points.

In summary we have to store the following (shadow) data from the neighboring PEs to calculate a time step:

- 1 shadow row of the fluid velocities to integrate the tracer movement,
- particles which are within $2a_{\max}$ of the boundary (dashed line in Figure A.5),
- tracers which are within h of the boundary (dotted line in Figure A.5).

We do not want to conceal that the advantage of less communication has to be paid by additional computations and storage requirements for the particles. Due to the fact that the particles and tracers are stored separately each particle must be identified uniquely and each tracer has to store this information in order to know with which particle it is associated. In addition we need to find the corresponding particle before we can calculate the force on the particle and on the fluid. Thus we use an associative map to minimize the time spent to find the particles. Additional complexity is added due to the fact that a particle might be present on up to 2^d PEs in d dimensions if it is located in the corner of the computational domain.

A.3 Parallel performance

Due to the optimizations described in the previous section, the parallel efficiency of the algorithm described is almost independent of the geometry of the particles and the relative size of the particles with regard to the fluid discretization. Due to the fact that the parallelization of the particles is more efficient than that of the fluid, the parallel efficiency increases slightly with higher particle concentrations.

The implementation of the multigrid algorithm does not allow for arbitrary sizes of the fluid field. We therefore do not measure the parallel efficiency but a parallel scaleup, i.e. we calculate a simulation of a given size on one PE and than increase the size of the problem and accordingly the number of PEs. Therefore a ideal scaleup would result in the situation that all simulations take the same time. In Figure A.6 we show

$$\eta(N) = \frac{T_1}{T_N}, \tag{A.2}$$

where N is the number of PEs and T_N is the time needed for the simulation on N PEs. The scaleup of the parallel efficiency is shown for three different system sizes: A system with a fluid grid size of 32^3N (+), 64^3N ($\times$), and 128^3N (*) at a volume fraction of $\phi = 0.2$ and a mesh size $h = 0.375$.

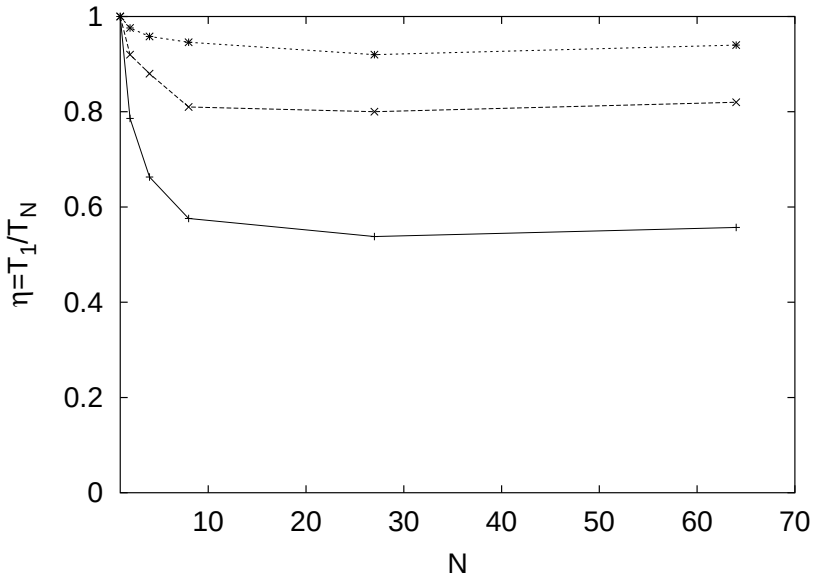

Figure A.6: Scaleup of the parallel efficiency. We show η as a function of the number of PEs N for three different system sizes (+) 32^3N, ($\times$) 64^3N, and (*)128^3N.

In addition we show $N\eta$ in Figure A.7.The value $N\eta$ corresponds to the number of time steps done in a fixed time as a function of the number of PEs.

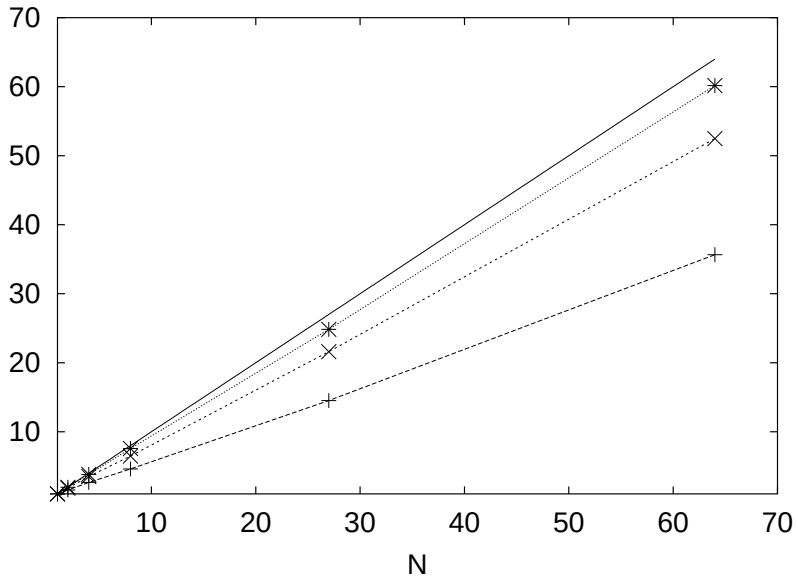

Figure A.7: Scaleup of the parallel efficiency. We shown $N\eta$ as a function of the number of PEs N for three different system sizes (+) $N32^3$, ($\times$) $N64^3$, and (*)$N128^3$. The solid line is the limit of a ideal scaleup.

Bibliography

[1] Andreas Acrivos and Eric Herbolzheimer. Enhanced sedimentation in settling tanks with inclined walls. *J. Fluid Mech.*, 92(3):435–457, 1979.

[2] F. J. Alexander, S. Chen, and J. D. Sterling. Lattice Boltzmann thermohydrodynamics. *Phys. Rev. E*, 47(4):R2249–R2252, 1993.

[3] M. P. Allen and D. J. Tildesley. *Computer Simulation of Liquids*. Clarendon Press, Oxford, 1987.

[4] G. K. Batchelor. Sedimentation in a dilute dispersion of spheres. *J. Fluid Mech.*, 52:245, 1972.

[5] G. K. Batchelor. Brownian diffusion of particles with hydrodynamic interaction. 74:1–29, 1976.

[6] G. K. Batchelor. Sedimentation in a dilute polydisperse system of interacting spheres. Part 1. General theory. *J. Fluid Mech.*, 119:379–408, 1982.

[7] G. K. Batchelor and J. T. Green. The hydrodynamic interaction of two small freely-moving spheres in a linear flow field. *J. Fluid Mech.*, 56:375–400, 1972.

[8] G. K. Batchelor and C.-S. Wen. Sedimentation in a dilute polydisperse system of interacting spheres. Part 2. Numerical results. *J. Fluid Mech.*, 124:495–528, 1982.

[9] E.S. Boek, P.V. Coveney, and P. van der Schoot H.N.W. Lekkerkerker. Simulating the rheology of dense colloidal suspensions using dissipative particle dynamics. *Phys. Rev. E*, 55(3):3124–3133, 1997.

[10] G. Bossis and J. F. Brady. The rheology of brownian suspensions. *J. Chem. Phys.*, 91(3):1866–1874, 1989.

[11] James D. Bozeman and Charles Dalton. Numerical study of viscous flow in a cavity. *Journal of Comp. Phys.*, 12:348–363, 1973.

[12] John F. Brady and Georges Bossis. Stokesian dynamics. *Ann. Rev. Fluid Mech.*, 20:111–157, 1988.

[13] John F. Brady and Louis J. Durlofsky. The sedimentation rate of disordered suspension. *Phys. Fluids*, 31(4):717–727, 1988.

[14] R. Bürger, K.-K. Fjelde, K. Höfler, and K. Hvistendahl Karlsen. Central difference solutions of the kinematic model of settling of polydisperse suspensions and three-dimensional particle-scale simulations. *Journal of Engineering Mathematics*, submitted, 2000.

[15] R. Bürger, W. L. Wendland, and F. Concha. Modelling equations for gravitational sedimentation-consolidation processes. *Z. Angew. Math. Mech.*, 80:79–92, 2000.

[16] B. L. Buzbee, F. W. Dorr, J. A George, and G. H. Golub. The direct solution of the discrete Poisson equation on irregular regions. *SIAM J. Numer. Anal.*, 8:722–736, 1971.

[17] Russel E. Caflisch and Jonathan H. C. Luke. Variance in the sedimentation speed of a suspension. *Phys. Fluids*, 28(3):759–760, 1985.

[18] R. H. Davis and K. H. Birdsell. Hindered settling of semidilute monodisperse and polydisperse suspensions. *AIChE Journal*, 34(1):123–129, 1988.

[19] R. H. Davis and M. A. Hassen. Spreading of the interface at the top of a slightly polydisperse sedimenting suspension. *J. Fluid Mech.*, 196:107, 1988.

[20] Robert H. Davis. Interaction of two suspended particles. In E. Guazzelli and L. Oger, editors, *Mobile Particulate Systems*, Dordrecht, 1995. Kluwer Academic Publishers. [Proceedings of the Summer School on Mobile Particulate Systems, Cargese, Corsica, July 1994].

[21] Robert H. Davis and Hatice Gecol. Hindered settling function with no empirical parameters for polydisperse suspensions. *AIChE Journal*, 40(3):570–575, 1994.

[22] J. Feng, H. H. Hu, and D. D. Joseph. Direct simulation of initial value problems for the motion of solid bodies in a newtonian fluid. Part 1. Sedimentation. *J. Fluid Mech.*, 261:95, 1994.

[23] O. Filippova and D. Hänel. Grid refinement for lattice-bgk models. *J. Comp. Phys.*, 147(1):219–228, 1998.

[24] E. G. Flekkøy and D. H. Rothman. Fluctuating hydrodynamic interfaces: theory and simulation. *Phys. Rev. E*, 53(2):1622–1643, 1966.

[25] Aaron L. Fogelson and Charles S. Peskin. A fast numerical method for solving the three-dimensional Stokes equation in the presence of suspended particles. *Journal of Comp. Phys.*, 79:50–69, 1988.

[26] M Fortin, R. Peyret, and R. Temam. *J. Méc.*, 10:357–390, 1971.

[27] Dimitri Gidaspow. *Multiphase Flow and Fluidization*. Academic Press, San Diego, 1994.

[28] R. Glowinski, T. W. Pan, T. I. Hesla, and D. D. Joseph. A distributed Lagrange multiplier/fictitious domain method for particulate flow. *Int. J. Multiphase Flow*, 25:755–794, 1999.

[29] R. Glowinski, T. W. Pan, T. I. Hesla, D. D. Joseph, and J. Périaux. A distributed Lagrange multiplier/fictitious domain method for particulate flows around moving rigid bodies. *Int. J. Numer. Meth. Fluids*, 30:1043–1066, 1999.

[30] Roland Glowinski, Tsorng-Whay Pan, and Jacques Périaux. A fictitious domain method for external incompressible viscous flow modeled by navier-stokes equations. *Comput. Methods Appl. Mech. Engrg.*, 112:133–148, 1994.

[31] A. J. Goldman, R. G. Cox, and H. Brenner. Slow viscous motion of a sphere parallel to a plane wall — I Motion through a quiescent fluid. *Chem. Eng. Sci.*, 22:637–651, 1967.

[32] N.T. Gray and K. Hutter. Physik granularer lawinen. *Phys. Bl.*, 54(1):37–43, 1998.

[33] Elisabeth Guazzelli and Luc Oger, editors. *Mobile Particulate Systems*. Kluwer Academic, Dordrecht, 1995. [Proc. NATO ASI, Cargèse, July 4–15, 1994].

[34] J. J. Haan and P. S. Steif. Particle-phase pressure in a slow shearing flow based on the numerical simulation of a planar suspension of rough contacting cylinders. *J. Rheol.*, 42(4), 1998.

[35] Wolfgang Hackbusch. *Multi-Grid Methods and Applications*. Springer, Heidelberg, New York, 1985.

[36] J. M. Ham and G. M. Homsy. Hindered settling and hydrodynamic dispersion in quiescent sedimenting suspensions. *Int. J. Multiphase Flow*, 14(5):533–546, 1988.

[37] Jean Pierre Hansen and Ian R. McDonald. *Theory of Simple Liquids*. Academic Press, London, 2nd edition, 1986.

[38] J. Happel. Viscous flow in multiparticles systems: Slow motion of fluids relative to beds of spherical particles. *A.I.Ch.E. Journal*, 4:197, 1958.

[39] John Happel and Howard Brenner. *Low Reynolds Number Hydrodynamics*. Prentice Hall, Englewood Cliffs, New Jersey, 1965.

[40] Stewart Harris. *An Introduction to the Theory of the Boltzmann Equation*. Holt, Rinehart, Winston, New York, 1971.

[41] H. Hasimoto. On the periodic fundamental solutions of the stokes equations and their application to viscous flow past a cubic array of spheres. *J. Fluid Mech.*, 5:317–328, 1959.

[42] E. J. Hinch. An averaged-equation approach to particle interactions in a fluid suspension. *J. Fluid Mech.*, 83:698–720, 1977.

[43] E. J. Hinch. Sedimentation of small particles. In E. Guyon, J.-P. Nadal, and Y. Pomeau, editors, *Disorder and Mixing*, page 153. Kluwer Academic, Dordrecht, 1988.

[44] D. Hirshfeld and D.C. Rapaport. Molecular dynamics simulation of Taylor-Couette vortex formation. *Phys. Rev. Lett.*, 80:5337–5340, 1998.

[45] K. Höfler, M. Müller, and S. Schwarzer. Design and application of object oriented parallel data structures in particle and continuous system. In E. Krause and W. Jäger, editors, *High Performance Computing in Science and Engineering '99*. Springer, Berlin, 1999.

[46] Kai Höfler. Räumliche Simulation von Zweiphasenflüssen. Master's thesis, Universität Stuttgart, 1997.

[47] Kai Höfler, Esa Kuusela, Christian Manwart, Reinmar Mück, and Stefan Schwarzer. Container size dependence of the velocity fluctuations in suspensions of monodisperse spheres. Technical report, to appear in High Performance Computing in Science and Engineering 2000, 2000.

[48] Kai Höfler and Stefan Schwarzer. Navier-Stokes simulation with constraint forces: Finite-difference method for particle-laden flows and complex geometries. *Phys. Rev. E*, 61(6):7146–7160, 2000.

[49] H. H. Hu. Direct simulation of flows of solid–liquid mixtures. *Int. J. Multiphase Flow*, 22(2):335–352, 1996.

[50] D. J. Jeffrey and Y. Onishi. Calculation of the resistance and mobility functions of two unequal rigid spheres in low-Reynolds-number flow. *J. Fluid Mech.*, 139:261–290, 1984.

[51] A. A. Johnson and T. E. Tezduyar. Simulation of multiple spheres falling in a liquid-filled tube. *Comput. Methods Appl. Mech. Engrg.*, 134:351–373, 1996.

[52] W. Kalthoff, S. Schwarzer, G. Ristow, and H. Herrmann. On the application of a novel algorithm to hydrodynamic diffusion and velocity fluctuations in sedimenting systems. *Int. J. Mod. Phys. C*, 7(4):543–561, 1996.

[53] Wolfgang Kalthoff, Stefan Schwarzer, and Hans Herrmann. An algorithm for the simulation of particulate suspensions with inertia effects. *Phys. Rev. E*, 56(2):2234–2242, 1997.

[54] Donald L. Koch and Anthony J. C. Ladd. Moderate reynolds number flows through periodic and random arrangements of aligned cylinders. *J. Fluid Mech.*, 349:31–66, 1997.

[55] Donald L. Koch and E. S. G. Shaqfeh. Screening in sedimenting suspensions. *J. Fluid Mech.*, 224:275–303, 1991.

[56] Esa Kuusela, Kai Höfler, and Stefan Schwarzer. Simulation of setttling speed and orientational distribution in suspensions of prolate spheroids. *Journal of Engineering Mathematics*, submitted, 2000.

[57] G. J. Kynch. A theory of sedimentation. *Trans. Farad. Soc.*, 48:166–176, 1952.

[58] Anthony J. C. Ladd. Hydrodynamic interactions in a suspension of spherical particles. *J. Chem. Phys.*, 88(8):5051–5063, 1988.

[59] Anthony J. C. Ladd. Short-time motion of colloidal particles: Numerical simulation via a fluctuating lattice-Boltzmann equation. *Phys. Rev. Lett.*, 70(9):1339–1342, 1993.

[60] Anthony J. C. Ladd. Numerical simulations of particulate suspensions via a discretized Boltzmann equation. Part 1. Theoretical foundation. *J. Fluid Mech.*, 271:285–309, 1994.

[61] Anthony J. C. Ladd. Numerical simulations of particulate suspensions via a discretized Boltzmann equation. Part 2. numerical results. *J. Fluid Mech.*, 271:311–339, 1994.

[62] Anthony J. C. Ladd. Sedimentation of homogeneous suspensions of non-brownian spheres. *Phys. Fluids*, 9(3):491–499, 1997.

[63] L. D. Landau and E. M. Lifschitz. *Hydrodynamik*, volume 6 of *Lehrbuch der Theoretischen Physik*. Akademie-Verlag, Berlin, 5th edition, 1991.

[64] S. Lee, Y. Jang, C. Choi, and T. Lee. Combined effect of sedimentation velocity fluctuation and self-sharpening on interface broadening. *Phys. Fluids A*, 4(12):2601–2606, 1992.

[65] M. J. Lockett and H. M. Al-Habbooby. Differential settling by size of two particle species in a liquid. *Trans. Inst. Chem. Eng.*, 51:281, 1973.

[66] M. J. Lockett and K. S. Bassoon. Sedimentation of binary particle mixtures. *Powder Technology*, 24:1–7, 1979.

[67] J. Martin, N. Rakotomalala, and D. Salin. Hydrodynamic dispersion broadening of a sedimentation front. *Phys. Fluids*, 6(10):3215–3217, 1994.

[68] Jacob H. Masliyah. Hindered settling in a multi-species particle system. *Chem. Eng. Sci.*, 34:1166–1168, 1979.

[69] B. Maury. Direct simulations of 2d fluid-particle flows in biperiodic domains. *J. Comp. Phys.*, 156(2):325–351, 1999.

[70] P. Mazur and W. van Saarloos. Many-sphere hydrodynamic interactions and mobility in a suspension. *Physica A*, 115:21–57, 1982.

[71] C. C. Mei and J.-L. Auriault. The effect of weak inertia on flow through a porous medium. *J. Fluid Mech.*, 222:647, 1991.

[72] J. R. Melrose, J. H. van Vliet, and R. C. Ball. Continuous shear thickening and colloid surfaces. *Phys. Rev. Lett.*, 77(22):4660–4663, 1996.

[73] P. Mills and P. Snabre. Settling of a suspension of hard spheres. *Europhysics Letters*, 25(9):651–656, 1994.

[74] S. Mirza and J. F. Richardson. Sedimentation of suspensions of particles of two or more sizes. *Chem. Eng. Sci.*, 34:447–454, 1979.

[75] H. Nicolai, B. Herzhaft, E. J. Hinch, L. Oger, and E. Guazzelli. Particle velocity fluctuations and hydrodynamic self-diffusion of sedimenting non-brownian spheres. *Phys. Fluids*, 7(1):12–23, 1995.

[76] Hélène Nicolai and Elisabeth Guazzelli. Effect of the vessel size on the hydrodynamic diffusion of sedimenting spheres. *Phys. Fluids*, 7(1):3–5, 1995.

[77] V. S. Patwardhan and Chi Tien. Sedimentation and liquid fluidization of solid particles of different sizes and densities. *Chem. Eng. Sci.*, 7:1051–1060, 1985.

[78] Roger Peyret and Thomas D. Taylor. *Computational Methods for Fluid Flow*. Springer Series in Computational Physics. Springer, Berlin, 1983.

[79] Yannick Peysson. *Convection intrinsèque et fluctuation vitesse en sédimentation*. PhD thesis, Univerity of Paris VI, 1998.

[80] Yannick Peysson and Élisabeth Guazzelli. Velocity fluctuations in a bidisperse sedimenting suspension. *Physics of Fluids*, 11(7):1953–1955, 1999.

[81] Thorsten Pöschel and Volker Buchholtz. Static friction phenomena in granular materials: Coulomb law versus particle geometry. *Phys. Rev. Lett.*, 71(24):3963–3966, 1993.

[82] William H. Press, Brian P. Flannery, Saul A. Teukolsky, and William T. Vetterling. *Numerical Recipes in C*. Cambridge University Press, Cambridge, 2nd edition, 1992.

[83] I. Proudman and J.R.A. Pearson. Expansion at small Reynolds numbers for the flow past a sphere and a circular cylinder. *J. Fluid Mech.*, 2:237, 1957.

[84] Harald Puhl. *Eine Studie zur Simulation granularer Medien*. PhD thesis, University of Stuttgart, 1997.

[85] K. Pye and H. Tsoar. *Aeolian Sand and Sand Dunes*. Unwin Hyman, London, 1990.

[86] J. F. Richardson and W. N. Zaki. Sedimentation and fluidisation: Part 1. *Trans. Instn Chem. Engrs.*, 32:35–53, 1954.

[87] Gerald H. Ristow. Wall correction factor for sinking cylinders in fluids. *Phys. Rev. E*, 55(3):2808–2813, 1996.

[88] A. Sangani and Guobiao Mo. Inclusion of lubrication forces in dynamic simulations. *Phys. Fluids*, 6(5):1653–1662, 1994.

[89] A.S. Sangani and A. Acrivos. Slow flow past periodic arrays of cylinders with application to heat transfer. *Int. J. Multiphase Flow*, 8(3):193–206, 1982.

[90] Hans Rudolf Schwarz. *Numerische Mathematik*. B. G. Teubner, Stuttgart, Germany, 1986.

[91] Stefan Schwarzer. Sedimentation and flow through porous media: Simulating dynamically coupled discrete and continuum phases. *Phys. Rev. E*, 52(6):6461–6475, 1995.

[92] Stefan Schwarzer, Wolfgang Kalthoff, Bernd Wachmann, and Hans H errmann. Bulk and interface dispersion of suspensions in the inertial regime. In D. Wolf and P. Grassberger, editors, *Friction, Arching, Contact Dynamics*, Singapore, 1997. World Scientific.

[93] P. N. Segrè, E. Herbolzheimer, and P. M. Chaikin. Long-range correlations in sedimentation. *Phys. Rev. Lett.*, 79(13):2574–2577, 1997.

[94] T. N. Smith. The differential sedimentation of particles of two diefferent species. *Trans. Instn Chem. Engrs.*, 43:T69–T73, 1965.

[95] T. N. Smith. The sedimentation of particles having a dispersion of sizes. *Trans. Instn Chem. Engrs.*, 44:T153–T157, 1966.

[96] M. Sommerfeld and H.-H. Qiu. Detailed measurements in a swirling particulate two-phase flow by a phase-Doppler aneometer. *Int. J. Heat and Fluid Flow*, 12(1):20–27, 1991.

[97] S. L. Soo. *Particles and Continuum: Multiphase Fluid Dynamics*. Hemisphere Publishing Corporation, New York, Washington, Philadelphia, London, 1989.

[98] John Stockie. *Analysis and Computation of Immersed Boundaries with Application to Pulp Fibres*. PhD thesis, University of British Columbia, September 1997.

[99] Toshitsugu Tanaka, Toshihiro Kawaguchi, Shota Nishi, and Yutaka Tsuji. Numerical simulation of two-dimensional fluidized beds: Effect of partition walls. *ASME/FED*, 166:17–22, 1993.

[100] E.M. Tory, M.T. Kamel, and C.F. Chan Man Fong. Sedimentation is container-size dependent. *Powder Tech.*, 73:219–238, 1992.

[101] D. J. Tritton. *Physical Fluid Dynamics*. Oxford University Press, 1988.

[102] Y. Tsuji, T. Tanaka, and T. Ishida. Lagrangian numerical simulation of plug flow of cohesionless particles in a horizontal pipe. *Powder Technology*, 71:239–250, 1992.

[103] B. Wachmann, W. Kalthoff, S. Schwarzer, and H.J Herrmann. Collective drag and sedimentation: Comparison of simulation and experiment in two and three dimensions. *Granular Matter*, 1(2):75–82, 1998.

[104] Bernd Wachmann and Stefan Schwarzer. Three-dimensional massively parallel computing of suspensions. *Int. J. Mod. Phys. C*, 9(5):759–775, 1998.

[105] W. L. Wendland and J. Zhu. The boundary element method for three-dimensional Stokes flows exterior to an open surface. *Mathematical and Computer Modelling*, 15:19–42, 1991.

[106] Pieter Wesseling. *An Introduction to Multigrid Methods*. John Wiley & Sons, Chichester, 1992.

[107] Shigeru Yonemura, Toshitsugu Tanaka, and Yutaka Tsuji. Cluster formation in gas-solid flow predicted by the DSMC method. *ASME/FED*, 166:303–309, 1993.

Acknowledgment

At the end of my thesis I would like to thank all those people who made this thesis possible and an enjoyable experience for me.

First of all I wish to express my sincere gratitude to Stefan Schwarzer, who guided this work and helped whenever I was in need. I think his presence at the ICA 1 was the best thing that could happen to me and my thesis.

I am also indebted to Hans Herrmann for the opportunity to work at the ICA 1.

I am grateful to the members of the institute for their support and their comradeship; especially to Christan Manwart, Reinmar Mück, Marc Lätzel, Matthias Müller and Gerd Sauermann.

I acknowledge the financial support by the Deutsche Forschungsgemeinschaft, Sonderforschungsbereich 404 and the access to the computer resources at the research center Jülich and the federal computer-center HWW in Stuttgart.

Finally, I would like to express my deepest gratitude for the constant support, understanding and love that I received from my wife Gabi and my parents during the past years.

Simulation und Modellierung von mono- und bidispersen Suspensionen

Deutsche Zusammenfassung der Doktorarbeit von

Kai Höfler

Hauptberichter: Prof. Dr. H. J. Herrmann
Mitberichter: Prof. Dr. G. Wunner

Universität Stuttgart
Institut für Computeranwendungen 1

2000

1 Einleitung

Gekoppelte System aus Teilchen und einem Fluid, wie sie z. B. bei Suspensionen oder Aerosolen vorliegen, zeigen Phänomene die sowohl auf molekulare als auch auf langreichweitige hydrodynamische Kräfte zurückzuführen sind. Während bei Kolloiden (eine Suspension von Brown'schen Teilchen) oft elektrostatische oder Van der Waals Kräfte zwischen den Teilchen das Verhalten der Suspension bestimmen, ist z.B. bei Staublawinen die Wechselwirkung der Teilchen durch das Gas für das kollektive Verhalten der Teilchen verantwortlich.

Die analytische Beschreibung von Suspensionen ist nur in wenigen, speziellen Situationen (geringe Teilchenkonzentration, unendlich ausgedehntes System, schleichende Strömung) möglich, weshalb man oft auf phänomenologische Beschreibungen oder Computersimulationen angewiesen ist. Phänomenologische Beschreibungen sind aber nur in bestimmten Parameterbereichen gültig und können nicht für die Voraussage in anderen Parameterbereichen verwendet werden, wohingegen in Computersimulationen wie Experimente neue Parameterbereiche erforschen können. Durch die sich bewegenden Teilchen, die als sich bewegende Ränder in der Flüssigkeit behandelt werden müssen, ist die Simulation von Suspensionen auf der Teilchenskala sehr aufwendig. Durch einen Übergang von der Teilchenskala zu einer makroskopischen Beschreibung der Suspension könnte der Aufwand beträchtlich reduziert werden. Dazu ist jedoch das detaillierte Verständnis der Suspension Voraussetzung. Um einen besseren Einblick in das Verhalten von Suspensionen zu bekommen, untersuchen wir mono- und bidisperse Suspensionen in einem quaderförmigen Behälter unter dem Einfluß der Gravitation. Der Behälter kann dabei periodische Randbedingungen oder feste Wände aufweisen. Außerdem wird ein Advektions-Diffusions-Modell zur Beschreibung der Konzentrationen in polydispersen Suspensionen aufgestellt.

2 Die Simulationsmethode

Die numerische Methode zur Simulation von suspendierten Teilchen basiert auf der sogenannten *immersed boundary* Technik von Fogelson und Peskin [25]. Dabei werden die Bewegungsgleichungen der Flüssigkeit auf einem regulären Gitter gelöst und die Teilchen durch Zwangskräfte modelliert. Dadurch können spezielle Lösungsverfahren für die Navier-Stokes-Gleichungen verwendet werden, die die Regularität des Gitters ausnutzen.

Die Simulation läßt sich in drei Teilprobleme zerlegen: 1. die Lösung der Flüssigkeitsgleichungen, 2. die Bewegung der suspendierten Teilchen und 3. die Kopplung zwischen Flüssigkeit und Teilchen. Die Lösung der ersten beiden Teile sind hinreichend bekannt,

und wir werden uns deshalb auf die Kopplung konzentrieren. Für eine detailliertere Beschreibung der Simulationsmethode verweisen wir auf Ref. [48].

Die Grundlage für die Flüssigkeitsbeschreibung ist die Navier-Stokes Gleichung,

$$\rho\frac{\partial\vec{v}}{\partial t} + \rho(\nabla\cdot\vec{v})\vec{v} = -\nabla p + \eta\nabla^2\vec{v} + \vec{f}. \tag{Z.3}$$

Dabei bezeichnet ρ die Dichte, η die Viskosität, $\vec{v}$ die Geschwindigkeit, p den Druck der Flüssigkeit und $\vec{f}$ die Volumenkraft, die auf die Flüssigkeit wirkt. Die Variablen werden auf einem regulären Gitter, einem *marker and cell* Gitter in zweiter Ordnung durch finite Differenzen diskretisiert und mit Hilfe eines zeitexpliziten und druckimpliziten Verfahrens unter Erfüllung der Inkompressibilitätsbedingung $\nabla\cdot\vec{v} = 0$ gelöst.

Die Integration der Bewegungsgleichungen für die Teilchen erfolgt durch einen Geschwindigkeits-Verlet-Algorithmus für die Translation und durch einen Gear-Prediktor-Korrektor vierter Ordnung für die Rotation [3].

Das dritte Teilproblem, die Kopplung zwischen den Teilchen und der Flüssigkeit erfolgt über die Volumenkraft in der Navier-Stokes-Gleichung (Z.3). Dazu wird das Teilchen i durch zwei Anteile modelliert: Der erste besteht aus einem Flüssigkeitselement mit derselben geometrischen Form wie das Teilchen. Die Flüssigkeit in diesem Volumen wird nun durch Zwangskräfte so bewegt, dass sie sich wie ein Festkörper innerhalb der restlichen Flüssigkeit bewegt. Sie verhält sich dann wie ein Teilchen der Dichte ρ mit einer Masse $M_i^{\mathrm{l}} = V_i\rho$ und einem Trägheitsmoment von $I_i^{\mathrm{l}} = (2/5)M_i^{\mathrm{l}}a^2$ im Falle einer Kugel mit Radius a. Der zweite Modellanteil ist eine Teilchenschablone, die ebenfalls die geometrische Form des physikalischen Teilchens hat und die Masse M_i^{t} und das Trägheitsmoment I_i^{t} trägt, die zusammen mit dem Flüssigkeitsanteil die Masse und das Trägheitsmoment des physikalischen Teilchens ergeben: $M_i = M_i^{\mathrm{l}} + M_i^{\mathrm{t}}$ und $I_i = I_i^{\mathrm{l}} + I_i^{\mathrm{t}}$.

Die Kopplung zwischen der Flüssigkeit und der Teilchenschablone erfolgt über die Zwangskräfte. Die Zwangskräfte werden durch ein explizites Verfahren berechnet, das ähnlich wie bei sogenannten Penalty-Verfahren ein gewisse Deformation des vom Teilchen bedeckten Flüssigkeitsvolumens zulässt und aus dieser Deformation die Zwangskräfte berechnet, die der Deformation entgegenwirken.

Konkret werden dazu in dem Flüssigkeitsvolumen, das vom Teilchen i überdeckt wird sogenannte Markierungspunkte $\vec{x}_{ij}^{\,m}$ in der Flüssigkeit verteilt. Diese Markierungspunkte bewegen sich massenlos mit der Flüssigkeit $\dot{\vec{x}}_{ij}^{\,m} = \vec{v}(\vec{x}_{ij}^{\,m})$. Mit jedem dieser Markierungspunkte wird ein Referenzpunkt $\vec{x}_{ij}^{\,r}$ auf der Teilchenschablone assoziiert, so dass zum Zeitpunkt $t = 0$ die Beziehung $\vec{\xi}_{ij} = \vec{x}_{ij}^{\,m} - \vec{x}_{ij}^{\,r}$ gilt.

Die Kraftdichte $\vec{f}$ auf die Flüssigkeit wird nun aus den Abständen zwischen Markierungs-

und Referenzpunkten berechnet

$$\vec{f}_{ij}(\vec{x}) = (-k\vec{\xi}_{ij} - 2\gamma\dot{\vec{\xi}}_{ij})\delta(\vec{x} - \vec{x}^m_{ij}), \tag{Z.4}$$

wobei k eine Federkonstante und γ eine Dämpfungskonstante darstellen. $\delta(\vec{x})$ bezeichnet die Dirac'sche Deltafunktion. Die Federkonstante k muss dabei hinreichend groß gewählt werden, so dass die Differenz ξ_{ij} immer wesentlich kleiner als die Gitterkonstante h des Flüssigkeitsgitters ist, d.h. dass $|\xi_{ij}| \ll h$ zu allen Zeiten erfüllt ist.

Die Simulationsmethode wurde an verschiedenen Testfällen wie der Umströmung periodischer Anordnungen von Kugeln und der Sedimentation monodisperser Kugeln verifiziert.

3 Monodisperse Sedimentation

3.1 Geschwindigkeitsfluktuationen

Während es für die mittleren Sinkgeschwindigkeiten der Teilchen in nicht Brown'schen Suspensionen theoretische Vorhersagen gibt [7, 13], ist das Verständnis der Geschwindigkeitsfluktuationen noch nicht befriedigend. Theoretische Betrachtungen [17, 42, 100] sagen voraus, dass die Geschwindigkeitsfluktuationen in Suspensionen mit der Größe des Behälters anwachsen. In experimentellen Untersuchungen wird diese Abhängigkeit von der Systemgröße aber nicht oder nur bis zu einer bestimmten Systemgröße gefunden [75, 93]. Simulationen von Suspensionen [62] zeigen eine Divergenz der Geschwindigkeitsfluktuationen mit der Systemgröße.

Abschätzung der Geschwindigkeitsfluktuationen

Mit Hilfe einer Abschätzung von Hinch [43] und den experimentellen Resultaten von Segrè et al. [93] kann ein Ausdruck für das Skalierungsverhalten der Geschwindigkeitsfluktuationen hergeleitet werden. Wenn man sich ein System der Größe $2L \times L \times L$ zufällig verteilter, suspendierender Teilchen vorstellt, das in zwei Hälften geteilt wird, so erwartet man dass sich im Mittel in beiden Teilen $N = (3/4\pi)\phi(L/a)^3$ Teilchen befinden. Bei einer zufälligen Teichenverteilung variiert die mittlere Teilchenzahl um $\sqrt{N}$ Teilchen, so dass sich ein antreibender Gewichtsunterschied von

$$F_1 = \pm\sqrt{N}\ \frac{4}{3}\pi a^3 \Delta\rho g \tag{Z.5}$$

ergibt. Diese Kraft verursacht solange einen Geschwindigkeitsunterschied zwischen den beiden Hälften dem die viskose Scherkraft entgegenwirkt. Die Scherkraft zwischen

diesen beiden Bereichen kann durch den zu erwartenden Geschwindigkeitsgradienten $\Delta U/L$, die Viskosität der Flüssigkeit und die Fläche $\sim L^2$, die die beiden Bereiche trennt abgeschätzt werden.

$$F_2 = \eta \frac{\sigma}{L} L^2. \tag{Z.6}$$

Hier haben wir die Geschwindigkeitsdifferenz mit σ bezeichnet. In einem stationären Zustand werden beide Kräfte sich gegenseitig aufheben, und man kann die Größe der Geschwindigkeitsfluktuationen σ abschätzen:

$$\sigma = \frac{4}{3}\pi \frac{\sqrt{\frac{\phi L^3}{a^3}} a^3 \Delta\rho g}{\eta L} \sim U_{\mathrm{St}} \sqrt{\frac{\phi L}{a}}, \tag{Z.7}$$

wobei U_{St} die Stokes Geschwindigkeit bezeichnet. Man erwartet also ein Anwachsen der Geschwindigkeitsfluktuationen mit $\sqrt{L}$.

Wenn es hingegen eine Längenskala ξ gibt, jenseits derer die Suspension als homogen und unkorreliert betrachtet werden kann, dann wäre unser Argument nur gültig für $L < \xi$. Für Systemabmessungen $L > \xi$ übernimmt die Größe der noch korrelierten Bereiche die Rolle der Systemgröße. Segrè et al. [93] fanden in ihren Experimenten eine Korrelationslänge von $\xi_{||} = 11a\phi^{-1/3}$, woraus sich für die Geschwindigkeitsfluktuationen in großen Systemen folgendes Skalierungsverhalten ergäbe:

$$\sigma \sim V_{\mathrm{St}} \phi^{1/3}. \tag{Z.8}$$

Systeme mit periodischen Randbedingungen

Um den Einfluß der Wände zu eliminieren, verwenden wir in allen Richtungen periodische Randbedingungen und messen die Fluktuationen der Sinkgeschwindigkeit der Teilchen in Systemen verschiedener Größe und verschiedenem Volumenanteil ϕ der Teilchen. Wenn sich die Systemgröße unterhalb des Größe befindet, ab der die Geschwindigkeitsfluktuationen unabhängig von der Systemgröße werden, erwartet man folgendes Verhalten,

$$(\sigma/U_{\mathrm{St}}) \sim (L\phi)^{1/2}. \tag{Z.9}$$

Bei einer Auftragung der normierten Geschwindigkeit gegen $(L\phi)^{1/2}$ sollten deshalb alle Datenpunkte auf einer Geraden liegen. Abbildung Z.8 zeigt die gemessenen Werte und eine Ausgleichsgerade $f(x) = bx + c$ mit $b = 0.63$ und $c = -0.12$.

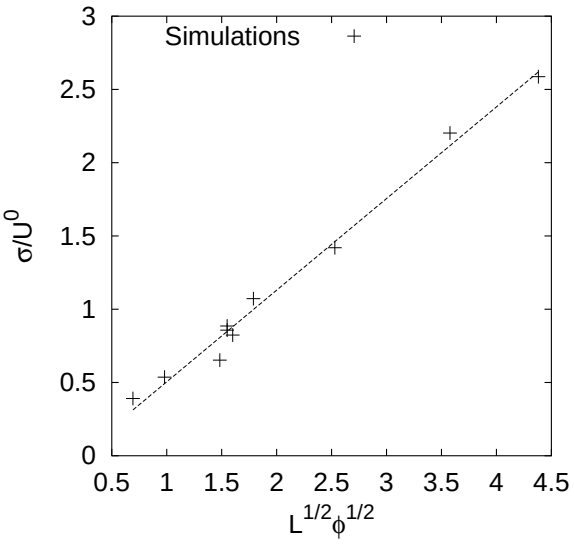

Abbildung Z.8: Geschwindigkeitsfluktuationen aufgetragen über $L^{1/2}\phi^{1/2}$. Nach Gleichung (Z.7) erwartet man, dass die Datenpunkte auf einer Geraden liegen. Die gestrichelte Linie zeigt die Ausgleichsgerade $f(x) = bx + c$ mit $b = 0.63$ und $c = -0.12$.

Systeme mit Wänden

In experimentellen Untersuchungen können periodische Randbedingungen nicht realisiert werden. Um den Einfluß von Wänden auf die Suspension zu untersuchen und die Simulationen mit Experimenten vergleichbar zu machen, werden in den Richtungen senkrecht zur Gravitation feste Wände als Begrenzung des Simulationsvolumens eingebaut. Dadurch sind die Bedingungen bis auf die Randbedingungen in Richtung der Gravitation identisch mit den Experimenten von Nicolai und Guazzelli [75].

In ihren Experimenten verwendeten Nicolai und Guazzelli Glaskugeln in einer viskosen Flüssigkeit und ließen sie bei einem Volumenanteil von $\phi = 0.05$ in einem Behälter mit einer Höhe von $L_y = 1262a$ und Breite von $L_x = 252a$ sedimentieren. Die Tiefe des Behälters wurde von $L_z = 50a$ bis $200a$ variiert. Die gemessenen Geschwindigkeitsfluktuationen waren innerhalb der Fehlerbalken konstant und betrugen $\sigma_x \approx 0.33 \pm 0.04$ und $\sigma_y \approx 0.66 \pm 0.08$. Das Verhältnis der Fluktuationen betrug $\sigma_y/\sigma_x \approx 2$.

Unsere Simulationen zeigen (vgl. Abb. Z.9(a)), dass die Geschwindigkeiten in Systemen mit einer Tiefe $L_z > 100a$ innerhalb der Fehlerbalken unabhängig von der Tiefe des Systems werden.

Um ausschließen zu können, dass die Breite des Systems einen Einfluß auf den Betrag der Geschwindigkeitsfluktuationen hat, wurden auch Simulationen bei einer festen Tiefe $L_z = 100a$ und verschiedenen Breiten $L_x = 50 \ldots 250a$ durchgeführt. Diese sind in

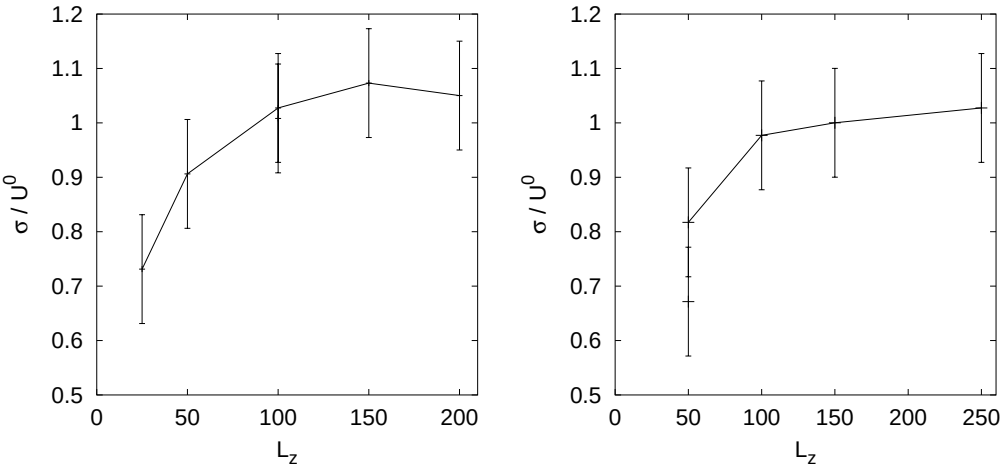

(a) (b)

Abbildung Z.9: Geschwindigkeitsfluktuationen σ_y als Funktion der Systemgröße. Auf der linken Seite (a) wird σ_y in Abhängigkeit von L_z bei $L_x = 250$ gezeigt. Auf der rechten Seite (b) wird L_x variiert und $L_z = 100$ festgehalten. Die Fluktuationen wachsen bis die kleinste Abmessung des Behälters einen Wert von $\approx 100a$ überschreitet.

Abbildung Z.9(b) gezeigt. Wie zu sehen ist, werden die Geschwindigkeitsfluktuationen von der kleinsten Abmessung des Systems kontrolliert.

Die Anwesenheit der Wände ändert also das Skalierungsverhalten der Geschwindigkeitsfluktuationen im Vergleich zu periodischen Randbedingungen drastisch.

4 Bidisperse Sedimentation

Die Sinkgeschwindigkeiten der Teilchen in einer Suspension polydispersen Teilchen wurden von Batchelor [6, 8] in erster Ordnung angegeben. Dabei wurden die Wechselwirkungen von Teilchenpaaren in einer selbstkonsistenten Verteilung von Teilchen berücksichtigt. Für die Sinkgeschwindigkeit der einzelnen Teilchensorten ergab sich

$$\langle \vec{U}_i \rangle = \vec{U}_i^{(0)}(1 + \sum_{j=1}^{N} S_{ij}\ \phi_j). \tag{Z.10}$$

Hierbei wird mit $\vec{U}_i^{(0)}$ die Stokes Geschwindigkeit der Teilchensorte i bezeichnet. Die Sedimentationskoeffizienten S_{ij} sind Funktionen des Teilchengrößenverhältnisses

$$\lambda = \frac{a_j}{a_i} \tag{Z.11}$$

und des reduzierten Dichteverhältnisses

$$\gamma = \frac{\rho_j - \rho}{\rho_i - \rho}. \tag{Z.12}$$

Die Sedimentationskoeffizienten S_{ij} wurden für bestimmte Werte für λ und γ von Batchelor und Wen [8] numerisch berechnet.

4.1 Sedimentationsgeschwindigkeiten

Für $\gamma = 1$ und zwei Teilchensorten reduziert sich die Gleichung (Z.10) zu

$$\begin{aligned} < U_s > &= U_s^{(0)}(1 + S_{ss}\,\phi_s + S_{sl}\,\phi_l), \\ < U_l > &= U_l^{(0)}(1 + S_{ls}\,\phi_s + S_{ll}\,\phi_l), \end{aligned} \tag{Z.13}$$

wobei der Index s die kleinen und l die großen Teilchen bezeichnet. Die Sedimentationskoeffizienten sind nur noch von λ abhängig. Die numerischen Werte von Batchelor und Wen können durch ein Polynom zweiter Ordnung approximiert werden,

$$\begin{aligned} S_{sl}(\lambda) &= -3.52 - 1.04\,\lambda - 1.03\,\lambda^2, \\ S_{ls}(\lambda) &= -3.52 - 1.04/\lambda - 1.03/\lambda^2, \end{aligned} \tag{Z.14}$$

wobei wir λ als $\lambda = a_l/a_s \geq 1$ definieren. Die beiden Sedimentationskoeffizienten S_{ss} und S_{ll} haben wie im monodispersen Fall beide den Wert -5.6.

Abbildung Z.10 zeigt die gemessenen Sedimentationsgeschwindigkeiten in Abhängigkeit vom Radienverhältnis λ. Durch die endliche Systemgröße von $24 \times 24 \times 24$ werden die Teilchen durch ihre periodischen Abbilder beeinflußt, und die erwartete Sedimentationsgeschwindigkeit muss um die Korrektur von Hasimoto [41]

$$U/U_\infty = 1 - 1.7601\,\phi^{1/3} + \phi - 1.5593\,\phi^2, \tag{Z.15}$$

berichtigt werden. Eine zweite Korrektur wird wegen der endlichen Reynoldszahl notwendig, da mit zunehmendem Teilchenradius auch die Reynoldszahl ansteigt. Nach Proudman und Pearson [83] muss die Stokes Kraft auf ein Teilchen durch

$$\vec{F} = 6\pi a \eta \vec{U}\,\left(1 + \frac{3}{8}Re - \frac{9}{40}Re^2 \ln\frac{1}{Re}\right)\,, \tag{Z.16}$$

korrigiert werden.

Durch das Berücksichtigen dieser beiden Effekte stimmen die Vorhersagen von Batchelor und Wen für die Sedimentationsgeschwindigkeiten sehr gut mit den Ergebnissen der Simulation überein. Für die von Batchelor und Wen vorhergesagte Paarverteilungsfunktion $g(r)$ ist die Übereinstimmung hingegen nicht so ausgeprägt, was auf Mehrteilchenwechselwirkungen zurückzuführen ist.

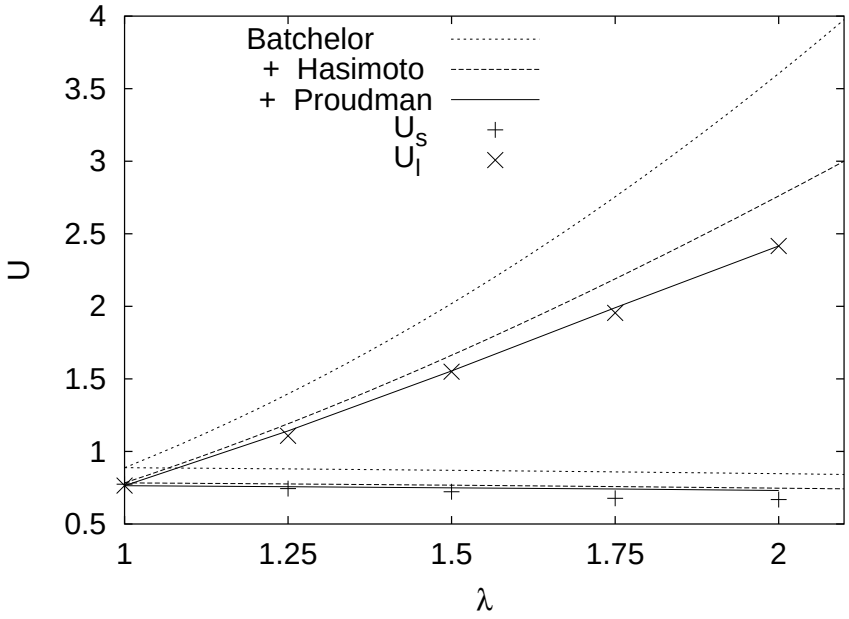

Abbildung Z.10: Abhängigkeit der Sinkgeschwindigkeit der kleinen (+) und großen ($\times$) Teilchen von λ verglichen mit den Vorhersagen von Batchelor (gepunktete Linien), und den Korrekturen aufgrund des endlichen Systemvolumens (gestrichelte Linien) und der endlichen Reynoldszahl (durchgezogene Linien).

5 Modellierung polydisperser Suspensionen

Bisher wurden nur Systeme mit periodischen Randbedingungen in Richtung der Gravitation betrachtet. Sobald aber die Translationsinvarianz in Richtung der Gravitation z.B. durch das Vorhandensein von Wänden gebrochen wird, bilden sich verschiedene Zonen (z.B. Sediment und klare Flüssigkeit) mit unterschiedlichen Teilchenkonzentrationen aus. Bei jeder realen Suspension handelt es sich um ein System mit gebrochener Translationsinvarianz. Zur Beschreibung der Konzentrationsverläufe wird normalerweise das dreidimensionale System auf eine Dimension reduziert, indem das System in Richtung der Gravitation in dünne Schichten zerlegt und die betrachteten Größen in den Richtungen orthogonal zur Gravitation gemittelt werden.

Zur Beschreibung der Konzentrationen in Abhängigkeit von der Höhe wird häufig die Kynch-Theorie [57] verwendet. Dabei handelt es sich um eine Advektionsgleichung der Form

$$\frac{\partial \phi_i}{\partial t} + \frac{\partial\, \phi_i U_i(\Phi)}{\partial y} = 0, \tag{Z.17}$$

wobei $\Phi(y) = (\phi_1(y), \phi_2(y), \dots)$ die Konzentrationen der Teilchensorten $i = 1 \dots N$ an der vertikalen Position y darstellt und $U_i(\Phi)$ die Sedimentationsgeschwindigkeit der

Teilchensorte i.

Wenn die Abhängigkeit der Sedimentationsgeschwindigkeit von der lokalen Konzentration der Teilchen bekannt ist, kann mit Hilfe von Gleichung (Z.17) aus einer Anfangssituation die zeitliche Entwicklung der Konzentrationen berechnet werden. Der Vergleich des advektiven Kynch-Modells mit Simulationen zeigt jedoch, dass das Kynch-Modell zwar die großräumige Struktur der Konzentrationsverläufe wiedergeben kann, aber nicht die genauen Verläufe an den Schockfronten [14].

Wir erweitern deshalb das Advektionsmodell um einen Diffusionsterm, der die hydrodynamische Diffusion der sedimentierenden Teilchen beschreiben soll. Das Advektions-Diffusions-Modell hat nun folgende Form:

$$\frac{\partial \phi_i}{\partial t} = -\frac{\partial}{\partial y}\left(\phi_i U_i(\Phi) - D_i(\Phi)\frac{\partial \phi_i}{\partial y}\right). \tag{Z.18}$$

wobei $D_i(\Phi)$ die effektive Diffusionskonstante in Abhängigkeit von den lokalen Konzentrationen bezeichnet. Zur Vollständigkeit des Modells müssen noch die beiden konstitutiven Beziehungen zwischen Konzentration und Sedimentationsgeschwindigkeit und zwischen Konzentration und dem Diffusionskoeffizienten angegeben werden.

Für die Sedimentationsgeschwindigkeiten erweitern wir Batchelors lineare Beziehung für polydisperse Suspensionen, deren Gültigkeit für kleine Konzentrationen gezeigt wurde um sie auch bei höheren Konzentrationen einsetzen zu können. Die erweiterte Form

$$\langle U_i \rangle = U_i^{(0)} \frac{e^{\left(1+\sum_j S_{ij}\phi_j + 2\phi_t/\phi_\infty\right)}(\phi_\infty - \phi_t)^2}{e\,\phi_\infty^2} \tag{Z.19}$$

ist für $\phi \to 0$ identisch mit Gl. (Z.10), weist aber nicht die unphysikalischen negativen Werte für $\phi > 0.178$ auf.

Für den Diffusionskoeffizienten schlagen wir folgenden funktionalen Zusammenhang vor

$$D_i(\Phi) = D_{\max} A\, a_i U_i^{(0)} \phi_i \left(\frac{U_i(\Phi)}{U_i^{(0)}}\right)^2, \tag{Z.20}$$

der auch die experimentellen Resultate von Nicolai *et al.* [75] gut wiedergibt. In Gleichung (Z.20) ist $A = 31.54$ eine Normierungskonstante, die so gewählt ist, dass $D_{\max}$ der maximale Betrag des Diffusionskoeffizienten ist.

Durch die Vorgabe von Anfangs- und Randbedingungen kann der zeitliche Verlauf der Konzentrationen durch numerische Integration der Differentialgleichung berechnet werden. In Abbildung Z.11 vergleichen wir die Vorhersagen des Advektions-Diffusions-Modells mit $D_{\max} = 4.0$ mit der dreidimensionalen Simulation eines Systems der Größe $36 \times 576 \times 36$ mit zwei Teilchensorten $(a_l/a_s = 1.414)$.

a)

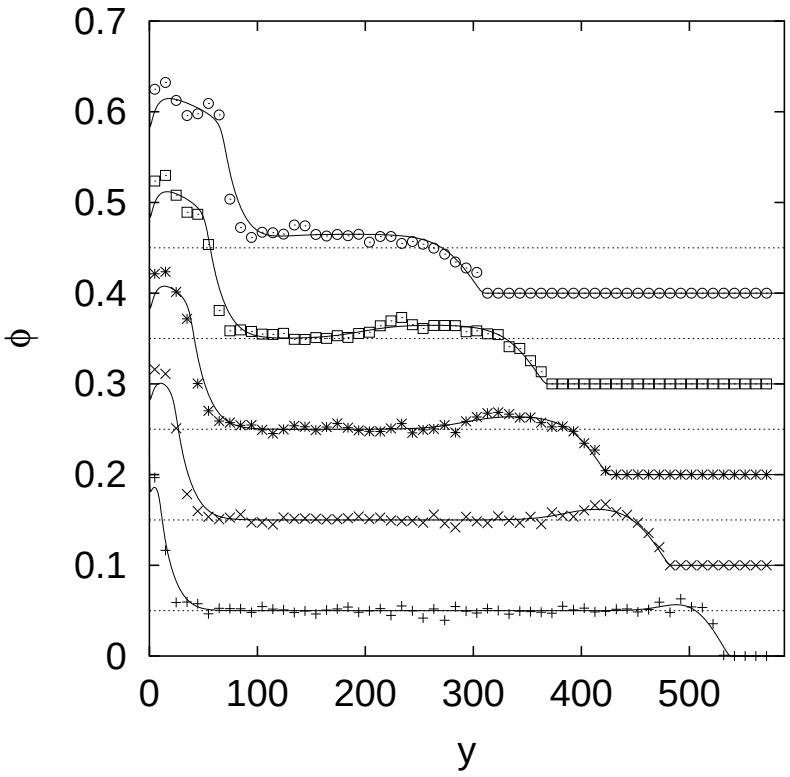

b)

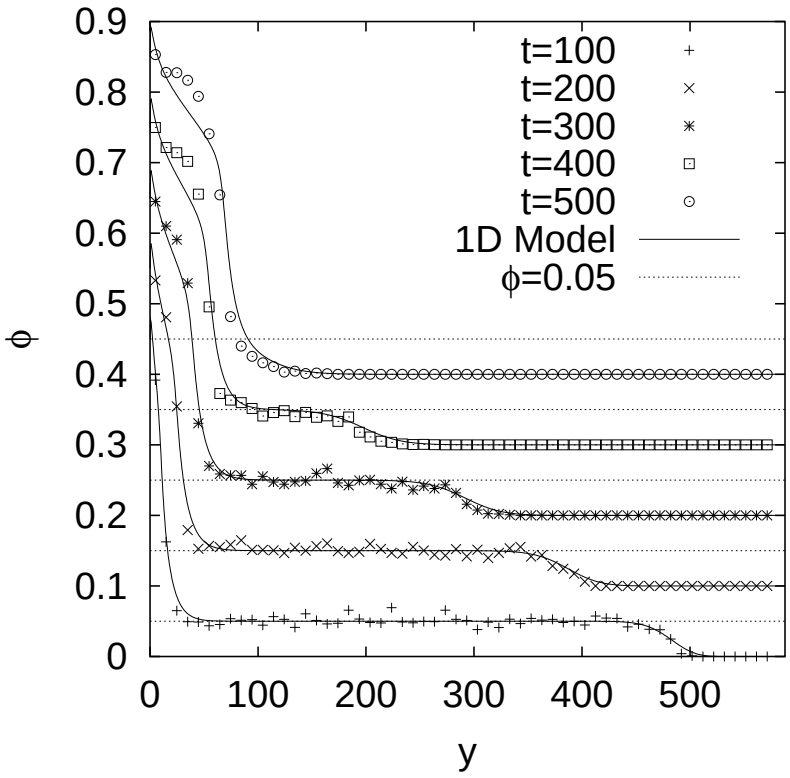

Abbildung Z.11: Volumenanteil der kleinen Teilchen (a) und der großen Teilchen (b). Die durchgezogenen Linien zeigen die Vorhersagen des Advektions-Diffusions-Modells. Die Datenpunkte sind Messungen einer dreidimensionalen Simulation. Die Konzentrationswerte sind jeweils um 0.1 nach oben verschoben worden. Die gepunktete Linie zeigt die Anfangskonzentration von $\phi = 0.05$.